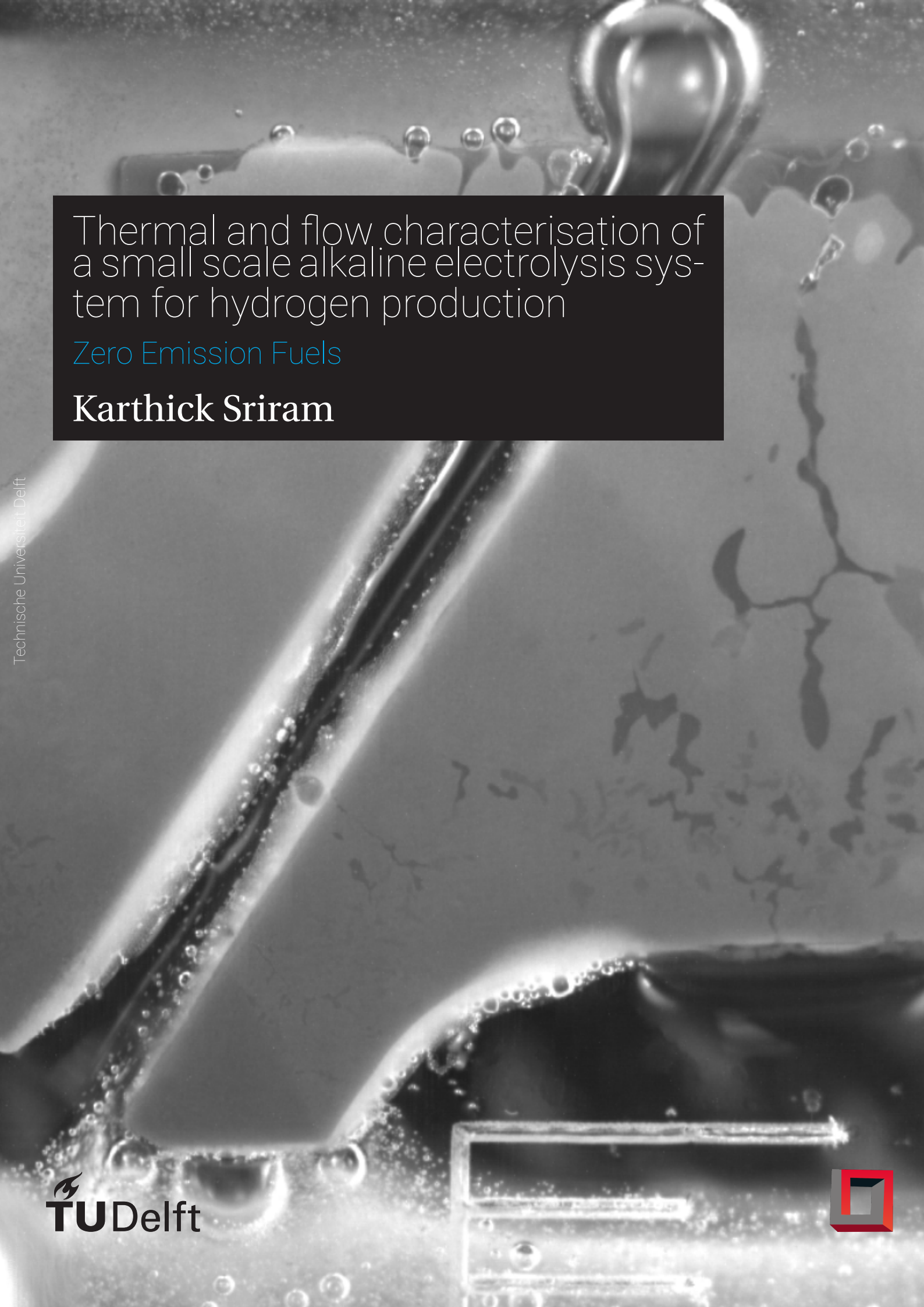

Thermal and flow characterisation of a small scale alkaline electrolysis system for hydrogen production

Zero Emission Fuels

Karthick Sriram

Technische Universiteit Delft

TU Delft

Thermal and flow characterisation of a small scale alkaline electrolysis system for hydrogen production

Zero Emission Fuels

by

Karthick Sriram

to obtain the degree of Master of Science
at the Delft University of Technology,
to be defended on Friday August 30, 2019 at 09:30 AM.

Student number:	4734777	
Project duration:	December, 2018 – August, 2019	
Thesis Committee:	Prof.dr.ir. R.A.W.M. Henkes,	TU Delft (Chair)
	Dr.ir. W.P. Breugem,	TU Delft
	Dr. ir. J.W. Haverkort,	TU Delft, supervisor
	Ir. Jan van Kranendonk,	ZEF, supervisor

This thesis is confidential and cannot be made public until December 31, 2021.

TU Delft

Abstract

Zero Emission Fuels (ZEF B.V.) is a start-up working to build a sustainable methanol micro-plant. Carbon dioxide and water is obtained from atmosphere. Hydrogen is obtained from captured water through alkaline electrolysis and the hydrogen is used for methanol production. The alkaline electrolyser should run at 50 bar and 90°C with 30% KOH as the electrolyte. It is a multi-cell design and the electricity supplied to the electrolyser leaks within the system through the electrolyte. This is the energy supplied to the system not being used for splitting water into hydrogen and oxygen. Leaking current and flow scale with the length and the radius of any channel in the system and contradict each other in terms of requirements.

This study focuses on characterising the electrolyser to validate a modified version of the existing Matlab model at a channel in the system for two different dimensions of the channel. The Matlab model predicts the flow and the leaking currents in the system. Estimating the flow in the system is essential to validate the model and using the model, the leaking currents are estimated. Experiments were performed on a single cell version of the electrolyser at atmospheric pressure to obtain the flow and thermal characteristics. Comsol simulations were ran on the single cell system to support the Matlab results.

The heating curve of the system was obtained at four different points in the system to check for the necessity of insulation. The system went up to 56°C at the hottest point in the system after 2 hours. This confirmed for the necessity of insulation. The diameter of the bubbles at the electrode were measured and compared to the estimated diameter in Matlab. They were 34% off. The flow part of the experiments were done at a lower current density to simulate 50 bar flow at 1 bar. The flow rate of the electrolyte was estimated using high speed cameras and tracking fluorescent particles at one of the channels in the system. The values of the flow rate from Comsol, Matlab and Comsol were 25% away from each other whereas Matlab and experiments were 65% away from each other. The mass flow rate predicted by Comsol was in between Matlab and experiments. The absence of a temperature network to estimate temperature at every part of the system, the approximate geometry and ignoring smaller resistances to flow in the Matlab model are responsible for the offset.

Leaking currents were estimated in the single and multi-cell system using Matlab. The power lost due to leaking currents were higher in the multi-cell system as compared to the single cell system. The reduction in leaking currents by using gas slugs was estimated and the current design achieves the electrical efficiency of 99%. Recommendations were to make the channel diameter larger and remove the part of the channel that is in the cell. Further modifications to the Matlab and Comsol model were suggested to improve the prediction. Experiments related to multi-cell setup have to be done to estimate the actual electrical efficiency of the system and validate the Matlab model.

Acknowledgements

There are many people who lent a helping hand to complete my thesis. I would like to thank ZEF B.V. for giving me the opportunity to be a part of their team. It was great working with them. The learning curve was steep but fun. I would like to thank Jan who was always there around to provide me with the required knowledge and feedback. I would like to thank Ulrich and Hessel who were a constant source of energy and motivation without whom climbing the hill would have been difficult.

I would also like to thank my supervisor Dr.ir. J.W.Haverkort who guided me through the thesis and also pushed the limits of the thesis which brought a lot of structure and information to the thesis and myself. The discussions with him were filled with so much information and helped me when it was required. I would like to thank Hadi Rajei who helped me with the experiments and also his constant monitoring helped me stay on track. I would also like to thank Michel and Jaap for granting me access to the laboratory and providing me with the necessary equipment. A special thanks to Edwin Overmars who provided me with the flow measuring equipment without whom the results in this thesis would have not been possible to visualise. I would also like to thank Prof.Dr.ir. R.A.W.M. Henkes and Dr.ir. W.P. Breugem for agreeing to be a part of the graduation committee.

This journey was made so simple because of the presence of a few people in my life. My parents deserve the biggest credit for putting up with me and shaping me into who I am today. My life is not complete without my two sisters who have gone to a great extent to make sure I have the fuel for the day. I would also like to thank my friends who were a source of positive energy.

Karthick Sriram
Delft, August 2019

Contents

List of Figures

List of Tables

List of Abbreviations

CO_2	Carbon dioxide
CPVC	Chlorinated PolyVinyl Chloride
H_2O	Water
H_2	Hydrogen
HHV	Higher Heating Value
KOH	Potassium hydroxide
NTC	Negative Temperature Coefficient temperature sensor
O_2	Oxygen
PMMA	Poly Methyl Meth Acrylate
ZEF	Zero Emission Fuels

Greek Symbols

α	Void fraction or gas holdup	[-]
β	Thermal coefficient of expansion	[K^{-1}]
Δ	Difference	[-]
η	Overpotential	[V]
γ	Efficiency	[%]
κ	Electrical conductivity of the electrolyte	[$S \cdot m^{-1}$]
λ	Thermal conductivity	[$W \cdot m^{-1} \cdot K^{-1}$]
μ	Dynamic viscosity	[Pa·s]
ρ	Density	[$kg \cdot m^{-3}$]
σ	Surface tension	[$N \cdot m^{-1}$]

List of Symbols

$\dot{Q}$	Heat supplied	[W]

$\dot{m}$	Mass flow rate	[kg·s^{-1}]
A	Area	[m^2]
c_p	Specific heat capacity at constant pressure	[W·m^{-2}·K^{-1}]
d	diameter	[m]
F	Force	[N]
F_const	Faraday's constant	[C·mol^{-1}]
G	Gibbs free energy	[kJ·mol^{-1}]
g	acceleration due to gravity	[m·s^{-2}]
H	Enthalpy	[kJ·kg^{-1}]
h	Heat transfer coefficient	[W·m^{-2}·K^{-1}]
H_cell	Height of the cell	[m]
I	Current	[A]
j	Current density	[A·m^{-2}]
l	length	[m]
n	number of electrons produced per mole of reactant	[-]
P	Pressure	[bar]
R	Resistance/Universal gas constant	[Ω]
R_const	Universal gas constant	[J·mol^{-1}·K^{-1}]
S	Entropy	[kJ·mol^{-1}·K^{-1}]
T	Temperature	[K]
t	time	[s]
V	Voltage	[V]
v	velocity	[m·s^{-1}]
w	Width	[m]
Ca	Capillary number	[-]
Eo	Eotvos number or Bond number	[-]
Pe	Peclet number	[-]
Re	Reynolds number	[-]

Subscripts

ads	adsorbed
air	air
b	buoyant
base	base or bottom
c	convective
cell	cell
ch	channel
com	comsol
d	drag
e	environment
flow	flow
ft	flash tank
g	gas
l	lift
l	liquid
ref	reference
rev	reversible
tn	thermo-neutral

1 Introduction

The increasing concern about pollution and climate change has led towards greener options, out of which hydrogen is appealing and has the potential of being the fuel of the future [14]. Hydrogen has advantages like it does not produce harmful by-products [26]. There are many ways of hydrogen production [38], among which electrolysis in 2011 accounted for nearly 4% of the total hydrogen produced among the other sources like coal and hydro carbons, and 8% is used to produce methanol [4]. Hydrogen production by electrolysis can be made carbon neutral by using renewable energy sources like solar panels. Modelling and optimisation of electrolysis using solar panels have also been studied previously in [32] and [42]. Alkaline electrolysis systems have advantages like long lifetime and low material costs [38]. But when it is compared to the liquid fuels, hydrogen is relatively not easy to be stored and transported. Hydrogen is also explosive and exists as a gas at room temperature [19]. Hence, an alternative to hydrogen had to be a fuel which does not have these drawbacks. Methanol is one such fuel which can be an alternative due to higher octane rating, low NO_x and SO_x emissions. Methanol can be easily produced from hydrogen and carbon dioxide. Zero Emission Fuels (ZEF B.V.) is a start-up that is working on making a small scale and low cost methanol plant by using hydrogen produced through alkaline electrolysis. Table 1.1 shows how the specifications of the alkaline electrolyser used by ZEF compare to the typical specifications of an alkaline electrolyser [13].

Table 1.1: Comparison of typical specifications of an alkaline electrolyser [13] with the ZEF alkaline electrolyser

Parameter	Alkaline electrolyser		Units
	Typical	ZEF	
Temperature	60-80	90	°C
Pressure	<30	50	bar
Current density	<0.45	0.3	A/cm^{-2}
Cell voltage	1.8-2.4	2	V
Cell area	3-3.6	$3 \cdot 10^{-3}$	m^2

1.1. Zero Emission Fuels

Zero Emission Fuels (ZEF B.V.) is a start-up in the Netherlands. The aim of the company is to produce methanol at 50 bar at a small scale and low cost. Multiple micro-plants will be used at a particular location as opposed to using one big plant for the production bringing down the complexity of the system. The path taken by ZEF to produce methanol is by capturing water and carbon dixodie from air and producing methanol with a well-defined process. The process is shown in Figure 1.1. The process begins with capturing water and carbon dioxide from atmosphere using direct air capture system. This is desorbed from the system at 0.1 bar and pressurised to 55 bar using compressors.

The mixture is then passed through a degasser, where the carbon dioxide is separated from water. The water is then stored at 55 bar for being supplied to the alkaline water electrolyser. The water is then supplied to the electrolyser which contains potassium hydroxide (KOH). The alkaline water electrolyser is a system that uses electricity to split water into hydrogen and oxygen.

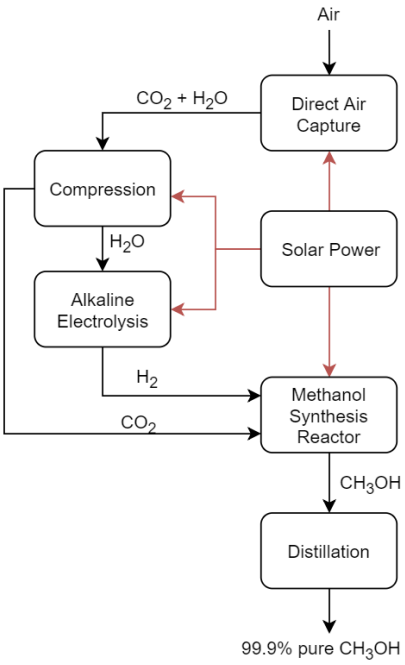

Figure 1.1: Flowchart showing the path taken for methanol production method at ZEF. Carbon dioxide and water are captured from air. Hydrogen obtained from water through electrolysis and carbon dioxide from air are used to produce methanol.

The temperature and pressure inside the electrolyser are maintained at 90°C and 50 bar respectively. Production of methanol at a pressure of 50 bar takes place in a methanol synthesis reactor using carbon dioxide from the direct air capture unit and hydrogen from the alkaline water electrolyser. The system does not produce methanol at the required level of purity.

The water content in the methanol has to be removed before it is stored and shipped. The distillation unit contains a wick and a heater to separate methanol from water. The final product required is 99.99% pure methanol. The whole system requires energy in places like the heater in methanol synthesis reactor and the electricity for hydrogen production in the alkaline water electrolyser. The energy is supplied by three solar panels, making the process sustainable.

1.2. Scope and research questions

This thesis focuses on the characterisation and improvement of the alkaline water electrolyser of the ZEF micro-plant to conduct experiments on the electrolyser and obtain the thermal and flow characteristics of the system. It is important that the system operates at 90°C and 50 bar. A smaller system was designed to analyse both the thermal and flow characteristics of the system. There is no external heat supplied to the system at the moment. The temperature of the system is the consequence of the alkaline electrolysis being operated at exothermic conditions. The thermodynamics of the system will be discussed later. Hence, it is a requirement that the temperature is maintained by the reaction. The flow in the system cannot be seen when the system is operational as it is not accessible visually. Hence, the problems with the flow and its characteristics cannot be determined when the whole system is operating. There are a few contradicting parameters like flow and leakage currents in the system for which a decision in the design had to be made. This thesis aims at answering one main research question:

Can the flow rate of the electrolyte be improved in the current ZEF alkaline electrolyser design while keeping the leaking currents in check?

To answer the main question, the following sub-questions have to be answered:

1. Can the electrolysis system be modelled and validated with respect to flow and temperature?
2. What are the thermal/flow problems in the current design?
3. How does the geometry affect the flow and leaking currents and how can it be improved?

1.3. Methodology

The thesis started with obtaining knowledge about electrolysis process and the various factors that can affect the parameters in the system like flow, temperature and electric current along with analytical equations. Knowledge about the current design of the ZEF alkaline electrolyser and the test setup was obtained from former ZEF members. The matlab model developed by M.Geraedts [18] was to be validated.

Simulations from modelling software and experiments were done for comparison of the results from the Matlab model. The set of characterisation parameters for the validation of the model were temperature, flow and leaking currents in the system. The experiments were meant to be done on a smaller multi-cell ZEF alkaline electrolyser. Due to delays in the setup and safety reasons, the system was not analysed. A single cell electrolyser was used for the validation of flow and temperature results from the system. The same system was designed using Adobe Fusion 360 and the same design was imported and simulated using Comsol Multiphysics.

Some modifications were done on the Matlab model to convert into a single cell setup and incorporate the effects of temperature. The flow results from Matlab and Comsol were compared with each other which were validated through experiments. Based on the results obtained from the current design, a modification was done to the design to see if it improves the system with respect to flow while keeping leaking currents within desired limits. Conclusions were drawn and recommendations were provided for further analysis/improvement of the model and the design of the electrolyser.

1.4. Structure of the report

The report is divided into 5 chapters. Chapter 1 gives an introduction to the general information about the company and the project of which the electrolyser is a part. Chapter 2 gives a summary of knowledge and literature including a description of the test setup. A few analytical solutions and results obtained are also a part of this section. Chapter 3 consists of the initial analysis on the system for identifying the potential problems/additions to the models. It also explains the method followed to simulate the system using Comsol Multiphysics and Matlab. A description of how the experiments were performed is also mentioned in this chapter. The results of the simulation and experiments along with the comparison is presented in Chapter 4. Chapter 5 consists of conclusion and recommendations.

2

Theory

The main parameters to be estimated in the electrolyser are with respect to temperature, flow and leaking currents in the system. Before the analysis begins, an introduction to working of an electrolyser, the resistances, the current design of the electrolyser in ZEF are discussed in this section. A few equations relevant to the study are also derived in this section.

2.1. Working of the electrolyser

In chemistry, electrolysis is the process of using current as a driving force to perform a non-spontaneous chemical reaction. The electrolysis of water (H_2O) involves passing current through water, decomposing it into hydrogen and oxygen.

There are three main types of water electrolysis, namely, alkaline water electrolysis, proton exchange membrane water electrolysis and solid oxide water electrolysis. The alkaline water electrolyser is explained further as that is the technology being used in the setup under consideration.

A schematic of an alkaline water electrolyser is shown in Figure 2.1. The electrolyser consists of an anode (positive electrode) and a cathode (negative electrode) connected to an external power source. The electrodes are in contact with the electrolyte consisting of an alkali in water.

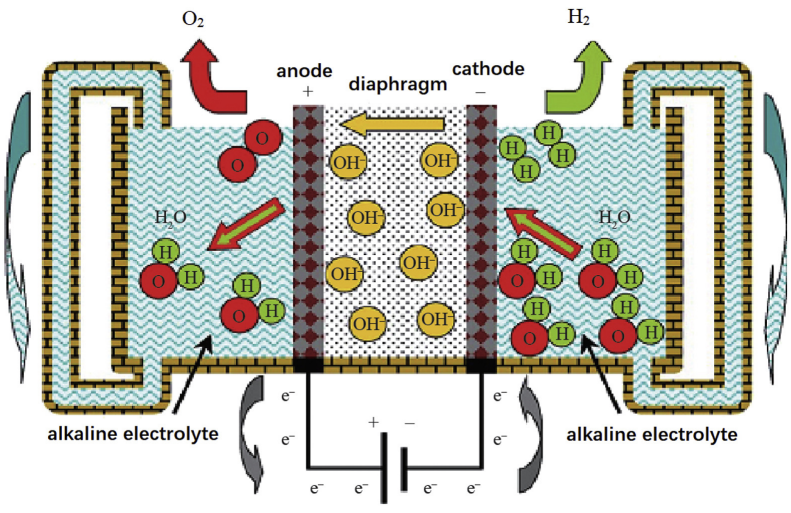

Figure 2.1: Working of an alkaline water electrolyser [17]. Current is applied across the diaphragm to produce hydrogen at the cathode and oxygen at anode. The electrolyte is an aqueous alkaline solution. The diaphragm ensures that the gases on the either side of the diaphragm do not mix inside the electrolyser.

The electrodes are separated by a separator which is permeable to hydroxyl ions and water molecules but not permeable to the gases produced at the either electrodes. By passing the right amount of voltage, the water

molecules are split into hydrogen and oxygen. Oxygen is generated at the anode and hydrogen is generated at the cathode in the form of bubbles. The bubble detaches from the electrode and rises to the top.

2.2. Thermodynamics of electrolysis

Current is passed through two electrodes that are dipped in water. By applying the right amount of potential across the electrodes, the following reactions occur,

$$\text{Anode}(+):\ 2OH^- \longrightarrow 0.5O_2(g)\ + H_2O\ + 2e^-\ (E^o = 0.400\text{V vs RHE @ pH} = 14) \tag{2.1}$$

$$\text{Cathode}(-):\ 2H_2O + 2e^- \longrightarrow H_2(g)\ + 2OH^-(E^o = -0.830\text{V vs RHE @ pH} = 14) \tag{2.2}$$

The voltages that are mentioned in the above equations are the reversible voltages. Usually, the conductivity of water is improved by either adding an acid or a base to the electrolyte. In the case of acid electrolysis, the environment is highly corrosive and hence, the electrodes used in such electrolysers are made of expensive materials like platinum.

In the case of alkaline electrolyser, cheaper materials like nickel can be used for the electrodes as corrosion issues are less significant with higher concentration of potassium hydroxide [6]. Typically, potassium hydroxide is used for improving the conductivity of the electrolyte. Up to 40 wt% of KOH in water is used to provide good conductivity up to temperature of 90°C [25]. Since the electrolyte is basic, the voltages corresponding to the pH values of basic solution are presented in the above equations.

The electrolysis of water is not thermodynamically favourable and requires energy input for the reaction to occur. The total energy required for the electrolysis to occur can be supplied by either heat or electricity. The energy requirements are estimated using the Gibbs equation given by,

$$\Delta G^o = \Delta H^o - T\Delta S^o \tag{2.3}$$

where G^o is the standard Gibbs free energy, H^o is the standard enthalpy of formation (286.03 kJ/mol), S^o is the ideal gas entropy (0.163 kJ $\text{mol}^{-1}\text{K}^{-1}$) and T is the temperature in Kelvin. The Gibbs energy of water at 298K is given by,

$$\Delta G^o = 286.03 - (298 \times 0.163) = 237.46\ \text{kJ/mol}$$

The voltage that has to be supplied for electrolysis can be calculated using the Gibbs free energy [12]. The voltage required is given by,

$$V_{\text{rev}} = -\frac{\Delta G^o}{nF} \tag{2.4}$$

where V_{rev} is the reversible voltage, G_{o} is the standard Gibbs free energy of formation of water, n is the number of electrons released per mole of hydrogen and F is the Faraday's constant. The number of electrons required to produce hydrogen is 2 and the Faraday's constant is 96485 C/mol. Using these values, the reversible voltage is calculated to be -1.23 V.

If the reaction has to occur at reversible voltage, the water that is reacting has to be in vapour phase. But in reality, the temperature of the water is lower than the evaporation temperature and hence, extra energy has to be supplied to the electrolyser [12]. The voltage at which the reaction has the necessary energy is called thermo-neutral voltage. The thermo-neutral voltage is given by,

$$V_{\text{tn}} = -\frac{\Delta H^o}{nF} \tag{2.5}$$

Using Equation 2.5, the thermo-neutral potential is -1.48V at 298K. Figure 2.2 shows the variation of the thermo-neutral voltage ($U_{\text{tn}}(T,1)$ in the figure) and reversible voltage ($U_{\text{rev}}(T,1)$ in the figure) with the temperature at 1 bar pressure.

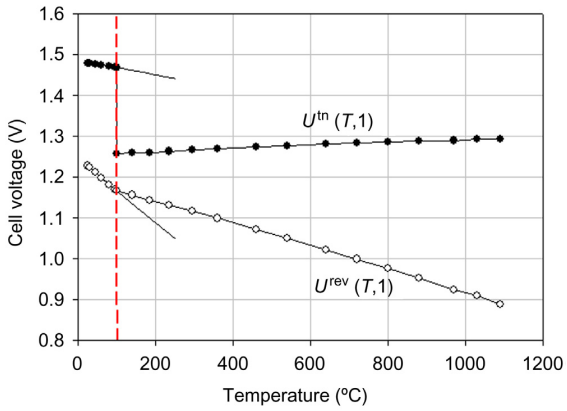

Figure 2.2: Variation of thermo-neutral voltage and reversible voltage with temperature [6]

The thermal characteristics of the reaction depend on the voltage that is supplied.

- If the supplied voltage is less than reversible voltage ($V < V_{rev}$), then the electrolysis does not take place.
- If the supplied voltage is equal to reversible voltage ($V = V_{rev}$), external heat has to be supplied to sustain the reaction.
- If the supplied voltage is higher than reversible voltage but less than the thermo neutral voltage, ($V_{rev} < V < V_{tn}$), the electrolysis is endothermic. This would mean that heat supply is still necessary, but the heat demand reduces as the supplied voltage approaches the thermo-neutral voltage.
- If the supplied voltage is equal to the thermo-neutral voltage ($V = V_{tn}$), the electrolysis occurs at constant temperature. There is no need for supply of external heat.
- If the supplied voltage is higher than the thermo-neutral voltage ($V > V_{tn}$), the electrolysis is exothermic. There is heat produced by the system and it has to be dissipated.

Figure 2.3 shows the graph containing regions specific to the thermal characteristic of electrolysis based on operating conditions.

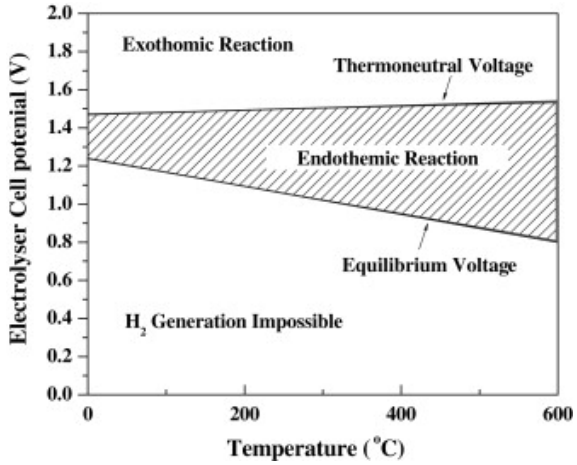

Figure 2.3: Thermal characteristics of electrolysis[40]. The preferable conditions are to operate the electrolyser at a voltage higher than the thermo-neutral voltage.

Low temperature electrolysers usually work in exothermic mode to satisfy the heat requirements with the internal heat generation [6]. The electrolyser being used is working with a supply voltage larger than the thermo-neutral voltage. Hence, it has to be verified if the heat dissipation is enough to run the electrolyser at the right temperature.

2.3. Losses in the electrolyser

Although water electrolysis is possible at thermo-neutral voltage (1.48 V), the actual reaction at this voltage is very slow. To split the water molecules in the electrolyser into hydrogen and oxygen, the voltage applied to the electrolyser must be significantly larger than the thermo-neutral voltage in order to let a significant current density flow across the cell and reduce capital expenses [25]. The potential applied over the thermo-neutral voltage to reach the corresponding current density is called over-potential. Some part of the over-potential is used to overcome the losses in the cell.

To explain the losses in the electrolyser, the electrical circuit analogy of water electrolyser [40] is used as shown in Figure 2.4.

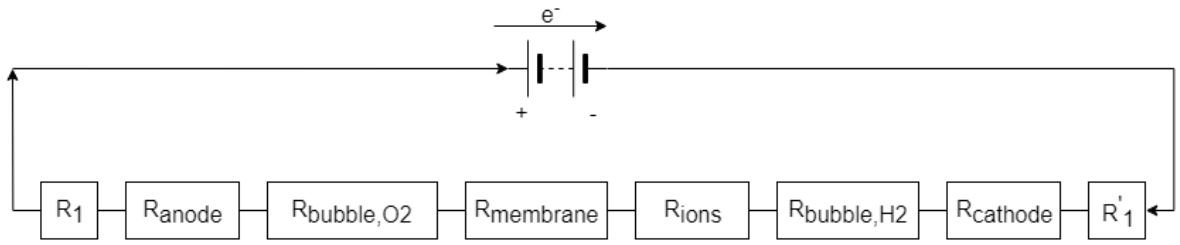

Figure 2.4: Losses in an electrolyser

Figure 2.5 shows the relative magnitude of each of the losses at various values of current density.

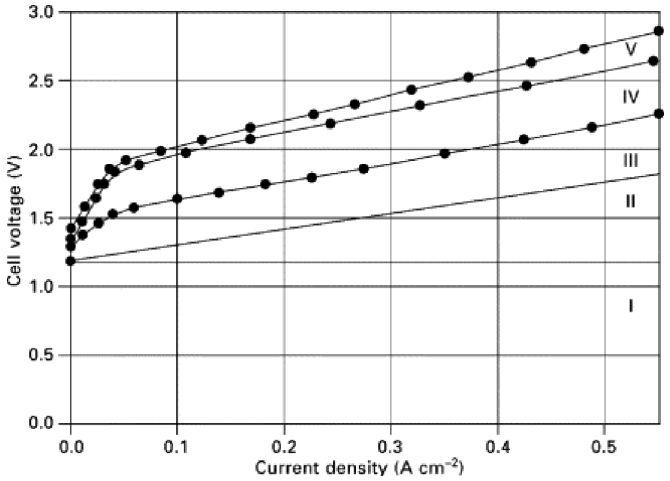

Figure 2.5: Contribution of different losses in an electrolyser. This is a plot of voltage versus current at 90°C. The curve shown by I is thermodynamic voltage, II is ohmic drop due to electrolyte, III is overpotential on anode side, IV is overpotential on cathode side, V is ohmic drop at the electrodes. [24]

2.3.1. Circuit resistances

Circuit resistances are the contributions made by the wiring and connections to the overall increase in the supplied voltage. These resistances are represented by R_1 and $R_1^{'}$ at the anode and cathode side respectively in Figure 2.4. These resistances can be calculated using Ohm's law (Equation 2.6) or using Equation 2.7.

$$R = \frac{V}{I} \tag{2.6}$$

$$R = \frac{l}{\kappa A} \tag{2.7}$$

In Equation 2.6, R is the effective resistance offered, and I is the current for supplied voltage V. In Equation 2.7, l is the length of the wires, κ is the specific electrical conductivity of the electrolyte and A is the area of cross section of the wires.

2.3.2. Transport resistances

Transport resistance is the physical resistance offered by the bubble formation and transportation in the electrolyser. During electrolysis, gas bubbles are formed at anode and cathode. If the bubbles cover the electrode, less surface area of the electrode is in contact with the electrolyte and this leads to a reduction in the efficiency of the electrolyser.

In Figure 2.4, R_{bubble,O_2} and R_{bubble,H_2} are caused as a result of oxygen and hydrogen bubbles covering the electrode. Resistance due to ionic transfer in the electrolyte is represented by R_{ionic} and resistance offered by the membrane is represented by $R_{membrane}$ in Figure 2.4.

2.3.3. Electro-chemical reaction resistances

Electro-chemical reaction resistances are the over potential values that are applied to the electrolyser to overcome the activation energies for the formation of oxygen and hydrogen at the electrodes. The surface parameters of the electrode play an important role in determining this over-potential. These resistances are represented as $R_{cathode}$ and R_{anode} in Figure 2.4.

The over-potential of hydrogen is measured by Tafel equation,

$$\eta_{H_2} = 2.3\frac{R_{const}T}{\alpha F_{const}}\log\frac{j}{j_0} \tag{2.8}$$

The exchange current density, j_0, is a function of the material used in the electrode [35]. Hydrogen over-potential is directly related to the hydrogen formed near the electrode. The hydrogen formation depends on concentration of electrolyte, temperature and electrode properties.

The over-potential of oxygen evolution reaction is generally measured by Tafel equation,

$$\eta_{O_2} = 2.3\frac{R_{const}T}{(1-\alpha)F_{const}}\log\frac{j}{j_0} \tag{2.9}$$

R used in both the equations is the universal gas constant (8.314 J/mol· K) The reaction rate is inversely proportional to the activation energy, so reducing activation energy is always favoured. The typical Tafel plots for the hydrogen and oxygen evolution reaction is shown in Figure 2.6.

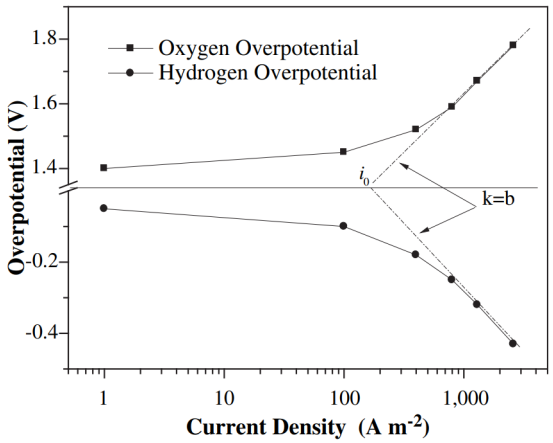

Figure 2.6: Typical Tafel plots for hydrogen and oxygen evolution [40]

The losses caused by the reaction resistances increases slowly with the rise in the current density. The energy loss in the circuit is relatively small. But the energy loss due to ionic transfer resistance becomes more relevant at higher current density. Generally, it is easier to reduce the hydrogen over-potential as compared to the oxygen over-potential due to the complex mechanism [8] and irreversibility of oxygen evolution reaction.

2.4. Bubbles and flow patterns

2.4.1. Forces acting on the bubble

The ZEF alkaline electrolyser does not have any external pumps to circulate the electrolyte within the system. Bubble formation and departure is one of the reasons for the electrolyte to be driven in the system. It also

one of the reasons for the losses in the electrolyser and hence, there is a need to learn the effects of it. The behaviour of gas bubbles and their effect on the cell voltage has been studied by Zhang et. al [41]. Figure 2.7 shows the forces acting on the gas bubble attached to the electrode.

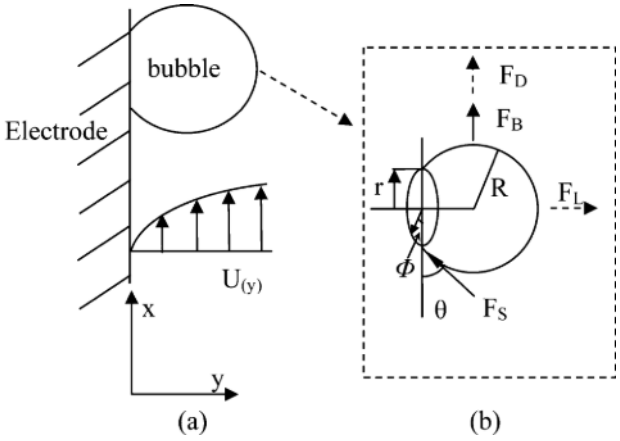

Figure 2.7: (a) Gas bubble on electrode and (b) forces acting on it

Due to the difference in gas and liquid densities, buoyancy and surface tension exist. If there is electrolyte flow, then, there is lift and drag force on the bubble. Due to the motion of the electrolyte, the contact angle is not same on all the sides of the bubble. The upward tilting of bubble leads to the formation of advancing and receding angles. The effect of temperature was not considered as the electrolyte was kept at the constant temperature. The force due to buoyancy is,

$$F_{\mathrm{B}} = \int_{A_B} p_{\mathrm{L}}(x)\,dA + \int_{A_C} p_{\mathrm{B}}\,dA - \int_{V_B} \rho_{\mathrm{B}} g\,dV \tag{2.10}$$

The drag force (F_D) and lift force (F_L) are given by,

$$F_{\mathrm{D}} = \frac{1}{2} C_{\mathrm{D}} \rho_{\mathrm{L}} v^2 A_a e_x \quad F_{\mathrm{L}} = \frac{1}{2} C_{\mathrm{L}} \rho_{\mathrm{L}} v^2 A_a e_y \tag{2.11}$$

where C_{D} is the drag coefficient and C_{L} is the lift coefficient. It was also found that surface tension is a function of electrolyte concentration gradient, pressure gradient, temperature gradient and voltage gradient. The temperature field and the bubble movement causes the bubble to depart prematurely.

2.4.2. Different multiphase flow patterns

The gas-liquid flow in the top channel can have different flow patterns. The common flow patterns are: bubbly, slug, annular and churn [21]. A representation of the different flow patterns are shown in Figure 2.8 [27].

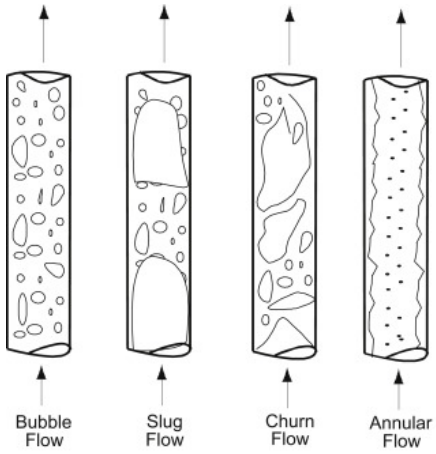

Figure 2.8: Vertical two phase flow patterns [27]

1. **Bubble flow** : When the liquid and gas velocities are low, the gas phase is dispersed in the liquid phase. This regime is called as bubble flow.

2. **Slug flow**: With larger gas velocities, the bubbles coalesce forming bubbles large enough to span across the cross-sectional area of the channel. This flow regime is called slug flow.

3. **Churn flow**: This type of flow pattern is seen when the continuity of the liquid in between two successive bubbles is broken repeatedly.

4. **Annular flow**: With further increase in the gas velocity, the gas phase becomes continuous and the liquid moves along with the bubble as a thin film in between the bubble and the wall. This flow regime is called annular flow

2.4.3. Pressure drop in the multiphase flow channel

The pressure drop in the channel where the multiphase flow of the electrolyte and the gases take place is given by [3] Equation 2.12.

$$\frac{\Delta P_{\text{ch}}}{L_{\text{ch}}} = \frac{2 f v_{\text{m}}^2 \rho_{\text{l}}}{d_{\text{ch}}} \alpha_{\text{l}} \tag{2.12}$$

where $\frac{\Delta P_{\text{ch}}}{L_{\text{ch}}}$ is the pressure drop per unit length of the channel, f is the friction factor given by Equation 2.13, v_{m} is the average of the gas and liquid velocity, ρ_{l} is the density of the electrolyte, d_{ch} is the diameter of the channel and α_{l} is the volume fraction of the electrolyte.

$$f = \frac{16}{\text{Re}} \left[1 + \frac{0.465 d_{\text{ch}}}{L_{\text{s}} \text{Ca}^{\frac{1}{3}}} \right] \tag{2.13}$$

where Re is the Reynolds number, Ca is the Capillary number given by Equation 2.14 and L_{s} is the length of the slug in the channel.

$$\text{Ca} = \frac{\mu_{\text{l}} u_{\text{g}}}{\sigma_{\text{l}}} \tag{2.14}$$

where μ_{l} is the dynamic viscosity of the electrolyte, u_{g} is the bubble velocity and σ_{l} is the surface tension of the electrolyte.

$$\frac{L_{\text{s}}}{d_{\text{ch}}} = 3451 \left[\frac{1}{\text{Re}_{\text{g}} \text{Eo}} \right]^{1.27} \tag{2.15}$$

where Re_{g} is Reynolds number calculated using the superficial gas velocity and Eo is Eotvos number or Bond number given by Equation 2.16.

$$\text{Eo} = \frac{(\rho_{\text{g}} - \rho_{\text{l}}) g d_{\text{ch}}^2}{\sigma_{\text{l}}} \tag{2.16}$$

2.5. Equation for void fraction/gas holdup

The driving force for the natural convection is due to bubbles and the void fraction is one of the parameters to be estimated. A simplified model to derive an equation for the average void fraction was given by Nagai et al [28]. Figure 2.9 shows the cut section of one half of the cell. The cathode is to the left of the image and the x coordinate is aligned with the electrode for the ease of deriving the equation. The electrolyte is blue in colour and the small element chosen in the electrolyte is white in colour. The height of the element is dx and the total height of the electrode is H_{cell} represented as H in Figure 2.9. The amount of hydrogen produced is proportional to the current density on the electrode. The volume flow rate of hydrogen gas (Equation 2.19) is given by Equation 2.17 [36] and Equation 2.18.

$$\dot{m}_{\text{H}_2}[mol/s] = \frac{jWdx}{nF} \tag{2.17}$$

$$PV = \dot{m}RT \tag{2.18}$$

$$\dot{m}_{\text{H}_2}[m^3/s] = \frac{RT}{P} \frac{jW}{2F} dx \tag{2.19}$$

where W is the width of the electrode, j is the current density, F is Faraday constant, P is the pressure of the system, T is the temperature of the system, R is the universal gas constant. The value of n is 2 as the number

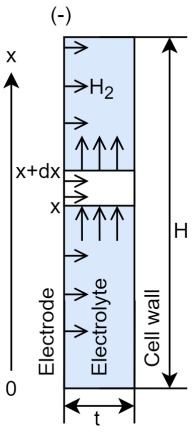

Figure 2.9: Cut section of half cell and orientation of coordinates in the void fraction derivation. The left line represents the cathode of the cell releasing hydrogen into the electrolyte (blue colour). The x coordinate of the system is aligned along the electrode for this derivation. The height of the electrode is H. Movement of the electrolyte is along the positive x direction.

of electrons from one mole of hydrogen is 2. Similarly, for the case of oxygen, the value of n is 4. The equation for volume flux of oxygen produced (in m^3/s) at anode is given by,

$$\dot{m}_{O_2} = \frac{RT}{P}\frac{jW}{4F}dx \tag{2.20}$$

Adding Equation 2.19 and Equation 2.20 gives the total volume flux of gas produced in the element at anode and cathode.

$$\dot{m}_{\text{total}} = \frac{3}{4}\frac{RT}{P}\frac{jW}{F}dx \tag{2.21}$$

The void fraction (α) depends on the coordinate x and if all the bubbles are assumed to have a constant velocity (v_g), the gas volume balance in the element is given by,

$$2utW(\alpha + d\alpha) = 2utW\alpha + \frac{3}{4}\frac{RT}{P}\frac{jW}{F}dx \tag{2.22}$$

This leads to,

$$d\alpha = \frac{3}{8}\frac{RT}{P}\frac{j}{Fut}dx \tag{2.23}$$

Solving for Equation 2.23, the void fraction is obtained as a function of the void fraction.

$$\alpha = \frac{3}{8}\frac{RT}{P}\frac{jx}{Fut} \tag{2.24}$$

The expression for the average void fraction is given by,

$$\alpha_{\text{av}} = \frac{1}{H_{\text{cell}}}\int_0^{H_{\text{cell}}} \alpha dx = \frac{3}{16}\frac{RT}{P}\frac{jH_{\text{cell}}}{Fut} \tag{2.25}$$

2.6. Scaling of resistances with the channel diameter

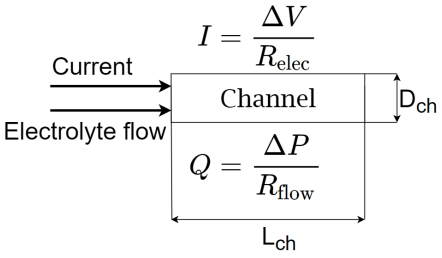

Figure 2.10: Representation of current and electrolyte flow in a segment of the system. The element offers resistance to the flow and the current. The electrical resistance scales with the square of the channel diameter whereas the flow scales with the fourth power of the diameter.

To find how the flow and electrical resistances scale with the channel hydraulic diameter, the Ohm's law and Hagen-Poiseuille equation are used. To obtain the Hagen-Poiseuille equation, the Darcy Weisbach equation is used. The Darcy-Weisbach equation [11] is given by,

$$\frac{\Delta P}{l_{\text{ch}}} = \frac{f \rho u^2}{2 D_{\text{ch}}} \tag{2.26}$$

Equation 2.26 relates the pressure loss per unit length of the channel ($\frac{\Delta P}{l_{\text{ch}}}$) to the channel diameter (D_{ch}). f is the friction factor which is $\frac{64}{Re}$ in the laminar flow case where Re = $\frac{\rho u D_{\text{ch}}}{\mu}$. The electrolyte flow rate $\dot{Q}_l$ is given by,

$$\dot{Q}_{\text{l}} = \frac{\pi D_{\text{ch}}^2}{4} u_{\text{l}} \tag{2.27}$$

Using Equation 2.26 and Equation 2.27,

$$\frac{\Delta P}{l_{\text{ch}}} = \frac{128 \mu \dot{Q}_{\text{l}}}{\pi D_{\text{ch}}^4} \tag{2.28}$$

Also, the flow rate of electrolyte is related to pressure drop by the equation,

$$\dot{Q}_{\text{l}} = \frac{\Delta P}{R_{\text{l}}} \tag{2.29}$$

Comparing Equation 2.28 and Equation 2.29,

$$R_{\text{l}} = \frac{128 \mu l_{\text{ch}}}{\pi D_{\text{ch}}^4} \tag{2.30}$$

To obtain the scaling of electrical resistance Pouillet's law gives,

$$R_{\text{elec}} = \frac{l_{\text{ch}}}{\kappa A} = \frac{4l}{\kappa \pi D_{\text{ch}}^2} \tag{2.31}$$

where R_{elec} is the electrical resistance of the channel, A is the cross sectional area of the channel, D_{ch} is the diameter of the channel and κ is the conductivity of the channel.

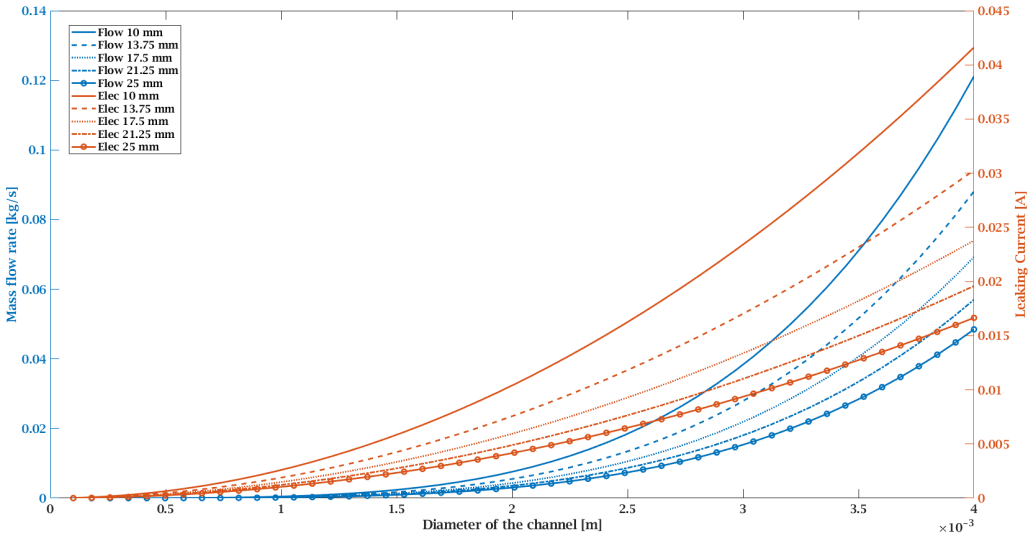

Figure 2.11: Variation of the mass flow rate and the leaking current with the diameter of the top channel. The mass flow and the leaking current are observed to raise continuously with the channel diameter but decreases with the length. Hence, an optimal point has to be found to balance both the parameters.

The leaking currents have to be minimised and the flow rate has to be maximised. This leads to maximising R_{elec} and minimising R_{l}. If the diameter is decreased by a factor of 2, the electrical resistance increases by a

factor of 4, but the resistance to the flow increases by a factor of 16. Figure 2.11 shows the effect of the length and diameter of the channel on leaking currents and mass flow rate of the electrolyte. The leaking currents and the mass flow rate increase with the diameter of the channel and the flow rate is more sensitive to the diameter of the channel. The different values of the channel length considered are mentioned in the legend.

The current design was built around the idea of decreasing the leaking currents and hence, the diameter of the channels are made as small as possible. The effect of this channel diameter has been investigated in the upcoming chapters.

2.7. Equation for the heating curve

The thermal behaviour of the electrolyser with respect to time had to be determined for looking at whether the system reaches the expected temperature during operation. The heat supplied to the electrolyte is lost through the PMMA. Here, it is assumed that the initial temperature of the system is not the same as the ambient temperature. The heat balance of the electrolyser for one half of the cell is given by,

$$Q_{\text{elec}} = \rho_{\text{l}} A x c_{\text{p}} \frac{dT}{dt} + h_{\text{c,air}} A (T(t) - T_{\text{env}}) \tag{2.32}$$

where Q_{elec} is the heat supplied at the electrode , ρ is the density of the electrolyte, x is the thickness of the cell, c_{p} is the specific heat at constant pressure of the electrolyte, $h_{\text{c,air}}$ is the heat transfer coefficient of natural convection for air which will be used as h in the derivation, T_{env} is the ambient temperature and A is the area of the electrode. The equation is rearranged and integrated for obtaining the relation between time and the temperature of the electrolyte.

$$\frac{dT}{dt} = -\frac{hA}{\rho_{\text{l}} A x c_{\text{p}}} \left[T - \left(\frac{Q_{\text{elec}}}{hA} + T_{\text{e}} \right) \right] \tag{2.33}$$

$$\frac{dT}{\left[T - \left(\frac{Q}{hA} + T_{\text{e}} \right) \right]} = -\frac{hA}{\rho_{\text{l}} A x c_{\text{p}}} dt \tag{2.34}$$

Let the temperature at time t = 0 be T_0. Integrating from t = 0 to t = t,

$$\ln\left[T - \left(\frac{Q_{\text{elec}}}{hA} + T_{\text{e}} \right) \right] - \ln\left[T_0 - \left(\frac{Q_{\text{elec}}}{hA} + T_{\text{e}} \right) \right] = -\frac{ht}{\rho_{\text{l}} x c_{\text{p}}} \tag{2.35}$$

$$\frac{\left[T - \left(\frac{Q_{\text{elec}}}{hA} + T_{\text{e}} \right) \right]}{\left[T_0 - \left(\frac{Q_{\text{elec}}}{hA} + T_{\text{e}} \right) \right]} = e^{\frac{-ht}{\rho_{\text{l}} x c_{\text{p}}}} \tag{2.36}$$

$$T = \left(\frac{Q_{\text{elec}}}{hA} + T_{\text{e}} \right) + \left[T_0 - \left(\frac{Q_{\text{elec}}}{hA} + T_{\text{e}} \right) \right] e^{\frac{-ht}{\rho_{\text{l}} x c_{\text{p}}}} \tag{2.37}$$

Steady state temperature (T_∞) is reached when the temperature does not change anymore. This condition is substituted in Equation 2.32 to obtain the condition for the steady state temperature,

$$Q_{\text{elec}} = hA(T_\infty - T_{\text{e}}) \tag{2.38}$$

$$T_\infty = \frac{Q_{\text{elec}}}{hA} + T_{\text{e}} \tag{2.39}$$

Using this result in Equation 2.37,

$$T = T_\infty + [T_0 - T_\infty] e^{\frac{-ht}{\rho_{\text{l}} x c_{\text{p}}}} \tag{2.40}$$

$$T = T_\infty + [\Delta T] e^{-kt} \tag{2.41}$$

where T is the temperature value at time t, ΔT is the difference between initial temperature and final temperature and $k = \frac{h}{\rho_{\text{l}} x c_{\text{p}}}$ is a constant with unit s^{-1}. This shows that the curve resulting from the equation takes the form of an exponential recovery curve.

2.8. Characterisation parameters

The two main parameters to be measured are:

- Temperature
- Velocity of KOH solution

2.8.1. Temperature

To measure the temperature in various parts of the alkaline electrolyser, thermistors are used. A thermistor is a type of resistor whose resistance is sensitive to temperature [5]. Assuming first order approximation and linear relationship between temperature and resistance,

$$\Delta R = k\Delta T \tag{2.42}$$

where ΔR is the change in resistance, k is the first order temperature coefficient and ΔT is the temperature change. If k value is positive, then the thermistor is called a positive temperature coefficient thermistor. If the k value if negative, the thermistor is called a negative temperature coefficient thermistor and the resistance of the thermistor deceases with the increase in temperature. I had used the temperature sensors in the setup to measure the temperature at various locations of the setup.

2.8.2. Velocity of KOH solution

To obtain the velocity of the electrolyte, fluorescent particles were used which track the flow and can be distinguished from other elements in the frame like the electrode and bubbles. Fluorescent particles have the ability of absorbing light from different wavelength and emitting a spectrum of light with different wavelength [31].

Particle Tracking Velocimetry (PTV) was used to obtain the velocity of the particles. PTV is one of the forms of pulsed light velocimetry [34] techniques where the position of the particle is tracked and expressed as a function of time. Different image processing techniques can be used for improved object identification like boundary thresholding [2].

2.9. ZEF alkaline electrolyser

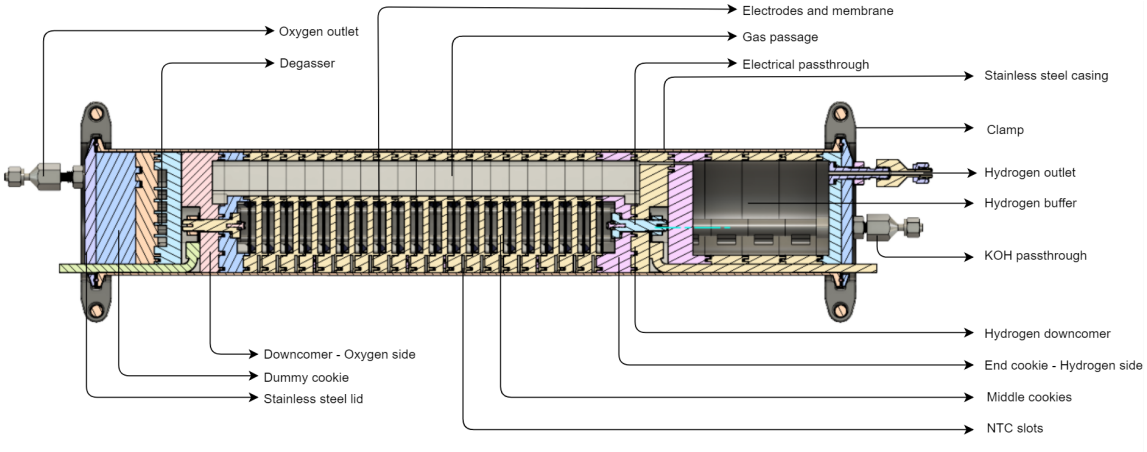

Figure 2.12: Cross section view of the full electrolyser design

The alkaline water electrolyser at ZEF is used to produce hydrogen gas from water at 50 bar. The input to the electrolyser contains a mixture of water and carbon dioxide. The output contains hydrogen. KOH is present in the electrolyser and is added or removed based on the liquid level in the electrolyser.

Figure 2.12 gives the cross section view of the electrolyser showing the components that are in the electrolyser. For reference purposes, the side of the electrolyser where the oxygen comes out is called the oxygen side and that where the hydrogen comes out is called the hydrogen side. There are 19 yellow identical components at

the centre of the system. Each one of these is called as a 'cookie' and will be referred that way in the rest of the report. Each cookie has a wall separating two successive electrolysis cells and two successive cookies make up one cell with the electrode and separator assembly in between.

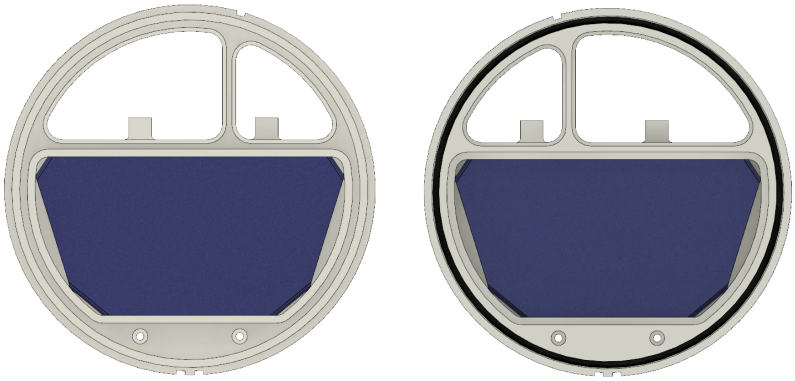

(a) Front view (b) Rear view

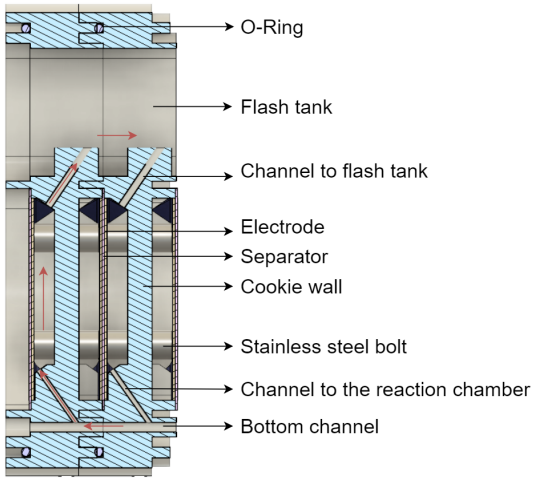

(c) Cut section view

Figure 2.13: Various views of the middle cookie. (a) shows the front view of the cookie with the electrode (blue in colour). (b) shows the rear view of the cookie with the electrode and the O-Ring (black) used to make the system leak-tight at higher operating pressures. (c) shows the cut section view of two cookies assembled. Red arrows in (c) show the direction of the electrolyte flow.

- **External casing**: The external casing consists of three components: tube casing, lids and the clamps. The material used for the external casing is stainless steel. The clamps are used to seal the lids with the tube. The lids have holes for the pass-throughs and the electrical cables.
- **Pass-through**: The pass-throughs are used for allowing fluids to enter or leave the system. There are four pass-throughs in total: hydrogen pass-through, oxygen pass-through, KOH pass-through and water pass-through. Water pass-through is used to supply water to the system that enters to the degasser before being sent to the middle cookies. Hydrogen pass-through and KOH pass-through are present on the hydrogen side and the oxygen pass-through and the water pass-through are present on the oxygen side.
- **Dummy cookie**: Dummy cookie is the cookie present between the lid and degasser that provides support to the pass-throughs on the oxygen side.
- **Degasser**: Degasser is used to reduce the percentage of carbon dioxide in the water supplied to the electrolyser. The oxygen produced in the electrolyser is passed through the water that is supplied into the electrolyser. When oxygen moves through the water containing CO_2, some of the CO_2 moves from water to oxygen. In this way, the purity of water is increased before it undergoes electrolysis.

- **Down-comer cookies**: When the gases are evolved during electrolysis, they carry some of the electrolyte along with them. Hence, some electrolyte ends up in the flash tank. This is brought back to the bottom of the setup through the downcomer cookies. The downcomer cookie on the oxygen side contains the level sensor. The level sensor is used to monitor the level of KOH and control the valves at the KOH pass-through and the water inlet.

- **Middle cookies**: The middle cookies are the main part of the electrolyser which contain the electrodes, separators and the electrolyte. This it the place where the water is split into hydrogen and oxygen. Figure 2.13 shows the different views of the middle cookie. The front view (Figure 2.13a) shows the electrode which is blue in colour, flash tank on the hydrogen and oxygen side at the top and the channels at the bottom to feed the electrolyte into the reaction chamber.

  The back side of the middle cookie is shown in Figure 2.13b. O-ring is seen at the back of the cookie. The flow of the electrolyte is shown in Figure 2.13c with red arrows. O-rings between two middle cookies are present to make sure that there are no leaks at high pressure. One side of one middle cookie and the one side of the other middle cookie make up for one electrolysis cell.

- **Flash tank / gas passages**: In the flash tank, the hydrogen is present in the hydrogen flash tank channel and is removed from the right side of the electrolyser. Similarly, oxygen is removed from the left of the electrolyser which is present in the oxygen flash tank channel. There is also electrolyte flowing into the flash tank from the cell through the top channels.

- **Electrodes and separators**: Every middle cookie contains two electrodes on either face and the end cookies contain one electrode. The electrode is made of Nickel mesh with Permascand coating. The electrode is a mesh and hence, allows the membrane to be in contact with the separator. Electrical connection is completed by passing the electricity from the electrical pass-through in the end cookies to the electrodes using stainless steel studs. Every middle cookie is provided with four such studs for the electrical connection.

  The separator is Agfa Perl UTP-500. The separator is placed in between every middle cookie and makes sure that the gases evolved at the electrodes do not mix. Hydroxyl ions are the charge carriers and they pass through the separator. Zero gap configuration is used in the setup. Hence, the electrodes are in contact with the separator.

- **End cookies**: The end cookies are the two cookies present in between the middle cookie stack and the down-comers. On one side, they have the same features as the middle cookies and on the other side, they have the other half of the down-comer. They are also thicker to house the electrical pass-through bolt. Power is supplied through cables, electrical pass-through bolts and to the stainless steel studs.

- **Hydrogen buffer**: After hydrogen is produced by electrolysis, it is stored in the buffer until it is being required by the downstream processes.

- **NTC slots**: NTC slots are used to house the temperature sensors in the system Every middle cookie consists of one slot at the bottom and one slot at the top so that the temperature sensors can be placed wherever necessary.

2.10. Setup description

Due to safety reasons, the full setup was not ready to be functional and thus, could not be characterised. Hence, a smaller setup with same geometry was used for observing the flow and temperature profile during operation. Figure 2.14 shows the front view of the setup that was designed using Adobe Fusion 360. The cookies were manufactured by Pieter from ZEF and the rest of the setup was done by me.

The bubble evolution and motion was observed from this view using a high speed camera. More information related to this part of the setup is presented in chapter 3. The cookie was adjusted so that the flow inside the channels is also observed. Hence, two square channels with the hydraulic diameter equal to that of the actual channel along with the angle of inclination same as that of the actual channel was designed.

Five bolts are seen from the front. The bolt in the centre is the bolt that provides the electrode (purple colour sheet) with the electricity. The remaining four bolts are used for pressing the electrode against the membrane

ensuring zero gap configuration during operation. Depending on the polarity of electricity on the bolt, the part of the cell under observation can be hydrogen side or oxygen side.

The path taken by the flow is same as that of the actual setup: 30% KOH solution enters cell from the bottom channel through the square channel at the bottom and passes along the electrode, generating gas bubbles. The flow then enters the upper channel to reach the flash tank.

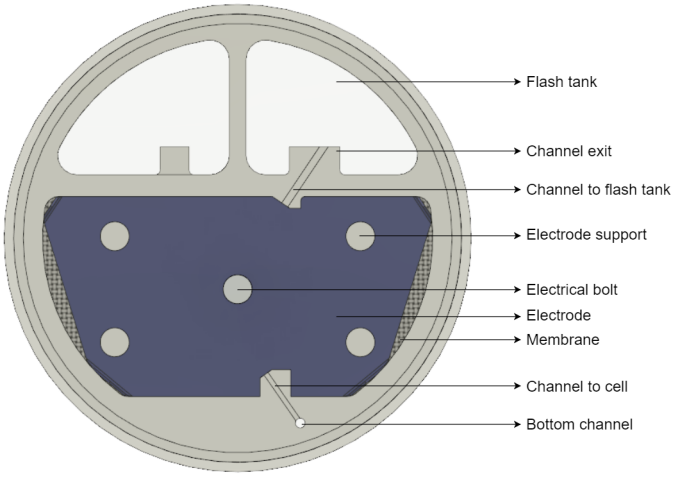

Figure 2.14: Front view of the setup

Figure 2.15 shows the other side of the setup which consists of the down-comer and the other bolt that works as the electrical pass-through for the other electrode. There are two down-comers on either side of the bolt with the down-comer on the left side being present for the flow seen on the front side of the setup and the down-comer on the right side being present for the flow through the other side of the membrane.

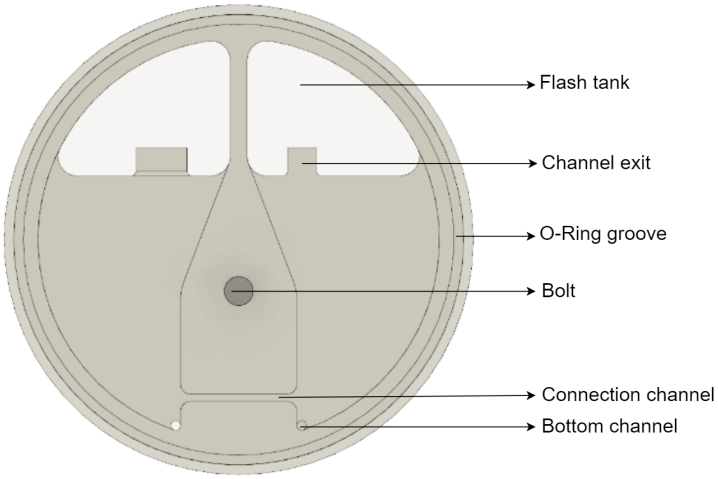

Figure 2.15: Back view of the setup

This setup totally consists of one electrolysis cell with two electrodes and one membrane in zero gap configuration, two stainless steel bolts for electrical connection, two CPVC cookies for the body of the electrolysis cell and two PMMA covers on either side of the setup for transparency. Figure 2.16 shows all the components mentioned. O-rings are necessary if the system is operated at higher pressure. Hence, O-ring grooves were machined.

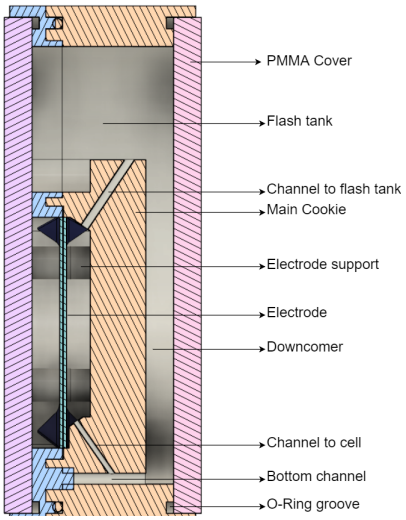

Figure 2.16: Cut section view of the test setup. The zero gap configuration is achieved by pressing the electrode-separator on either sides with the supports. The passage to the right of the electrode-separator assembly is the oxygen side and the one to the left is the hydrogen side.

The location of the temperature sensors are not shown in the 3D drawing of the setup. There are two temperature sensors on either side of the setup. A hole is made on PMMA cover for every temperature sensor. The sensitive part of the NTC is kept in the flow whereas the connecting ends of the NTCs are present on the outside of the setup. The terminals of the NTC are connected to and controlled by an Arduino controller.

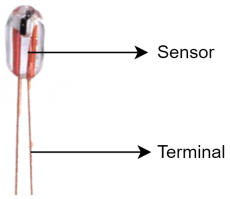

Figure 2.17: Temperature sensor used in the setup. The actual sensor is placed in contact with the electrolyte and the terminals are soldered with electrical wires to be connected with the rest of the circuit. Four temperature sensors were used in total.

The temperature sensor used in the setup is shown in Figure 2.17. The faces of the PMMA cover is shown in Figure 2.18. Several holes and engravings were done on the PMMA covers. The holes are made for housing the stainless steel bolts (shown as bolt hole) and the temperature sensors. In both the PMMA covers, there are two small holes of 2 mm diameter which hold the temperature sensor. The hole is made leak proof and the temperature sensor is held by means of epoxy glue. The advantage of using epoxy glue is that it is transparent and hence, it does not block any visual information from inside.

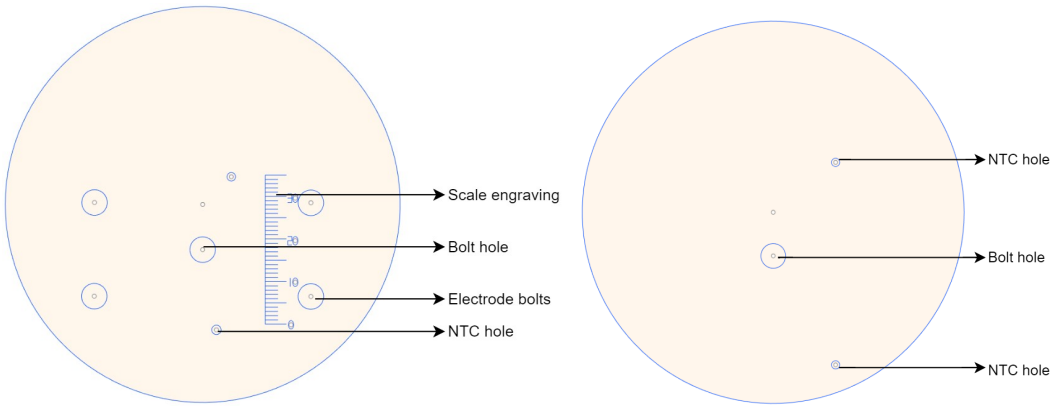

(a) Front cover (b) Back cover

Figure 2.18: Front and back PMMA covers showing various holes and engravings on them

In Figure 2.18a, all curves except the bolt hole, NTC hole and the actual circle marking the diameter of the PMMA cover are engraving lines. The scale is used to scale the images and videos to the right size when post processing it. The electrode bolts are also made from PMMA so that they are transparent. The marking is done on the PMMA cover so that the location at which the bolts have to be stuck are made obvious.

In Figure 2.18b, all the curves are cutting curves and the PMMA engraving and cutting was done using a laser cutting machine. The laser cutting is done with high power for the curves which are supposed to be cutting curves and for the ones which are meant to engraved, the laser operates at lower power making an engraving roughly 0.2 mm deep.

3

Initial analysis, modelling and experiments

The are two main factors that affect the temperature distribution are advection and diffusion of heat. The source of heat is at the electrodes. The electrolyser heats up whenever the supplied voltage is greater than the thermo-neutral voltage (1.48 V in this case). The effect of diffusion was studied using the simulation option available in Adobe Fusion 360 and the other effects were analysed in the Matlab model. This section contains the initial analysis and description of the simulations done using Matlab and Comsol. The information related to experiments are also mentioned in this section.

3.1. Advection-diffusion equation

The advection-diffusion equation was solved for the current system to see the temperature profile in the system due to conduction and convection. The electrolysis system is opaque and one of the options to quantify the flow inside the system was to use the already existing temperature sensors. For this method to be reliable, the relative dependence of temperature on advection and diffusion had to be studied. The advection-diffusion equation is given by,

$$\frac{dT}{dt} = -u\frac{dT}{dz} + \alpha\frac{d^2T}{dz^2} + S \tag{3.1}$$

where u is the velocity of the fluid, T is the temperature, z is the vertical distance with z = 0 being the bottom of the electrode and z = H being the top of the electrode, α being the thermal diffusivity of the fluid and S being the volume heat flux that is heating the fluid. The steady state solution is obtained when the temperature stays constant with time. This would mean that the left hand side of equation 3.1 becomes zero. Equation 3.1 is then,

$$u\frac{dT}{dz} = \alpha\frac{d^2T}{dz^2} + S \tag{3.2}$$

General solution to equation 3.2 is,

$$T(z) = \frac{\alpha e^{\frac{uz}{\alpha}} c_1}{u} + \frac{Sz}{u} + c_2 \tag{3.3}$$

3.1.1. Between z=0 and z=H

The heat source S is at the electrode as the heating happens due to the Joule effect. Hence, equation 3.3 has a positive value for S between z=0 and z=H and zero everywhere else. Let the temperature at z=0 be T_0. Using this condition, equation 3.3 becomes,

$$c_2 = \frac{uT_0 - \alpha c_1}{u} \tag{3.4}$$

$$T(z) = \frac{\alpha e^{\frac{uz}{\alpha}} c_1}{u} + \frac{Sz}{u} + \frac{uT_0 - \alpha c_1}{u} \tag{3.5}$$

AT z=H, $\frac{dT}{dz} = 0$

$$c_1 = -\frac{S}{ue^{\frac{uH}{\alpha}}} \tag{3.6}$$

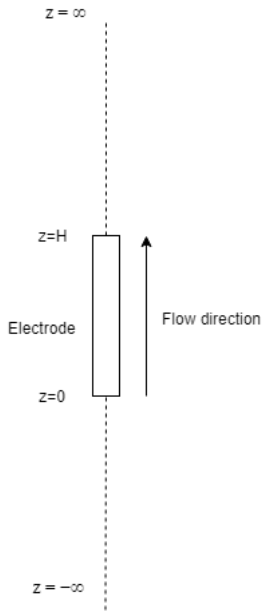

Figure 3.1: Representation of the z axis in the flow

Equation 3.3 becomes,

$$T(z) = -\frac{\alpha S}{u^2} e^{\frac{u(z-H)}{\alpha}} + \frac{\alpha S}{u^2 e^{\frac{uH}{\alpha}}} + \frac{Sz}{u} + T_0 \tag{3.7}$$

At z = H, T = T_H,

$$T_H = -\frac{\alpha S}{u^2} + \frac{\alpha S}{u^2 e^{\frac{uH}{\alpha}}} + \frac{SH}{u} + T_0 \tag{3.8}$$

3.1.2. Between z = $-\infty$ and z = 0

At z = $-\infty$, T=$T_{-\infty}$. Equation 3.3 becomes,

$$T_{-\infty} = c_2 \tag{3.9}$$

$$T(z) = \frac{\alpha e^{\frac{uz}{\alpha}} c_1}{u} + T_{-\infty} \tag{3.10}$$

At z = 0, T=T_0

$$c_1 = (T_0 - T_{-\infty})\frac{u}{\alpha} \tag{3.11}$$

$$T(z) = e^{\frac{uz}{\alpha}}(T_0 - T_{-\infty}) + T_{-\infty} \tag{3.12}$$

3.1.3. Between z = H and z = ∞

The temperature at z = H is T_H. The temperature beyond z = H cannot increase because there is no heat source and the temperature cannot decrease because there are no heat losses taken into consideration. This means that the temperature is constant beyond z = H. Hence, the equation for temperature profile becomes,

$$T(\mathrm{H} < z < \infty) = T_\mathrm{H} \tag{3.13}$$

3.1.4. Plotting the temperature profile

The temperature profile is plotted using the equations 3.7, 3.12 and 3.13 for different parts of the flow. The dimensionless number that relates the convective heat transport to the diffusive heat transport is the Péclet number [33]. Péclet number is defined as,

$$\mathrm{Pe} = \frac{uH}{\alpha} = \frac{\text{Convection transport}}{\text{Diffusion transport}} \tag{3.14}$$

where H is the height of the electrode, u is the velocity of the electrolyte and α is the thermal diffusivity of the electrolyte. Using the velocity as input, the dependence of temperature profile on Péclet number is obtained

and plotted in Figure 3.2. The various colours of the plot are the various locations in the electrolyser. Red colour is when the flow has not entered the cell yet, blue colour is when the flow is in the cell and green colour is after the cell. The temperature before the electrolyte increases with the decrease in Péclet number as diffusion becomes more significant. The y axis is normalised for better comparison of the different cases. In all the three cases, the temperature beyond the electrode is constant.

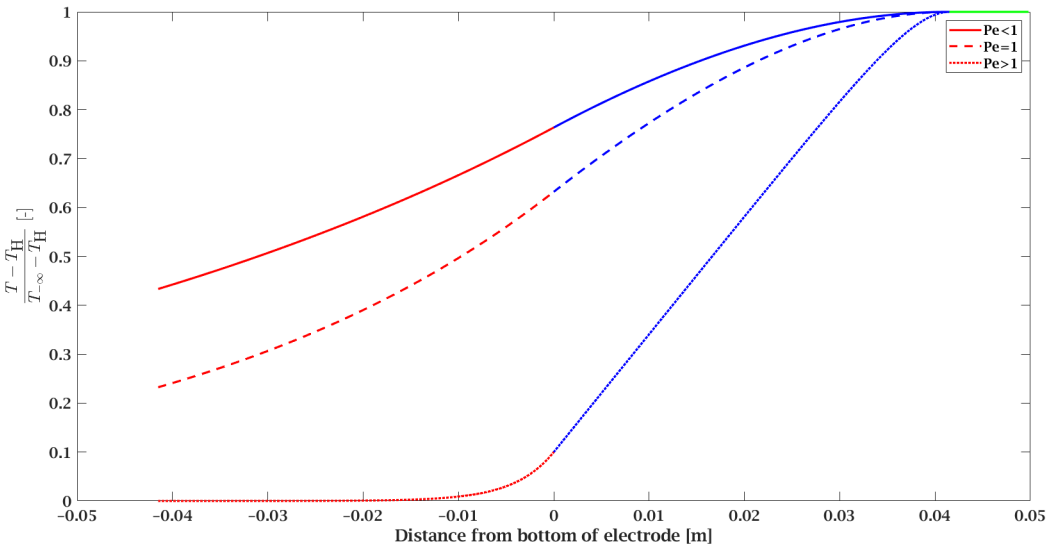

Figure 3.2: Temperature profile for various values of Péclet number. Every temperature profile is split into three parts: red part being before the electrode, blue part being at the electrode and the green part being after the electrode. The temperature rise due to the convection is more significant with the increase in the Peclet number.

3.2. Fusion 360 modelling

Adobe Fusion 360 software used for designing the system consists of a thermal analysis module which was used in the initial analysis. The software does not have a flow module in it. Hence, two extreme cases could be simulated: zero flow case and high flow case by modifying the thermal conductivity of the electrolyte.

Table 3.1: Parameters used for the simulation

Parameter	Value	Units
Heat generated	5.2	W
$h_{c,air}$	5	W/m^2K
T_{env}	20	°C
λ_l	0.637	W/mK
λ_{high}	5000	W/mK
ρ_l	1280	kg/m^3
$c_{p,l}$	2950	W/m^2K

Table 3.1 gives all the parameters required to run the simulation. The heat generated is provided at the electrode and separator assembly. The heat (Q) generated by the system is given by the formula,

$$Q = (V - V_{tn}) \times I = (2 - 1.48) \times 10 = 5.2\text{W} \tag{3.15}$$

where V is the supplied voltage, I is the supplied current and V_{tn} is the thermo-neutral voltage. The natural convective heat transfer coefficient of air is obtained from [20]. The thermal conductivity of the electrolyser is modified for the different cases. When the thermal conductivity is equal to that of 30% KOH (λ_l), the zero flow case is simulated and when the same value is kept at maximum (λ_{high}), the high flow case is simulated. This analysis also shows if the system is in safe limits when there is no flow in the electrolyser. T_{env} is the ambient temperature.

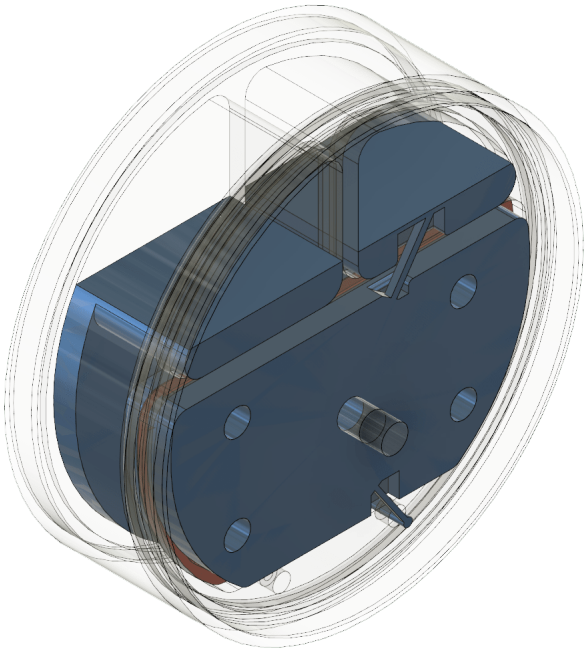

Figure 3.3: 3D view of the flow domain in the electrolyser setup. The blue colour is the flow domain in the setup and red colour is the part where the heat is supplied. The rest of the setup is made transparent in the figure for better visibility.

Figure 3.3 shows the setup with the flow domain shown in blue colour. The heat is supplied on the electrode separator assembly which is shown in red colour. The rest of the setup is made transparent so that a clear view of the inside is obtained.

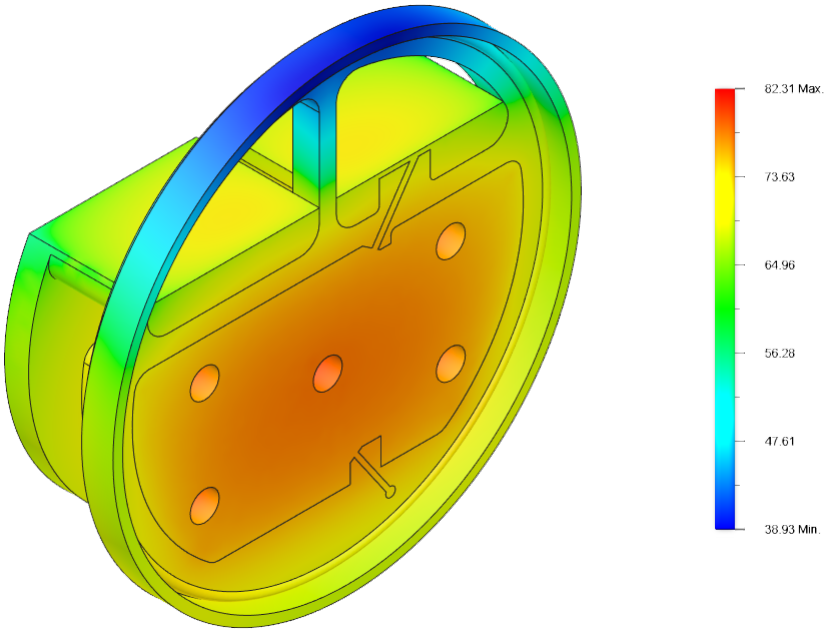

Figure 3.4: Temperature profile of the zero flow case. The maximum temperature is 82°C at the cell and the temperature is almost constant at the down-comer. There is a significant temperature difference across the top and bottom channel.

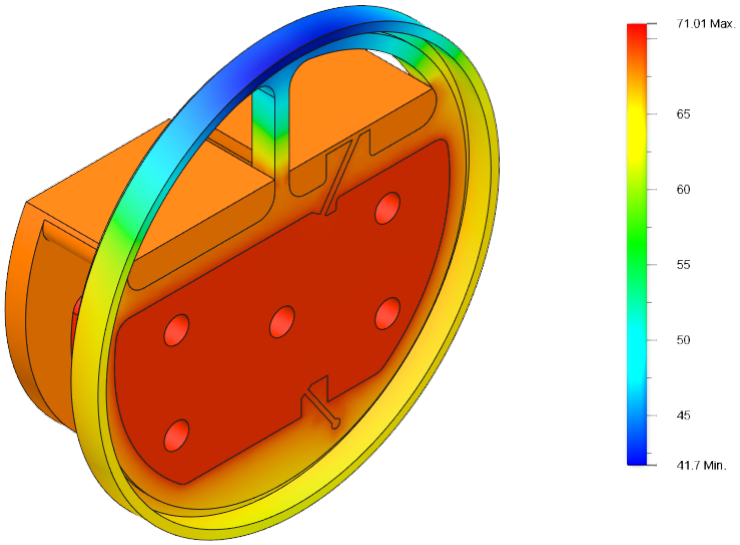

Figure 3.5: Temperature profile of the high flow case. The temperature in the system is lower and more uniform.

Figures 3.4 and 3.5 show the results of the simulation for the low and high thermal conductivity. The temperature difference between the electrolyte inside and outside the cell is greater in the low thermal conductivity than in the high thermal conductivity case. Figure 3.4 shows that the maximum temperature of the system would be at 82°C. This means that in a situation where there would not be any flow in the system, the system does not exceed the melting point of PVC [39].

3.3. Matlab modelling

3.3.1. Introduction and results from previous work

Matlab modelling was done for characterising the electrolyser by M.Geraedts [18]. The basis of the model was the electrical circuit analogy for determining the flow and electrical parameters in various parts of the system. For evaluating the flow parameters, hydrodynamic force balance is done and for obtaining the electrical parameters, an electrical circuit is built and solved.

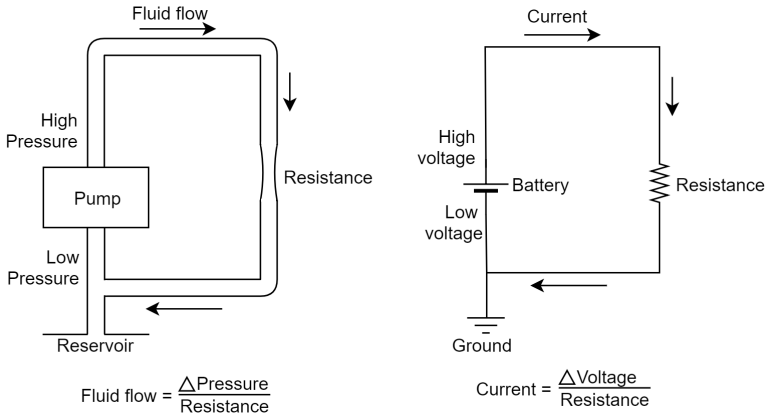

Figure 3.6: Analogy between the fluid flow circuit (left) and the electrical circuit (right). The laminar fluid flow is analogous to the electrical current and the pressure is analogous to electrical voltage. Fluid flow in the figure represents the volumetric flow rate of the fluid.

Figure 3.6 shows the electrical-hydraulic analogy. A laminar flow circuit is analogous to an electrical circuit where the flow rate of the electrolyte is the current, pressure at different points in the system is the voltage and friction is the resistance in the circuit. The algorithm of the code is explained in the Figure 3.7.

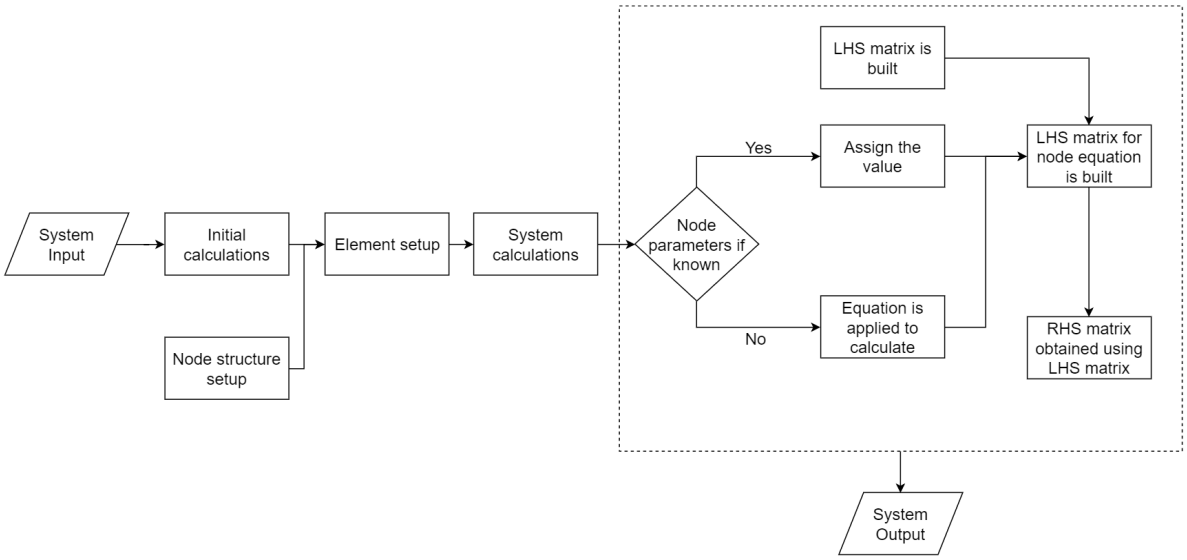

Figure 3.7: Representation of the algorithm for the matlab code. The nodes and elements were defined and the electrical analogy network was solved for electrical and flow case. The equations applied depend on the physics for which the network is built.

A set of linear equations are obtained for every node and element in order to calculate the unknown parameters. The final matrix is of the form

$$\mathbf{A}x = \mathbf{B} \tag{3.16}$$

where **A** is the LHS matrix and **B** is the RHS matrix described in Figure 3.7. x is the matrix containing all the parameters of the system like voltage, pressure, resistance, current and flow rate.

The system parameters like temperature and pressure are defined along with the dimensions of various channels of the system. The hydraulic diameter for all these channels are also calculated for the hydrodynamic force balance. Ohm's law and Kirchoff's law are used in the electrical parameter calculations at nodes. In order to estimate the power loss, Joule's law was used with the voltage and current information that was calculated previously.

In the case of estimating the hydrodynamic parameters, Hagen-Poisuelle equation was used to determine the initial K value (resistance to the flow) and the mass flow rate is determined. The mass flow rate from laminar model was used to calculate the Reynolds number. Darcy friction factor was estimated using Churchill equation and turbulent K values (resistance to the flow) were calculated. The mass flow rate was calculated with these values and the velocity at various parts of the system is estimated.

Figure 3.8 shows the result of the hydrodynamic calculations of the Matlab code. The system simulated has 5 cells with 2 down-comers on either side. The hydrogen side (blue colour) and oxygen side (red colour) have their values of pressure at each node and velocity at every element. The elements which are black in colour represent the small channel connecting the electrolyte on the anode and the cathode side.

In this model, only the effect of bubbles on the flow rate has been estimated. Void fraction was included to account for the density change in the electrolyte due to bubbles and the flow rates were obtained for those density values. The effect of temperature and change in the density of electrolyte as a result of change in temperature is not taken into account. With only the influence of bubbles taken into account, Table 3.2 provides the results from the model simulated by M.Geraedts.

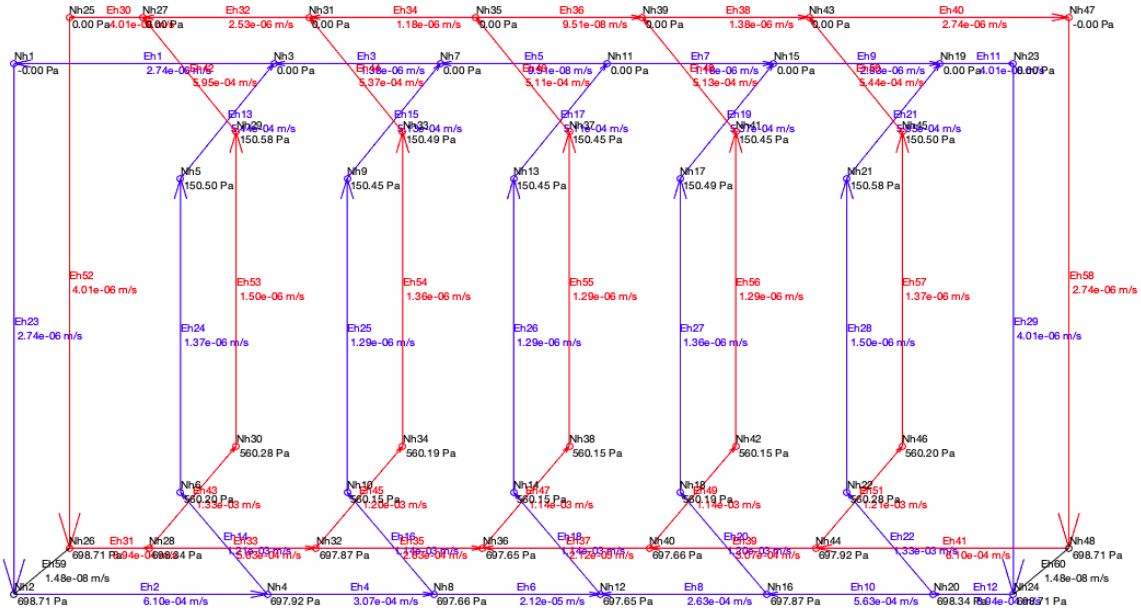

Figure 3.8: Hydrodynamic network result of the Matlab model with 5 electrolysis cells and 2 down-comers on the either side [18]. This figure shows the flow velocity at different parts of the system. The pressure at each node is also indicated. The vectors and nodes coloured in blue represent the hydrogen side of the system and the ones in red represent the oxygen side. Nh denotes nodes and Eh denotes element with a unique number given to every node and element in the system.

Table 3.2: Results from the matlab model [18]

Parameter	Value	Unit
Bubble diameter	0.18	mm
Mass flow rate	2.01×10^{-6}	kg/s
Average velocity	1.39×10^{-6}	m/s
Leaking current efficiency	98.45	%
Void fraction	0.94	%
Average current	11.3	A
Bypass current	0.175	A

3.3.2. Modifications and preliminary analysis on the Matlab model

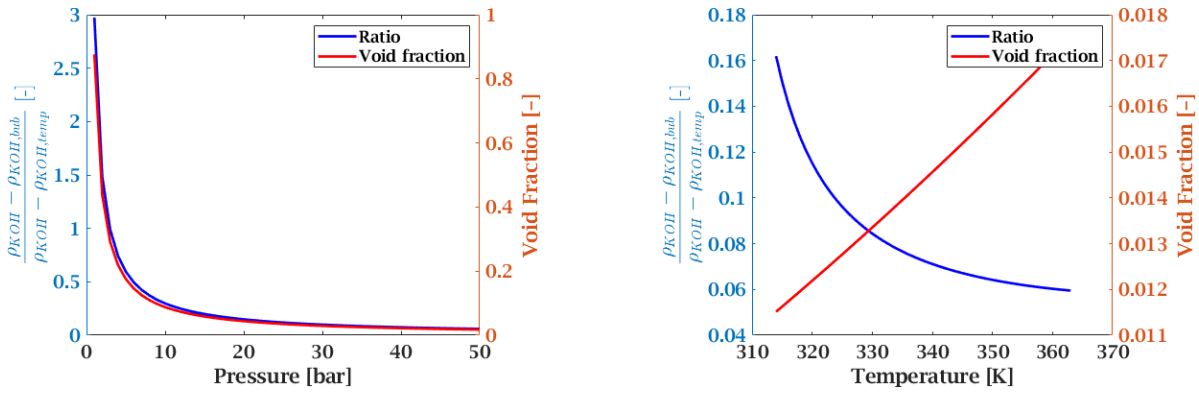

(a) Effect of pressure

(b) Effect of temperature

Figure 3.9: Relative importance of bubbles and temperature on the density as a function of temperature and pressure. The ratio of the density difference due to bubbles and temperature taken on the y axis. Since the curve always lies below 1, it shows that temperature is always important in (a). In the case of pressure, the effect of bubbles dominate below a pressure of 3 bar as seen in (b).

The significance of including the temperature in the model was seen through a Matlab plot where the relative importance of density difference due to temperature and bubbles was observed by me. Figure 3.9 shows how the effect of temperature and void fraction play a role in modifying the density of the electrolyte. Figure 3.9a shows the relative importance of the two factors from 1 bar to 50 bar. The electrolyser is meant to be operated at 50 bar and at this pressure, the effect of temperature dominates and as the pressure decreases, the effect of void fraction becomes more relevant. In Figure 3.9b, the effect of temperature is seen on the relative importance of the two factors. The effect of the temperature on the density is far more pronounced than the effect of bubbles on the density of the electrolyte. This makes it more important to include the effect of temperature in the Matlab model.

Some modifications were done so as to account for the effects of the temperature. The two factors affecting the temperature are advection and diffusion. The modifications to the Matlab model were added in steps and the variation in the resulting velocity values were tabulated in table 3.3.

1. **Boussinesq approximation**: Boussinesq approximation was added to account for the variation in the density of the electrolyte with the temperature. The effect of adding temperature to the model is seen in the other two cases and hence, the Boussinesq approximation was added but not used in this case. Also, iterative solving was added to the model with the mass flow convergence being the condition.

2. **Effect of conduction on convection**: The effect of conduction on the temperature of the system is already analysed using Adobe Fusion 360. The zero flow case in the Adobe Fusion 360 model provides the required information for the pure conduction case. Based on this, the temperature driven flow is obtained. This is a case where the conduction and convection are decoupled and the effect of conduction on convection is seen. No iterations were used in this case as the temperature values are well defined for each cell.

3. **Convection and looping**: For the case of convection, the Matlab model [18] was used. The total heat supplied to the system is calculated in equation 3.17 and the mass flow rate is obtained from the case of flow driven by bubbles. The resulting temperature difference is calculated using equation 3.18.

$$\dot{Q}_{\text{sup}} = (V_{\text{sup}} - V_{\text{tn}})\, I_{\text{sup}} \tag{3.17}$$

$$\dot{Q}_{\text{sup}} = \dot{m}_{\text{tot}} \times c_{\text{p,l}} \times \text{dT} \tag{3.18}$$

$$T_{\text{top}} = T_{\text{bot}} + \text{dT} \qquad T_{\text{cell}} = \frac{T_{\text{bot}} + T_{\text{top}}}{2} \tag{3.19}$$

Here, T_{top} is the temperature of the electrolyte at the exit of the cell, T_{bot} is the temperature of the electrolyte before it enters the cell, T_{cell} is the temperature of the electrolyte inside the cell, dT is the temperature difference between the top and bottom of the cell, $\dot{Q}_{\text{sup}}$ is the heat supplied to the cell, V_{sup} is the supplied voltage, V_{tn} is the thermo-neutral voltage, I_{sup} is the supplied current . The temperature values are updated in all the elements and the mass flow rates are calculated again. This iteration continues until the mass flow rate values converge.

Table 3.3: Comparison of the cases on the Matab model

Parameter	Base case	Case 1	Case 2	Case 3	Units
m_{l}	6.55E-05	6.55E-05	8.32E-05	8.19E-05	kg/s
v_{cell}	1.58E-04	1.58E-04	2.45E-04	2.08E-04	m/s
v_{dc}	3.02E-04	3.02E-04	4.49E-04	3.90E-04	m/s
v_{botch}	6.52E-02	6.52E-02	9.93E-02	8.40E-02	m/s
v_{topch}	7.59E-03	7.59E-03	1.14E-02	9.95E-03	m/s

The base case results are the model used as such without any modifications done. The effect of adding the iterations were shown in case 1. The difference in mass flow rate or velocity are not seen as the temperature is not added yet and the flow velocity obtained from the model is already through iterations in the individual module (oxygen and hydrogen flow calculation module).

For case 2, the mass flow rate improvement is seen because the temperature difference simulates the effect of change in density due to temperature. As in the case of convection (case 3), the temperature difference

causes the flow to improve but the flow is lesser than that of the conduction case because the temperature difference between the downcomer and the cell is lesser (5 K) in case 3 than that of case 2 (11 K). Although the inclusion of the effect of the temperature is not as robust as including a third network for estimating the temperature, this gives an idea about the influence of temperature on the model.

3.4. Modelling

Two applications, namely, Matlab and Comsol Multiphysics were used by me for the prediction of temperature and flow values in the alkaline electrolysis cell during operation. The various parameters chosen for the analysis are presented in this section.

3.4.1. Matlab modelling

The general matlab model for the alkaline electrolyser [18] was modified to predict the electrical and hydrodynamic characteristics of the setup. The general parameters were the same as that of the main setup like the angle of the flow channels and the diameter of the channels. But the down-comer and flash tank channel width are made equal on both the sides in the setup instead of different sizes as in the case of the actual setup. This was done so that the polarity of the electric current can be switched and the flow in the inner half cell can be visualised on the outer half cell. If the downcomer and flash tank were not same on both the half cells, they will also play a role if any difference in the flow is noticed. The method of estimating the parameters has already been explained in the previous section.

3.4.2. Comsol Modelling

To see the combined effects of flow and temperature and to get a visual plot of the same, a multiphysics simulation was done using Comsol Multiphysics. The model was split into various bodies so that it becomes easier to quantify the flow velocity from the results at a later stage.

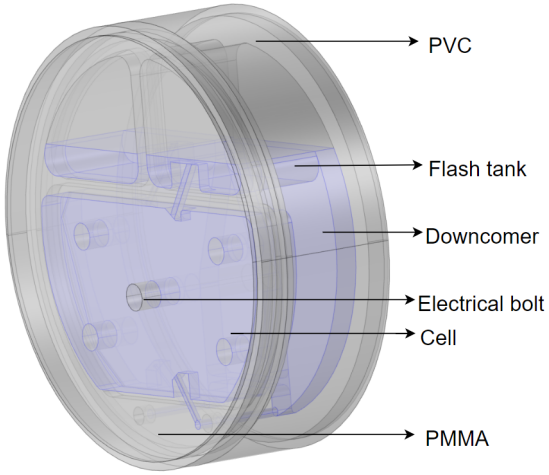

Figure 3.10: Various parts of the 3D model used in the analysis. The part of the image coloured in blue is the part of the system which has the electrolyte.

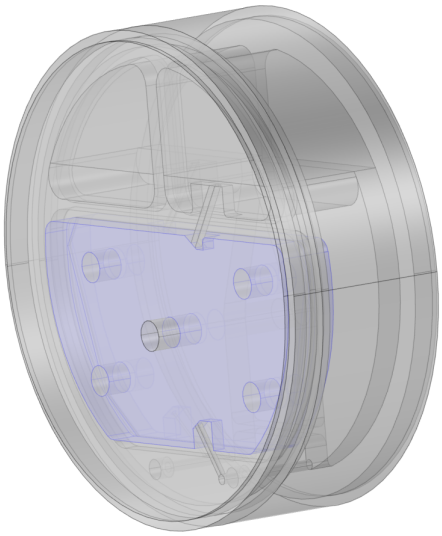

Figure 3.11: Part of the system where the body force is applied

The heat input to the system was from the faces of the electrode and the value of the heat input was calculated based on the voltage and current that is supplied to the system. For alkaline water electrolysis, the thermoneutral voltage (V_{tn}) is 1.48 V and assuming supplied voltage (V) as 2 V, the heat input to the system is,

$$Q = (V - V_{tn}) \times I = (2 - 1.48) \times 10 = 5.2\text{W} \tag{3.20}$$

The heat generated due to that is spread across both the electrodes. Initially, the simpler model has one half of the cell with the bottom channel, channel to the cell, channel from the cell and the down-comer. The flow is natural convection and the main driving force for the flow is the formation of bubbles at the cell which decreases the effective density of the fluid in the cell. This buoyancy driven flow is simulated using a volume

body force. The laminar flow module in Comsol is used to obtain the flow parameters. The velocity predicted by Matlab model helped in identifying the flow regime and the Reynolds number was low enough for the flow to be considered as laminar flow. As seen in Figure A.9, the velocity at various sections of the electrolyser was used to calculate the Reynolds number. Using this value, the order of Reynolds number was estimated by,

$$Re = \frac{\rho_l \times v_l \times d_{\text{flow}}}{\mu_l} \tag{3.21}$$

Table 3.4: Predicted Reynolds and Péclet number at various locations of the test setup

Location	$\mathbf{d}_{\text{flow}}$ **(m)**	$\mathbf{v}_l$**(m/s)**	**Re**	**Pe**
Down-comer	0.0117	1.27E-04	1.91	33
Bottom channel	0.0020	4.30E-03	11.08	403
Channel to cell	0.0010	1.72E-02	22.15	1236
Cell	0.0093	2.01E-04	2.41	52
Channel from cell	0.0015	7.85E-03	15.17	689
Flash tank	0.0102	1.66E-04	2.18	21

The value of Reynolds number and Péclet number at various locations is presented in Table 3.4. As it can be seen in Table 3.4, the value of Reynolds number is less than the transition Reynolds number of 2300. Hence, the assumption of laminar flow is valid. Since the Péclet number is larger than 1, heat transfer through advection is greater than the flow through diffusion. The effect of gravity is included with the flow being set to incompressible. In addition to the 'Laminar flow' module, the 'Heat transfer in fluids' module was used to see the temperature distribution during the flow. In the heat transfer module, a boundary heat source was added where the electrode area is exposed to the fluid and the boundary convection heat flux was described to simulate the heat loss to the walls of the test setup. For the stationary solution case, the following equations were used by Comsol to iteratively solve the given problem:

$$\rho(\mathbf{u}\cdot\nabla)\mathbf{u} = \nabla\cdot[-p\mathbf{I} + \mu(\nabla\mathbf{u} + (\nabla\mathbf{u})^T)] + \mathbf{F}_b + \rho\mathbf{g} \tag{3.22}$$

$$\rho\nabla\cdot(\mathbf{u}) = 0 \tag{3.23}$$

$$\rho c_p \mathbf{u}\cdot\nabla T + \nabla\cdot\mathbf{q} = Q + Q_p + Q_{vd} \tag{3.24}$$

Equations 3.22 and 3.23 are the momentum and mass conservation equations used to solve for the flow part of the problem. Equation 3.24 is used to solve for the heat part of the problem. In equation 3.22, F_b is the body force given in terms of the void fraction at the cell.

$$F_b = \alpha \times \rho_l \times g \tag{3.25}$$

where α is the void fraction. The non isothermal flow module was used from the multiphysics menu of Comsol to couple the effects of heat and flow to each other. In the module, there is an option to vary the density of the fluid with the temperature using Boussinesq approximation. This assumes that the density of fluid in the system is a linear function of the temperature. The incompressible flow option was chosen initially to account for the variation in the density only in the body force term using this approximation.

The grid independence study was done and the results are provided in Appendix A. The mesh used for the analysis was a compromise between accuracy and computation time. Figure 3.12 shows the mesh used for the analysis. Using a reference temperature, the density and the thermal coefficient of expansion, the density values can be calculated for other temperature values. This assumption is valid as long as the temperature variation is not too high. Equation 3.26 shows the equation form of the effective density of the fluid.

$$\rho_l = \rho_{\text{ref}}[1 - \beta(T - T_{\text{ref}})] \tag{3.26}$$

Time dependent simulations were run on the model for obtaining the heating curve of the electrolyser. This will give an expected estimate for the temperature of the system after a particular duration. The level of insulation required was estimated from Comsol by running the simulations for different values of $h_{c,\text{air}}$ (convective heat transfer coefficient of air). The comparison is done for the temperature at the front,top location.

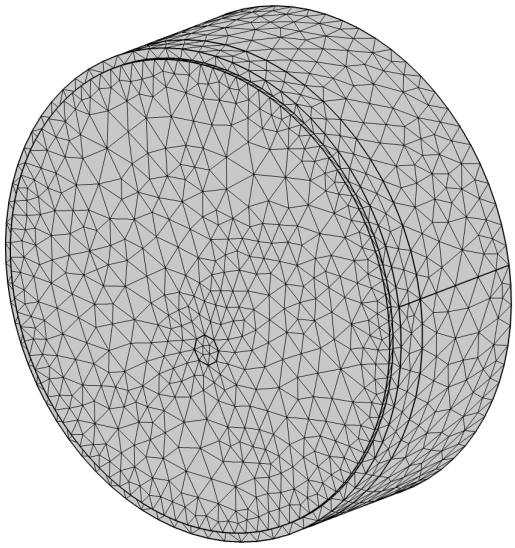

Figure 3.12: Mesh generated by Comsol. The mesh size was based on the in-built options in Comsol. The degree of refinement can be chosen and the level of discretisation was decided by Comsol based on the physics. [9]

The resulting curves are compared with the curve obtained from the experiments to see what value of insulation is effectively present and how much insulation has to be added to increase the temperature of the system. The ambient air temperature was assumed to be at 20°C and the time dependent calculations were done based on the following equations in Comsol:

$$\rho(\mathbf{u}\cdot\nabla)\mathbf{u} = \nabla\cdot[-p\mathbf{I}+\mu(\nabla\mathbf{u}+(\nabla\mathbf{u})^{T})]+\mathbf{F}_{\mathrm{b}}+(\rho-\rho_{\mathrm{ref}})\mathbf{g} \tag{3.27}$$

$$\rho\nabla\cdot(\mathbf{u}) = 0 \tag{3.28}$$

$$\rho c_{\mathrm{p}}\frac{\partial T}{\partial t}+\rho c_{\mathrm{p}}\mathbf{u}\cdot\nabla T+\nabla\cdot\mathbf{q} = Q+Q_{\mathrm{ted}} \tag{3.29}$$

$$\mathbf{q} = -k\nabla T \tag{3.30}$$

3.5. Experiments

The electrolyser has to be characterised with respect to flow and heat. The actual electrolyser of ZEF would be running at a pressure of 50 bar. But the current experiments are run at 1 bar where the characteristics of the flow and heat are different when measured simultaneously. Hence, the heat and fluid characteristics cannot be obtained at the same time. This is because the void fraction in the cell is lower at higher pressure for the same current density and the heat generated in the system is dependent on the current density. The strategy to obtain these characteristics are as follows:

- The thermal characteristics were obtained by running the system at the same current density and atmospheric pressure
- The flow characteristics were obtained by running the system at lower current density and atmospheric pressure

Figure 3.13 shows the front and rear views of the actual test setup before the experiments. The location of the temperature sensors are also visible along with the silicone rubber sealing which is pink in colour. The level of KOH is also seen in the flash tank. The rear view shows the two temperature sensors at the back along with the electrical connection bolt. The entrance of the bottom channel is also seen at the bottom to left half of the downcomer.

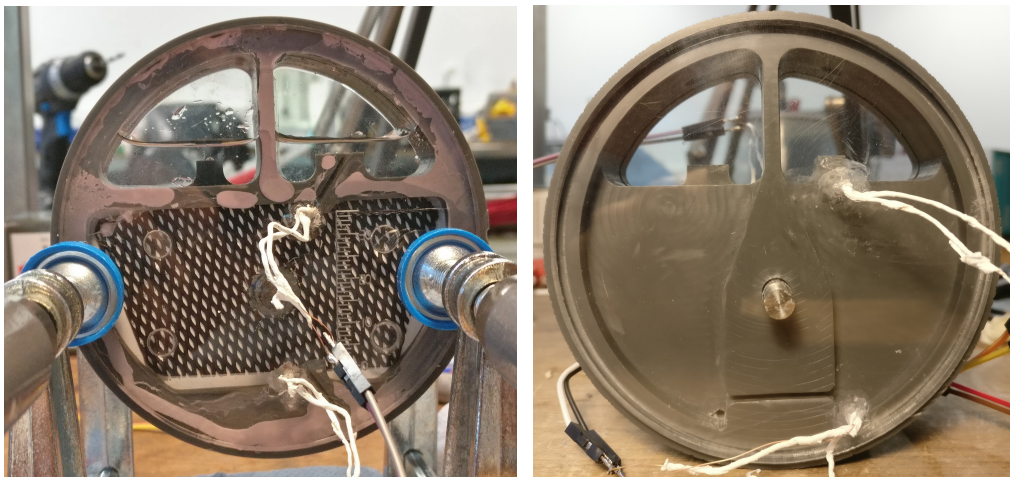

(a) Front view (b) Rear view

Figure 3.13: Front and rear views of the test setup. The image of the front view was taken after the silicone sealing was applied whereas the rear view was taken before the silicone sealing was applied.

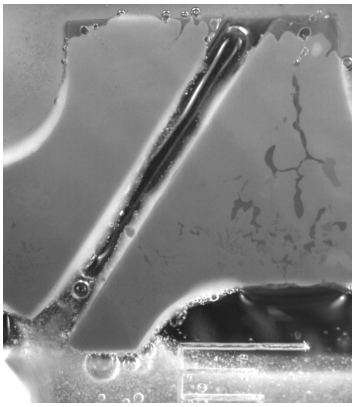

Figure 3.14: The top channel showing a bubble flowing through it to the flash tank. To get a feeling of a scale, the channel is 15 mm in length and the scale below the channel to the right shows 1 mm graduations.

Figure 3.14 shows the top channel (channel from cell) during operation. The bubble formed at the cell is flowing through the channel to the flash tank. Some bubbles are also seen at the flash tank. The bubble diameter is bigger than the channel width and is hence, elongated as it flows through the channel. There is also some KOH leaving the system along with the generated gas bubbles [7]. The flow measurement equipment and the flow measurement technique is presented in Appendix B.

3.6. Thermal characterisation

The thermal characteristics of the test setup was obtained by me, using temperature sensors (NTC). The current density was kept at the same rate as that of the actual electrolyser and it was run at atmospheric pressure. This will give an estimate for the temperature rise in the system. A temperature profile as a function of time can also be obtained for these locations to see how long it takes before the system reaches steady state conditions. The test was run for about 7200 seconds. For this test, Table 3.5 shows the operating conditions:

Table 3.5: Operating parameters for the thermal characterisation

Parameter	Value	Unit
Current	0.3	A/cm^2
Voltage	2.2	V
KOH concentration	30	%
Quantity of KOH	54	ml
Density of KOH	1280	kg/m^3
Pressure	1	bar

3.7. Flow characterisation

The void fraction in the electrolysis cell was calculated using equation 2.25,

$$\alpha_g = \frac{3}{16}\frac{RTjH_{cell}}{PFu_g t} \tag{3.31}$$

As seen in equation 3.31, the void fraction is inversely proportional to the pressure of the system. Hence, to simulate the effect of bubbles at 50 bar in the current setup, the current density has to be decreased by a factor of 50 to offset the atmospheric pressure at operating conditions. At this current density, the thermal characteristics will be different but the hydrodynamics will still be close to 50 bar operating conditions.

The experiments were intended to be conducted at a density of 1280 kg/m^3, but the fluorescent particles were not available for that density. Particle flotation test was done for about an hour and the particles did not stay in the flow with 30% KOH. Hence, the experiments were conducted at a lower density where the percentage of KOH was at 20%.

There were a few parameters based on which the matlab model was developed. To check for the deviation of the model predictions from the actual test setup, the few parameters to be identified with respect to flow characterisation are:

1. Average bubble diameter while leaving the electrode
2. Flow pattern of the electrolyte in the cell
3. Average velocity at some part of the cell

3.8. Design modification

The current design suggests that there is a problem with the flow in the channels. Due to unsteady flow at the top channel, the dynamics of the electrolyte flow are not ideal. Hence, the channel at the top was widened to see if it improves the flow. The depth of the channel cannot be modified as the thickness of the front cookie is about 2 mm at the thinnest point where the channel is present.

Hence, the width of the channel was modified to be twice the value of current design. Figure 3.15 shows the modified version of the front cookie. The top channel was widened to 3 mm and all the flow parameters were obtained for this system for comparison with the original setup design.

There was a significant layer of gas filled at the top of the cell which was not able to get out of the cell as the entrance of the channel was below the top wall of the cell. Figure 3.16 shows the narrow channel with the electrolyte level being at the same height as that of the channel entrance. The gases are trapped in between the electrolyte level and the top wall of the channel as seen to the right of the channel. The channel was also modified such that the opening of the channel is in line with the top of the cell. This would ensure that the electrolyte is in contact with the entire electrode area instead of the gases.

Figure 3.15: Modified front cookie with the top channel having 1.5 mm depth and 3 mm width.

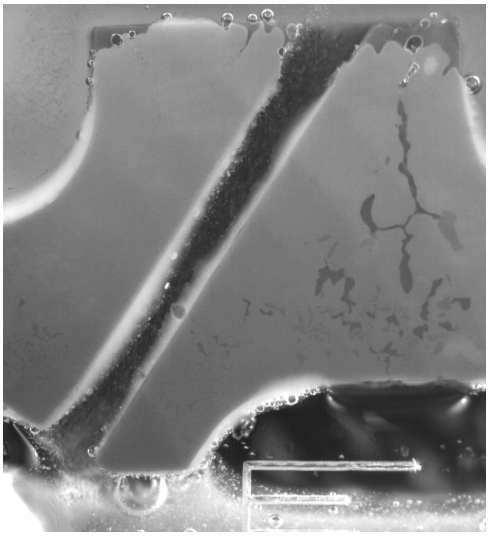

Figure 3.16: Gases trapped in between the top wall of the cell and the electrolyte level.

The flow pattern itself has not changed fundamentally with it showing slug flow in the channel. But the flow has improved where there is greater flow and the bubbles find it easier to travel through a wider channel. Hence, the flow is more continuous than in the previous case. The results of the measurement and the comparison are presented in chapter 4.

3.8.1. Average bubble diameter

Determining the accuracy of the bubble diameter estimation was important as the bubble velocity depends on the bubble diameter and the void fraction in the cell depends on the bubble velocity. The density difference of the electrolyte in the cell and outside the cell due to void fraction is the driving force and hence, accuracy of the bubble diameter is important. The average bubble diameter of the bubbles when leaving the electrode had to be determined to compare with the matlab model. The information was available from the same set of frames used to look into the variation of bubble velocity with respect to diameter.

The main criteria here was that the diameter of the bubble was measured when it left the electrode and moved into the flow. A few bubbles were selected at random and the bubble diameter was measured using the same technique that was used to measure the bubbles in the previous case.

3.8.2. Flow pattern of the electrolyte in the cell

For obtaining the flow pattern of the electrolyte, the fluorescent particles were used. They absorb light from other wavelengths but give out light of a particular wavelength, in this case, orange. The filter was used for the camera to obtain the particles alone and filter out any other wavelength. This was done because the particles were difficult to distinguish from small bubbles if non-fluorescent particles were used. The experiment was done in the dark and all the external light sources were minimised to avoid anything other than the particles in the field of view.

3.8.3. Estimation of flow velocity

The flow at the channel connecting the cell and the flash tank was used for validating the results obtained from Comsol and Matlab. The channel has the gases and the electrolyte flowing through it.

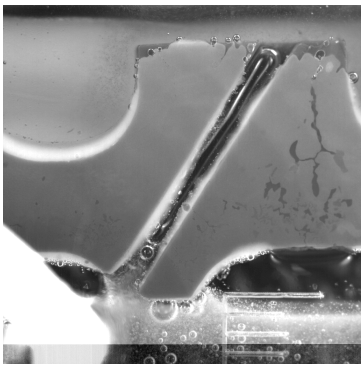

(a) Electrolyte starts filling the channel

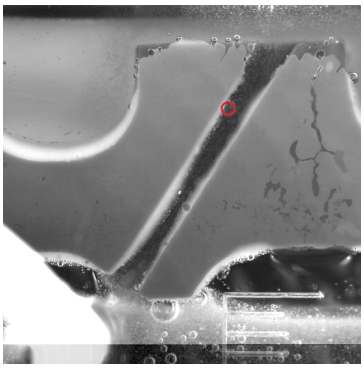

(b) Electrolyte fills the channel with small bubbles

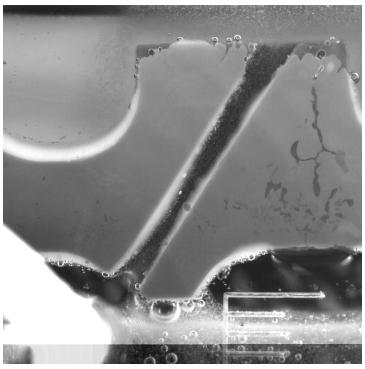

(c) Large gas bubbles start filling the channel

Figure 3.17: Flow in the top channel at different points of time. (a) shows the electrolyte entering the channel, pushing the gas out of the channel and fills the channel as seen in (b). Small bubbles flow through the channel during this time and is marked in red in (b). Large gas bubbles enter the channel again after a while and push the electrolyte out of the channel.

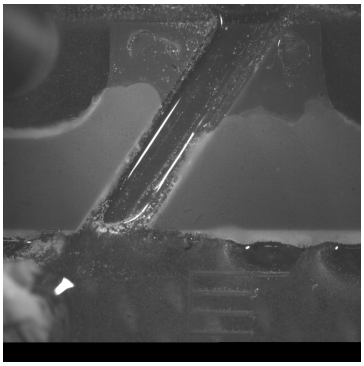

(a) Electrolyte starts filling the channel

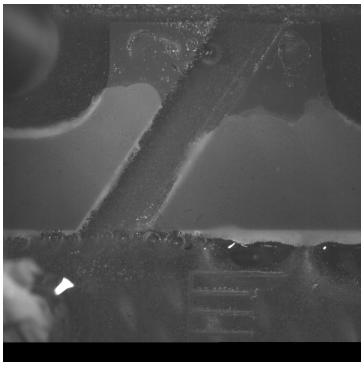

(b) Electrolyte fills the channel with small bubbles

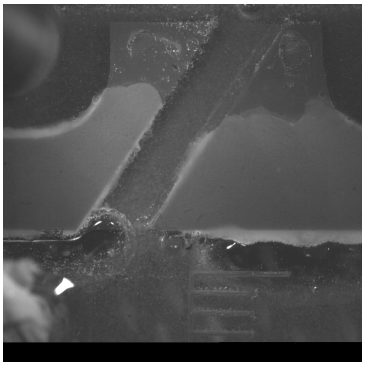

(c) Large gas bubbles start filling the channel

Figure 3.18: Flow in the wide top channel at different points of time. (a) shows the electrolyte entering the channel, pushing the gas out of the channel and fills the channel as seen in (b). Small bubbles flow through the channel during this time which is also seen in (b). Large gas bubbles enter the channel again after a while and push the electrolyte out of the channel.

Figure 3.17 and Figure 3.18 show the flow in the top channel at different points of time. The images are placed such that they show the state of the flow in the channel as the time progresses. The flow in the channel is as follows:

1. Figure 3.17a and Figure 3.18a show the flow in the channel when the electrolyte just begins to enter the channel from the bottom. The flow direction is from bottom to top. The channel is filled with gas in the image. The electrolyte keeps pushing the gas until the channel is mostly filled with electrolyte.

2. Figure 3.17b and Figure 3.18b show the channel when the electrolyte mostly fills the channel. When the electrolyte is flowing through the channel, small bubbles move through the channel. One such bubble is seen in Figure 3.18b and the bubble in Figure 3.17b is not seen clearly. Hence, it is marked in red.

3. Figure 3.17c and Figure 3.18c show the flow in the channel when the large gas bubbles start flowing into the channel again. They push the electrolyte to the flash tank and the gas fills the channel. This part of the flow is similar to the annular flow pattern.

The amount of time taken by bubbles in the channel have to be taken into account while doing the mass flow calculations of the electrolyte in the channel. There are particles in the electrolyte and these particles were used for obtaining the velocity of the electrolyte in the channel. The mass flow rate was obtained with the cross section area of the channel, the flow rate and the density of the electrolyte.

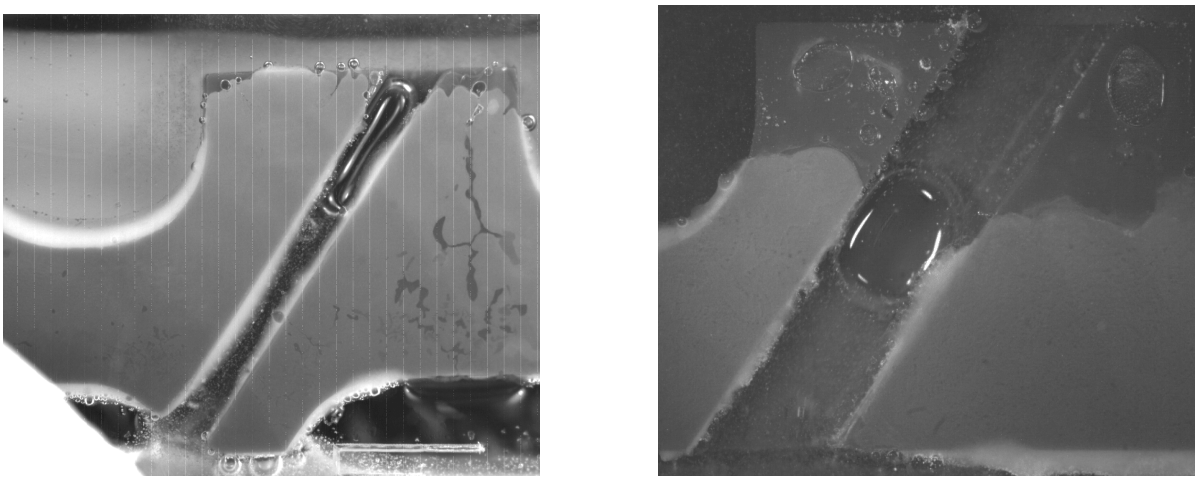

(a) w_{ch} = 1.5 mm (b) w_{ch} = 3 mm

Figure 3.19: Taylor bubbles in the both the channel cases. The length of the gas slug in the narrow channel is longer than the wide channel.

Influence of the capillary inner diameter on the gas slug length in a two phase liquid flow was studied by Laborie et al.[22] and it was found that the gas slug length decreased with the increase in the inner diameter. The same is qualitatively observed in this case.

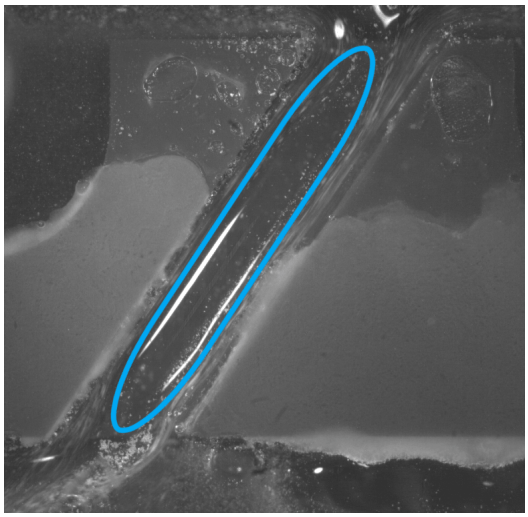

Figure 3.20: Back-flow of the electrolyte into the cell in the wide channel case. The part of the channel occupied by gas is shown in blue around which there is back flow. The flow direction is downwards back into the cell.

The video of the channel flow was used for obtaining information on how long the electrolyte was in the channel and how long the bubbles were in the channel. The video also gave information on how many small bubbles moved through the channel in a time interval. There is also back flow of the electrolyte in the case of the wide channel as shown in Figure 3.20. The flow occurs in between the bubbles and the channel. This electrolyte flow back into the cell has to be subtracted from the obtained mass flow rate to get the actual flow rate in the wide channel case.

4

Results

The flow and the electrical current characteristics were determined by Matlab. The Matlab model was compared to the results from the Comsol simulations. The Comsol simulations produced the thermal and flow characteristics out of which the thermal simulation results were validated in thermal characteristics. Bubble diameters from the experiments were compared to the values predicted by Matlab. The flow results from Comsol and Matlab were compared with the experiments.

4.1. Matlab

The results of the model are shown in Figure 4.1 and Figure 4.2. In Figure 4.1, the blue lines are the part of the setup where the flow is on the hydrogen side and the red lines represent the part the part of the setup where the flow is on the oxygen side. The black horizontal line represents the electricity through the electrodes and separator. The cells are represented as points at 2 V and 0 V. All the vectors have values of leaking current and the power lost as a consequence of it. At every node, the voltage is shown and ideally, all the current should go through the cell. In reality, the leaking currents are present. If the channel at the bottom connecting the down-comer on the hydrogen and oxygen is absent, there is no leaking current in the system. This is because the hydrogen and oxygen become disconnected and everywhere in the individual circuit, the voltage is same. Hence, there is no current flowing.

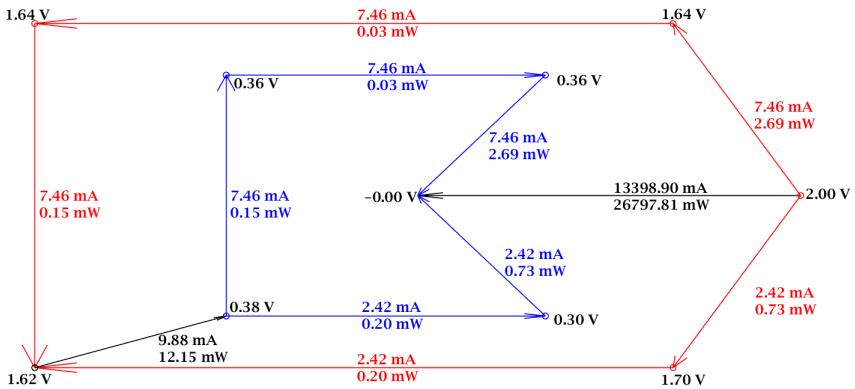

Figure 4.1: Electrical parameters in various parts of the setup. The current through the electrode and the separator is shown on the black horizontal element. The rest of the values are a result of leaking currents. The power loss associated with the leaking currents are also mentioned next to every element. The voltage values are mentioned at

Figure 4.2 shows the results with the hydrogen side, oxygen side and the connecting channel combined. The expected flow is constant in the hydrogen and oxygen circuit due to mass balance. The pressure value at every

node is also shown. The channels in the hydrogen and oxygen side are different and are modelled based on the test setup. In the case of the hydrogen circuit, the electrolyte has to travel for a longer distance at the flash tank and the bottom channel, hence having higher resistance to flow.

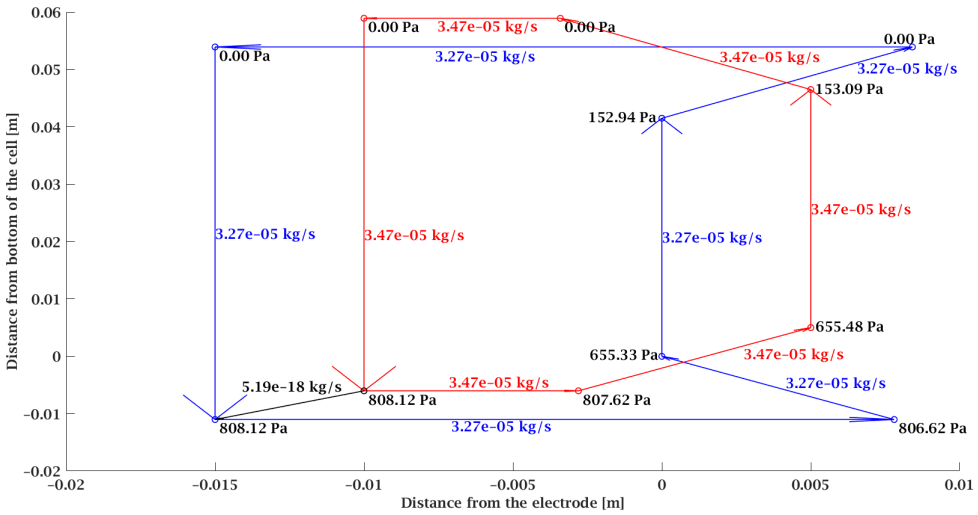

Figure 4.2: Mass flow rate of KOH solution in various parts of the setup. The length of the vector lines scale with the actual length of the corresponding parts of the setup. The oxygen loop is slightly offset to separate it from the hydrogen loop.

Table 4.1 shows the value of leaking current and the mass flow rate of the electrolyte at the top channel for w_{ch} = 1.5 mm and w_{ch} = 3 mm.

Table 4.1: Results of the leaking current and the mass flow rate for both the cases

w_{ch} (mm)	$\dot{m}_l$ (kg/s)	Leaking current (mA)
1.5	3.27E-05	7.46
3	3.42E-05	9.95

4.2. Comsol

The result of the simulation is presented in Figure 4.3 and Figure 4.4. The velocity profile is shown from two angles for showing all the information from the simulation. The profile was obtained along two planes: one along the depth of the electrolyser and the other was sliced along the face of the electrolyser. The upper and the lower limits of the legend are scaled equally so that they are visually comparable. The channel connecting the bottom channel to the cell is missing in the side view as no part of the channel lies on the slice plane. In Figure 4.3a and Figure 4.3b, the left side of the image shows the two half cells and the right side shows the down-comer. The flow is in clockwise direction. The velocity in both the channels is seen in Figure 4.3c and Figure 4.3d along with the cell and the flash tanks. The velocity is lower in the channel at the top in Figure 4.3d, but the mass flow rate is higher than the corresponding channel in Figure 4.3c. There are five holes in the cell part of the front view, four of which correspond to the PMMA bolts and one corresponds to the electrical bolt.

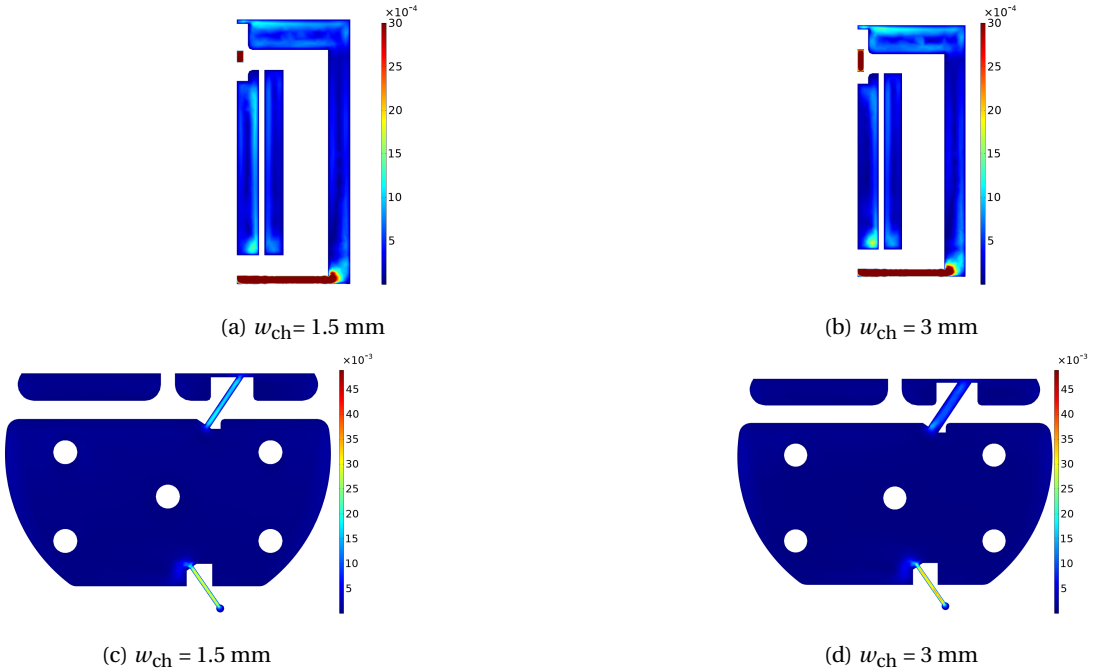

(a) w_{ch}= 1.5 mm (b) w_{ch} = 3 mm

(c) w_{ch} = 1.5 mm (d) w_{ch} = 3 mm

Figure 4.3: Velocity profile in the electrolyser from two angles, depth view and the front view. (a) and (b) show the velocity profile on a plane cut through the depth of the electrolyser. The left side of the images is the cell and the right side is the down-comer side. (c) and (d) show the velocity profile on a plane cut parallel to the face of the electrolyser. The cell, the flash tank and the two channels are visible in this view.

(a) w_{ch} = 1.5 mm (b) w_{ch} = 3 mm

Figure 4.4: Temperature profile on a plane that is cut through the depth of the electrolyser. The temperature is highest at the electrode and the heat is transferred to the electrolyte. The cooling happens at the downcomer.

Figure 4.4 shows the temperature profile on the plane cut through the depth of the electrolyser for both the cases. The highest temperature is observed at the electrode and the cooling occurs at the down-comer. The temperature of the electrolyte heats as it moves from the bottom to the top which is also expected. The view is same as that of the Figure 4.3a and Figure 4.3b for better understanding. The Comsol model can be further improved by using the 'Bubbly flow module' to include multi-phase flow in the system.

Table 4.2: Comparison of the flow results from Matlab and Comsol

Location	Matlab		Comsol		Error	
	$\dot{m}_l$ (kg/s)	v_l (m/s)	$\dot{m}_l$ (kg/s)	v_l (m/s)	$\dot{m}_l$ (%)	v_l (%)
Cell	3.3E-05	7.8E-05	2.6E-05	5.0E-05	20.7	55.2
Channel from cell	3.3E-05	1.2E-02	2.4E-05	8.3E-03	27.2	42.8
Flash tank	3.3E-05	1.3E-04	2.4E-05	8.1E-05	26.1	58.8
Down-comer	3.3E-05	1.5E-04	2.4E-05	1.4E-04	25.4	6.4
Bottom channel	3.3E-05	8.2E-03	2.4E-05	7.4E-03	25.3	11.5
Channel to cell	3.3E-05	3.3E-02	2.4E-05	1.9E-02	26.3	74.1

Comparing the results from both the Matlab and the Comsol model, the values are tabulated in Table 4.2. The values of velocity and the mass flow rate are displayed in the table. The mass flow rate in the Comsol model is calculated using the formula,

$$\dot{m}_l = \rho_l \times A_{\text{flow}} \times v_l \tag{4.1}$$

The value for the density of KOH is taken as 1280 kg/m^3. The values of the mass flow rate for the matlab model are larger than the values obtained in Comsol. This can be due to the following reasons:

- Approximation of the model in Matlab and not considering the exact geometry
- Ignoring friction in the bends which can reduce the flow rate predicted by Matlab
- Not including the electrical analogy network for temperature

With these issues included, the prediction of Matlab is not far from what a multiphysics simulation software predicts. The highest error percentage for the mass flow rate is 27%. This makes the Matlab model reliable enough for the estimation of flow parameters. Improving the model by including the temperature model and friction factors for bends and curves can bring the results of the Matlab model closer to the Comsol model.

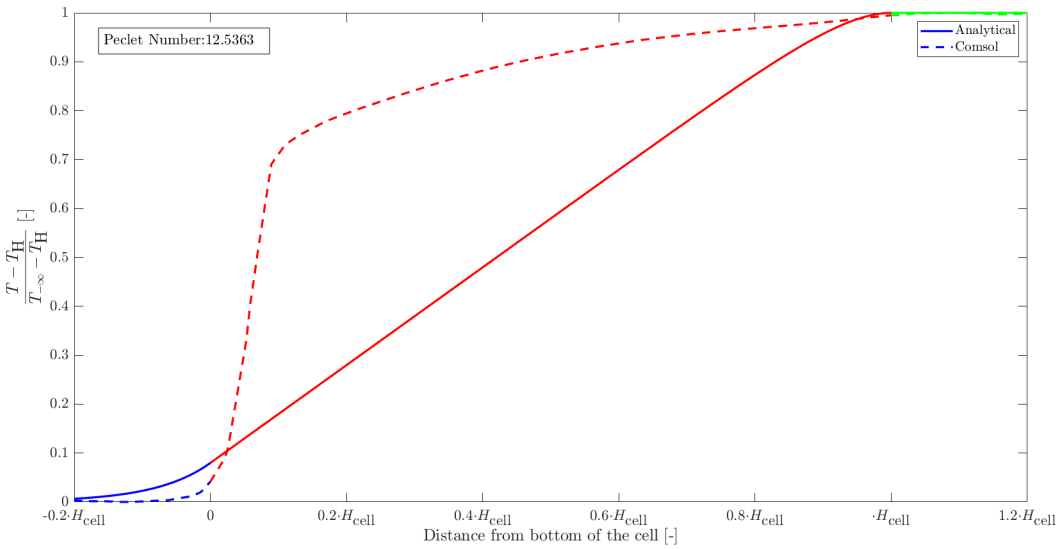

Figure 4.5: Comparison of temperature profiles from simulation and analytical solution for same parameters. H_{cell} in the x axis is the y-coordinate of the cell height (4.15 cm). The shape of the curve at the cell is different at different depth levels in the cell. The assumption of constant temperature for the flow after the cell in the analytical model is also seen in the simulations.

The temperature profile was obtained from Comsol along the vertical axis and was plotted along with the analytical result obtained in section 3.1. Figure 4.5 shows the comparison of temperature profiles for the same parameters in the Comsol and the analytical solution like velocity of the electrolyte. The assumption of a flat temperature curve beyond the height of the cell was validated by Comsol simulations. The temperature curve at the cell was not the same curve as the one in the analytical solution. The shape of the temperature

curve depends on the depth at which the curve is obtained. The shape of the curve becomes closer to ideal as we get closer to the electrode. The figure containing the temperature profiles at different depth is present in Appendix A. Also, the temperature curve is obtained along an angled line at the cell as the entrance of the top channel and the exit of the channel at the bottom are not at the same line. The temperature curve along a vertical line gives a different temperature profile.

4.3. Experiments - Thermal characterisation

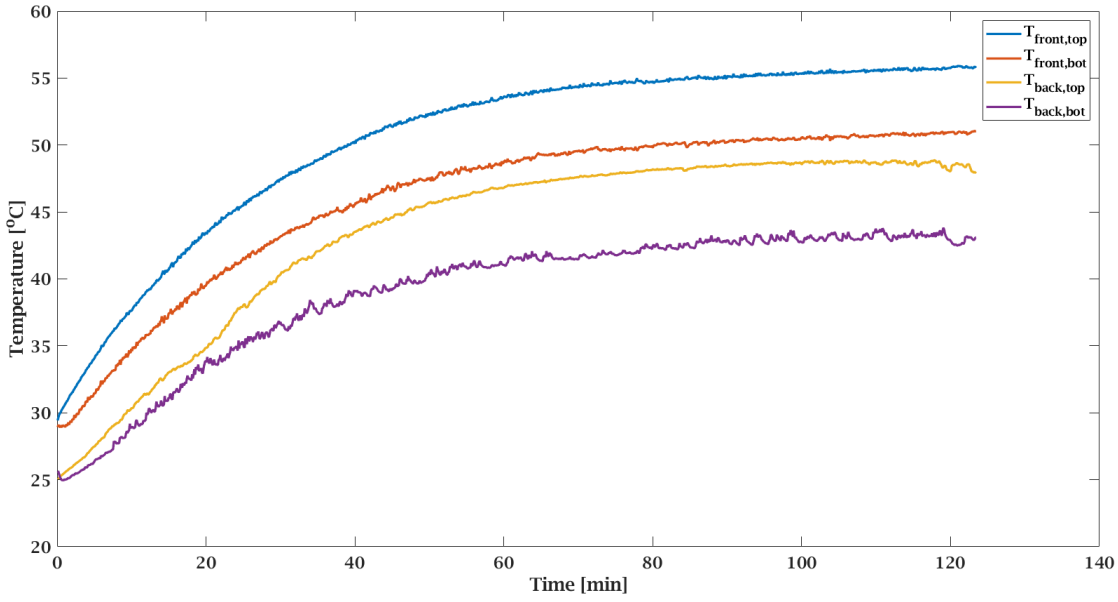

Figure 4.6: Temperature change and the heating curve with respect to time for 10 A of current. The temperature at the front denotes the temperature measured at the cell side and the back side is the down-comer side. The system did not reach steady state at the end of the experiment. Curve fitting was done to find the steady state temperature.

Figure 4.6 shows the temperature profiles over a period of time at different locations in the electrolyser. The temperature rise is seen but it gradually flattens over time. The temperature values begin to follow the expected trend until the end. Steady state condition was not reached even after the experiment. A curve fit was done to obtain the equation for these curves and obtain the steady state temperature. The curve used to fit the equation is of the form,

$$y = (\mathrm{a} - \mathrm{c}) \cdot e^{-\mathrm{b} \cdot x} + c \tag{4.2}$$

Comparing this with Equation 2.41, c is the steady state temperature at the given point (T_∞), y is the temperature at time t ($T(t)$), a is the initial temperature (T_0) and b is the constant (k). The parameters obtained for fitting the four curves is given in Table 4.3

Table 4.3: Parameters of curve fitting the heating curves of the electrolyser with Equation 4.2

Parameter	T_{fronttop}	T_{frontbot}	T_{backtop}	T_{backbot}
a	29.35	27.68	22.84	23.29
b	0.038	0.036	0.035	0.035
c	56.07	51.27	49.59	43.63

Table 4.3 shows the values of the parameters as a result of curve fitting the temperature profiles at four different location in the electrolyser: two at the front where the flow is visible and two at the back which is the down-comer. The goodness of fit for these curves is presented in Appendix B. The value of c gives the steady state temperature at the four locations. The maximum temperature of the system was expected to be at the temperature sensor marked by T_{fronttop} and the steady state temperature is 56°C. This is a lower temperature

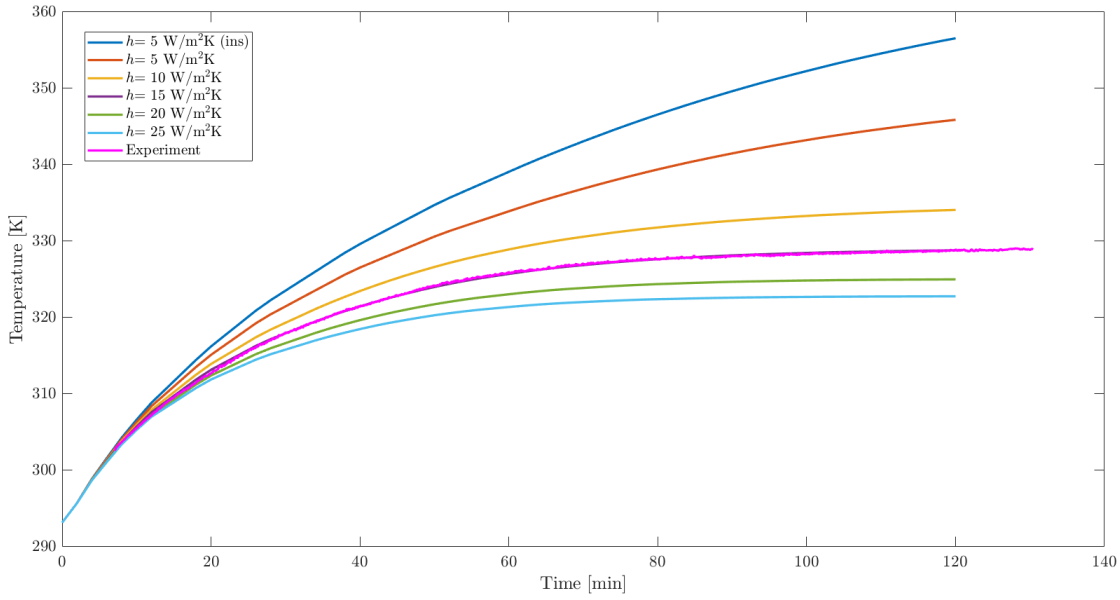

Figure 4.7: Heating curves obtained from Comsol for different values of $h_{c,air}$ along with the heating curve from the experiments. The curve obtained from experiments are comparable to the curve obtained for h = 15 W/m^{2}K in Comsol. The result of the simulation is shown as h = For the system to reach 90°C, insulation is necessary.

than the expected operation temperature of 90°C. This implies a higher heat loss to the environment than expected.

Time dependent simulations were done on Comsol to find the equivalent external heat transfer coefficient value by comparing the results from the experiments. The data from the temperature sensor at the front top was used for the comparison of data from both the Comsol simulations and the experiments. The temperature of the system during experiments did not begin at room temperature. So, the curve obtained through the experiments were offset along the x-axis to find the right curve with respect to the Comsol simulations. Figure 4.7 shows the curves for different values of external transfer coefficient of air. $h_{c,air}$ was varied in the range of typical values of free convection heat transfer coefficient of air [20]. The simulation was run for 120 minutes and the curves were fit using Equation 4.2. The value of $h_{c,air}$ = 15 W/m^{2}K was the curve that matched the curve obtained from experiments. The steady state values of the experiment (56.07°C) and Comsol (55.98 °C) are close enough to validate the Comsol value to be considered.

The curve fit for the Comsol curves are tabulated in Table 4.4. The temperature of the system would be at 56°C with the current configuration and if the operating temperature of the electrolyser has to reach 90°C, insulation is required. With the lowest value of $h_{c,air}$ (5 W/m^{2}K), the system would attain a temperature of 76°C. The front side of the electrolyser alone was insulated with a $h_{c,air}$ assigned a value of 1 W/m^{2}K. With this insulation in the Comsol model, the temperature went to 92°C which is close to the operating point of the electrolyser.

Table 4.4: Results of fitting a curve to the results obtained from Comsol

$h_{c,air}$ (W/m^{2}K)	a (°C)	b (s^{-1})	c (°C)
5 (ins)	22	0.01628	91.86
5	21.85	0.02185	76.01
10	20.82	0.03269	61.64
15	20.57	0.03913	55.98
20	20.44	0.04469	52.04
25	20.36	0.04856	49.78

4.4. Experiments - Flow characterisation

4.4.1. Average bubble diameter

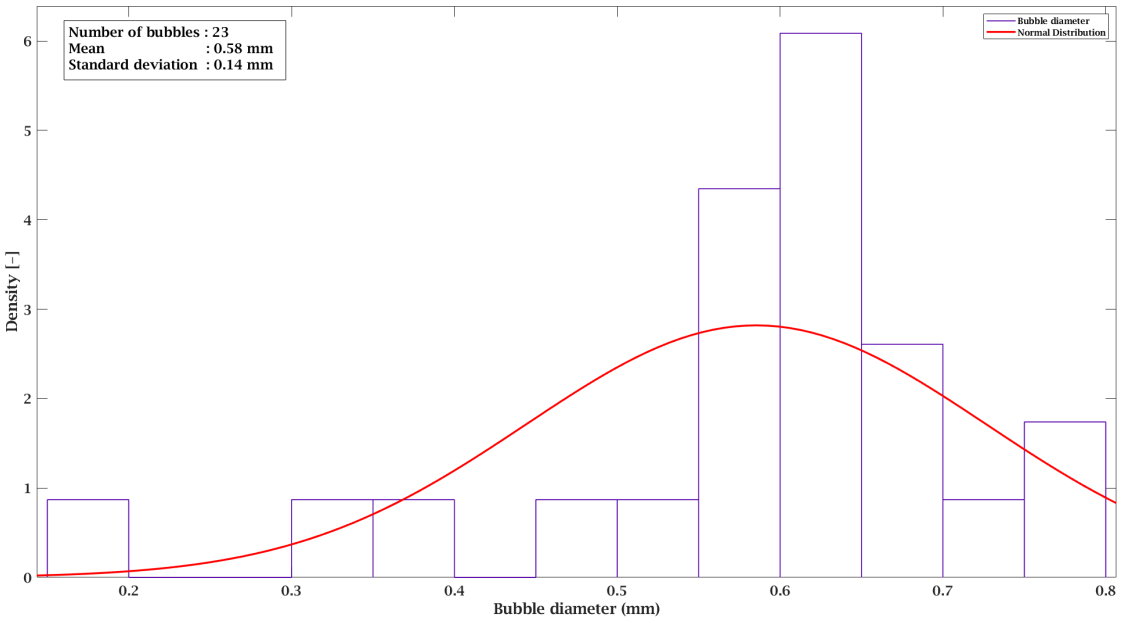

Figure 4.8: Bubble size distribution for the narrow channel (w_{ch} = 1.5 mm) case. The bubble diameter was measured when the bubbles depart from the electrode. The mean diameter of the bubbles is 0.58 mm. The value on the y-axis is the density function of the normal distribution.

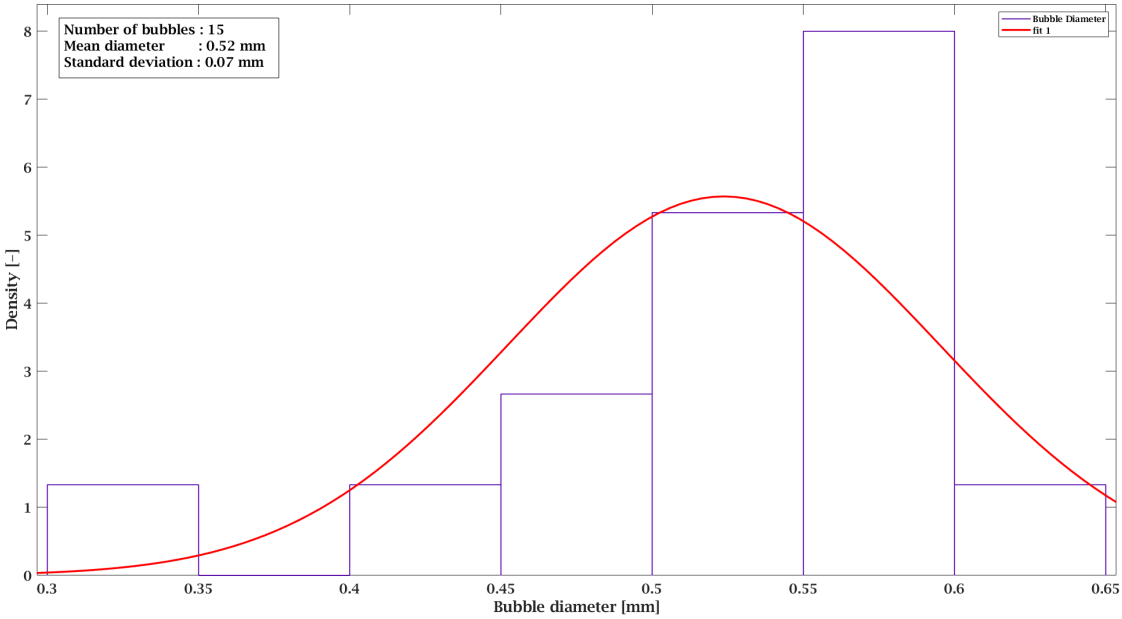

Figure 4.9: Representation of the bubble diameter distribution for the wide channel (w_{ch} = 3 mm) case. The red curve fit is the normal distribution fit for the diameter data. The mean diameter obtained is 0.52 mm which is lesser than the narrow channel case. The value on the y-axis is the density function of the normal distribution.

Figure 4.9 shows the bubble diameter distribution for the wide channel case. The data consists of 15 bubbles whose diameter were measured when they just depart from the electrode. When a normal distribution was fit for the data, the mean was obtained to be 0.52 mm and the standard deviation was obtained as 0.07 mm.

Comparing this to the data from Figure 4.8, the bubble diameter is smaller for the same current across the electrodes. This indicates that the bubbles depart earlier from the electrode in the wide channel case. This can be attributed to the higher velocity of the electrolyte in the cell which result in a higher drag force on the bubbles. The drag force is proportional to the flow velocity of the electrolyte in the cell. This indicates that the hydrodynamics of the electrolyte have improved in the current design.

Table 4.5: Comparison of bubble diameter values obtained from the experiments and the Matlab model

w_{ch} (mm)	**Bubble diameter (mm)**			**Difference (%)**	
	Experiments	**Matlab**	**Modified Matlab**	**Matlab**	**Modified Matlab**
1.5	0.58	0.874	0.797	33	27
3	0.52	0.873	0.796	40	34

Table 4.5 shows the bubble diameter predicted by Matlab and the actual diameter observed in the experiments. The bubble diameter in the Matlab model is larger than the average value obtained from the experiments. The bubble diameter was estimated by the Matlab model using Equation 4.4 [18].

$$d_{0,g} = 1.2\phi\sqrt{\frac{\sigma_l}{g\delta\rho_l}} \tag{4.3}$$

$$d_g = D_{0,g}(1+0.2j)^{-0.45} \tag{4.4}$$

where d_g is the bubble diameter at the given current density, $\delta\rho_l$ is the difference between the density of the electrolyte and the gas bubbles, ϕ is the angle of contact of the bubbles, and $d_{0,g}$ is the diameter of the bubble without considering the effect of current density. The difference in the value estimated by Matlab and that obtained from experiments can be attributed to the variation in parameters considered in the Matlab model. The surface tension was considered to be 0.096 N/m whereas at 18°C, for 20% KOH, the surface tension is 0.08 N/m [29]. With this value, the diameter was calculated and presented in the Modified Matlab column of Table 4.5. It can be seen that the error in prediction is lesser in this case. The scaling of contact angle with the bubble diameter was taken into account with the effect of current density on the bubble diameter. The current density affects the electrode potential which affects the wettability and hence, the contact angle [37]. The bubble diameter also scales differently in the case of the experiments and the Matlab model. Including the effect of velocity of the electrolyte on the bubble diameter can bring the scaling of bubble diameter with the channel width closer to each other.

4.4.2. Flow pattern of the electrolyte in the cell

Figure 4.10 shows the trajectories of a few fluorescent particles that were tracked. It can be seen that all the particles are not moving vertically. Some particles show diagonal motion whereas some move horizontally. This shows that the current design does not have the flow pattern that is expected or ideal. The ideal flow pattern would be to have a flow that moves vertically. The simulations on Comsol and Matlab work under the assumption that the flow is vertical. But in the actual setup, it is seen that the flow is not steady. The flow at the top channel is restricting the flow and the flow that moves upwards does not directly exit the cell through the channel. The flow rises to the top and waits to leave the cell when the bubbles or the fluid which was already at the top is moving out. This leads to flow recirculating within the cell itself for a brief period. Hence, the results obtained from the cell were not used to validate the model. The flow at the top channel is more likely to validate the results from the simulations. The channels were analysed by me to validate the models. Figure 4.11 shows the path taken by various particles as they move through the flow and reach the top. It can be seen that most of the particles are rising in the flow and the trajectory is close to vertical. The ideal case would be when the particles are always moving upwards. This is closer to the ideal case but the rest of the cell does not have the same motion. This also shows that the flow is closer to vertical and hence, there is greater drag force. This also validates why the bubble diameter departing from the electrode in the wider channel case is smaller than the bubble departing in the normal channel case.

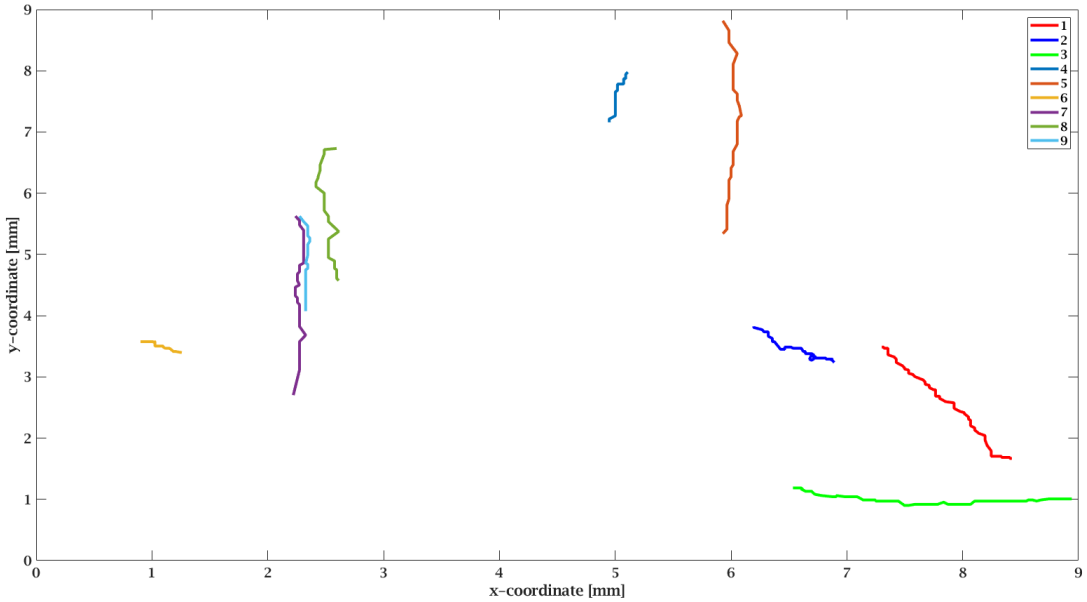

Figure 4.10: Trajectory of various fluorescent particles in the electrolysis cell for the narrow channel case. The trajectories are not always vertical. Some of the particles were observed to be moving horizontally.

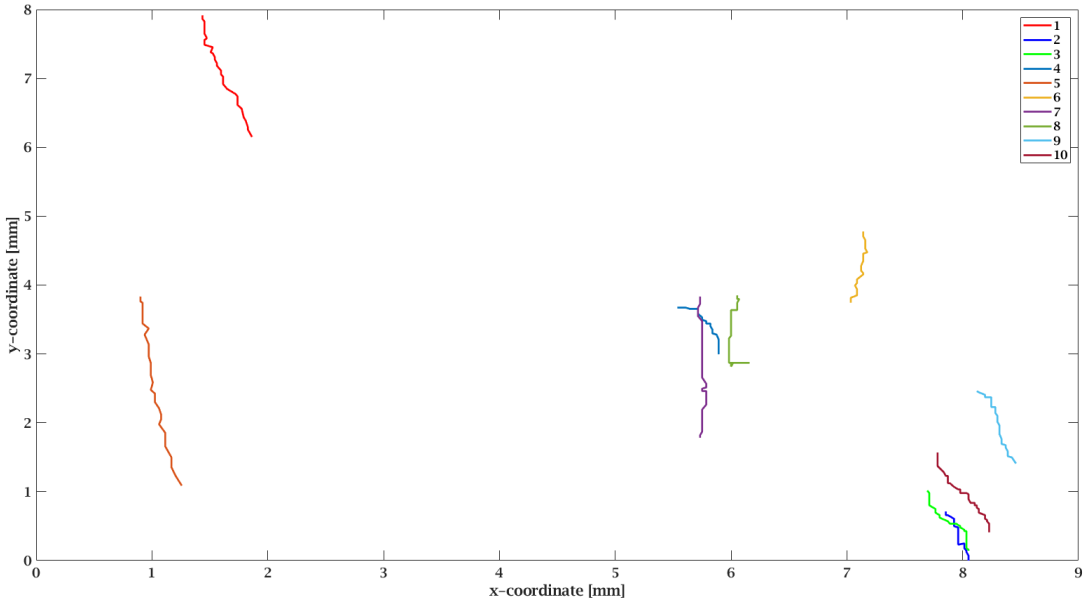

Figure 4.11: Particle trajectories in the wide channel case. The path followed by the particles is more uniform and consistent. Most of the particles are seen to rise up which is closer to the ideal case of the electrolyser compared to the narrow channel case.

4.4.3. Estimation of flow velocity in the channel

Table 4.6: Parameters and results of the narrow channel mass flow rate estimation

Element in the channel	**Number of frames**	**Velocity (mm/s)**	**Cross section area (mm^2)**	**Mass flow rate (kg/s)**	**Total mass flow (kg)**	**Duration (s)**
Electrolyte	649	9.47	2.25	2.65E-05	1.4E-04	5.2
Gases	839	-	-	-	-	6.7
				Total	1.4E-04	11.9

Table 4.6 shows the values of the parameters used for calculating the average mass flow rate in the narrow channel case. The number of frames for which the electrolyte or the gas was in the channel was used to estimate the duration of the flow as the video was shot at 125 fps. The velocity was estimated by particle tracking. Using Equation 4.5, the mass flow rate of the electrolyte was calculated.

$$\dot{m}_{\mathrm{l}} = \rho_{\mathrm{l}} \times A_{\mathrm{ch}} \times u_{\mathrm{l}} \tag{4.5}$$

Since the mass flow rate of the electrolyte was to be estimated, the mass flow rate of electrolyte during the gas flow was assumed to be zero. The total mass flow was then divided by the total duration of the gas and electrolyte flow combined.

Table 4.7: Parameters and results of the wide channel mass flow rate estimation

Element in the channel	**Number of frames**	**Velocity (mm/s)**	**Cross section area (mm^2)**	**Mass flow rate (kg/s)**	**Total mass flow (kg)**	**Duration (s)**
Electrolyte	900	11.8	4.50	6.8E-05	4.9E-04	7.2
Gases	118	-	-	-	-	0.9
Back flow	87	136	2.75	4.7E-04	3.3E-04	0.7
				Total	1.58E-04	8.8

Table 4.7 shows the parameters used for the calculation of average mass flow rate of the electrolyte in the wide channel. The calculation method is similar as in the case of narrow channel. The only change in this case is that the channel has a reverse flow of the electrolyte through the channel to the cell. The mass flow of the back flow must be subtracted from the total flow to get the net flow out of the electrolyte from the cell to the flash tank. The cross section area of the back flow was obtained by considering a circular cross section for the gas trapped in the middle and subtracting it from the rectangular cross section area of the channel.

The value of the mass flow rate can be more accurate if the small bubbles flowing through the channel are accounted for in the calculations. A part of the video was taken when the flow is mostly the electrolyte and the total number of bubbles were obtained. The average volume occupied by these bubbles are calculated and the total mass flow lost as a result of the volume was calculated.

Table 4.8: Comparison of the electrolyte mass flow rate in both channel cases when the bubble volume is included and excluded

$\dot{m}_{\mathrm{l,avg}}$	w_{ch} = 1.5 mm	w_{ch} = 3 mm
Excluding bubbles	1.16E-05	1.79E-05
Including bubbles	1.10E-05	1.49E-05
Difference	5%	17%

Table 4.8 shows the change in mass flow rate of the electrolyte as a result of including the volume of small bubbles. The value of the mass flow rate when the bubbles were excluded was the value obtained from dividing mass flow with the total duration in Table 4.6 and Table 4.7. The decrease in the electrolyte mass flow rate when the bubble volume was included was significant and hence, the mass flow rate of the electrolyte to be considered further would be the one with the inclusion of bubbles.

4.5. Comparison of the models and the experiment

Table 4.9: Comparison of the mass flow rates obtained from Comsol, Matlab and experiments

w_{ch} (mm)	$\dot{m}_l$ (kg/s)			Deviation from Matlab (%)	
	Experiments	Comsol	Matlab	Experiments	Comsol
1.5	1.10E-05	2.44E-05	3.27E-05	66	25
3	1.49E-05	2.81E-05	3.42E-05	56	18

Table 4.9 shows the comparison of the mass flow rates obtained from all the three cases for the two channel cases. It is clear that the trend followed by the results are the same as that in the case of the comparison of Matlab and Comsol model. The mass flow rate keeps increasing as the model is approximated to a greater extent. The effect of bubbles are approximated by including the void fraction and the effect of current is approximated by including a heat source at the electrodes. The geometry is exact in the case of Comsol with the physics alone being approximated. This leads to the experiments being closer to the Comsol model than the Matlab model. But, all the three cases show a significant rise in the mass flow rate of the electrolyte when the channel was widened which was expected. Accounting for minor losses like bends and including a third network, a heat network, which calculates the temperature of the elements including the losses in an interactive manner with the flow network can potentially improve the results of the Matlab model. Also, more experiments can be done with intermediate values of the channel diameter to obtain a curve for the variation in the mass flow of the electrolyte and the slug flow pattern with respect to the channel diameter.

4.6. Leaking currents

4.6.1. Leaking currents in the single cell and multi-cell setup

Leaking currents were compared for the test setup and the 5 cell model to understand the behaviour of leaking currents in the single cell and a multi-cell setup. The single cell and multi-cell showed different variation of current density and hence, leaking power with the channel diameter as seen in Figure 4.13. The mass flow rate does not keep rising with the channel diameter as observed in Figure 2.11. This is because the resistance in some other part of the system becomes dominant and that decides the mass flow rate of the system and not the channel. Hence, increasing the channel radius beyond 1.5 mm does not benefit mass flow rate. The leaking power curve also flattens out with the increase in radius of the channel in the single cell model. But, in the case of the multi-cell model (Figure 4.13), the leaking power continue rising with the increase in the channel radius. The difference is observed as the effect of the currents leaking from one cell to another is not taken into account in the single cell model.

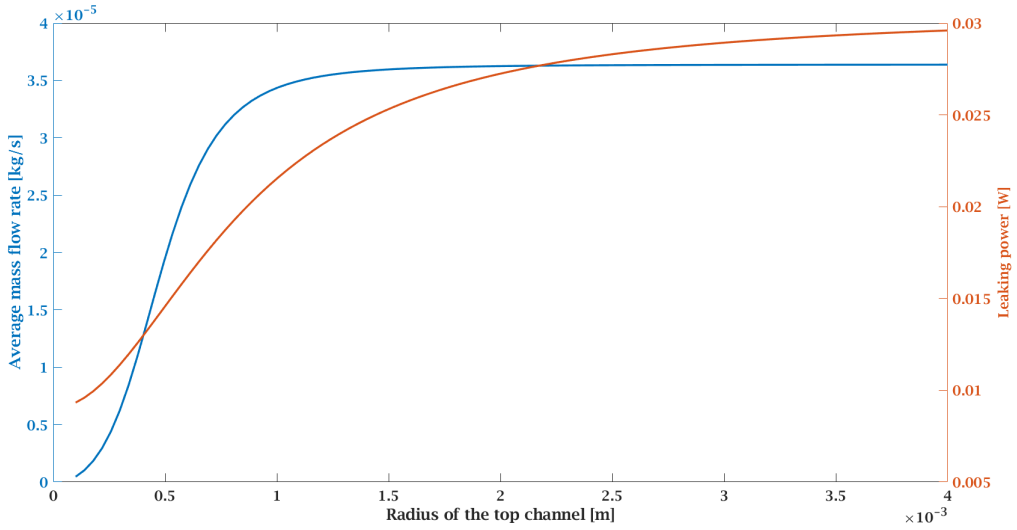

Figure 4.12: Leaking currents and the mass flow rate in the single cell setup. The mass flow rate does not keep increasing like it does in the case of the theoretical model as the resistance in some other part of the system would then determine the flow rate and not this channel.

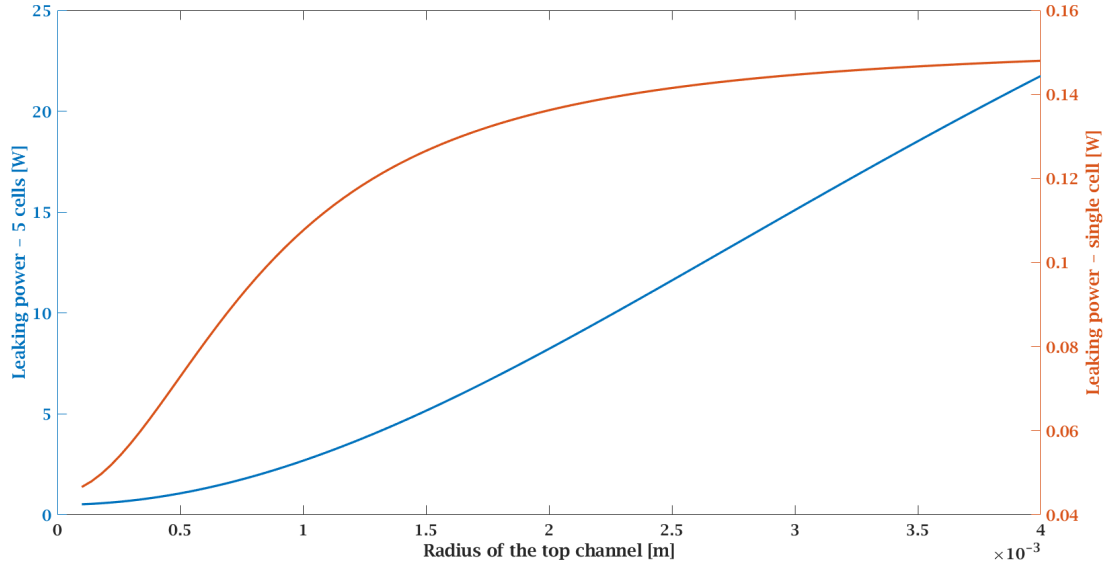

Figure 4.13: Leaking currents in the single and multi-cell setup. The leaking currents are observed to rise continuously as compared to the leaking currents in the single cell model which starts flattening out. Hence, the need for estimation of leaking currents is necessary when it comes to the multi-cell setup.

4.6.2. Effect of the gas slugs on the leaking currents

One way to decrease the leaking currents is by taking advantage of the fact that the effective area of flow decreases when the Taylor bubbles flow through the channel. The equation to find the thickness of the annulus of the electrolyte around a Taylor bubble depends on the Capillary number [3]. The Capillary number is calculated using Equation 2.14,

$$\mathrm{Ca} = \frac{\mu_l v_g}{\sigma_l} = 3.4 \cdot 10^{-4} \tag{4.6}$$

For the obtained Capillary number, the annular thickness is given by Fairbrother and Stubbs [16],

$$\frac{\delta}{r_{ch}} = 0.5\,\mathrm{Ca}^{0.5} = 0.014 \tag{4.7}$$

where δ is the annular thickness. This is considering the radius of the channel to be 1.5 mm. The annular thickness decreases with the reduction in channel diameter. The ratio of the annular thickness to the channel radius is 0.009 which means that the area for the leaking currents to flow is 98% lesser than the case where the electrolyte fills the channel. This leads to the reduction in leaking currents by about 98% through the channel if a Taylor bubble is always present in the channel. If the bubble is present for half of the time, the leaking currents are reduced by about 49%.

Table 4.10: Effect of including gas slugs on the leaking current in the channel

w_{ch} (mm)	Leaking currents (mA)	
	without gas slug	with gas slug
1.5	7	3
3	15	13

Table 4.10 shows the effect of including the gas slugs on the leaking currents in the test setup. A detailed version of this table is provided in Appendix B. Based on the information from Table 4.6 and Table 4.7, the duration of gas slugs were obtained and the average current flowing through the channel was estimated. The effect of gas slug is greater for the narrow channel case as the gas slugs are in the channel for longer duration and hence, the leaking currents are lower.

Table 4.11: Effect of gas slugs on the leaking current and the electrical efficiency of the multi-cell system

Parameter		w_{ch} (mm)	
		1.5	3
Leaking Power (mW)	Without slugs	2.1	3.6
	With slugs	1.2	3.2
Efficiency (%)	Without slugs	98.2	96.9
	With slugs	98.9	97.2

Table 4.11 shows the effect of gas slugs on the multi-cell system. The electrical efficiency increases and in the case of w_{ch} = 1.5 mm, the efficiency goes to 99% which is the goal of ZEF with respect to electrical efficiency. These results are for the case of 5 cell system. The leaking currents were lower for the single cell model but higher in the multi-cell model for the same parameters. The efficiency of the actual system with 18 cells and 2 down-comers (as seen in Figure 2.12) will be lower as the effect of number of cells on leaking currents/power must be considered.

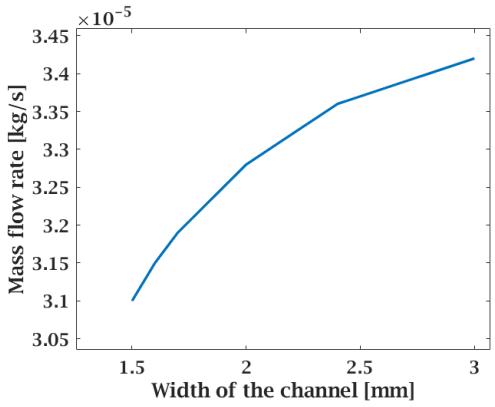

Figure 4.14: Mass flow rate as a function of w_{ch}.

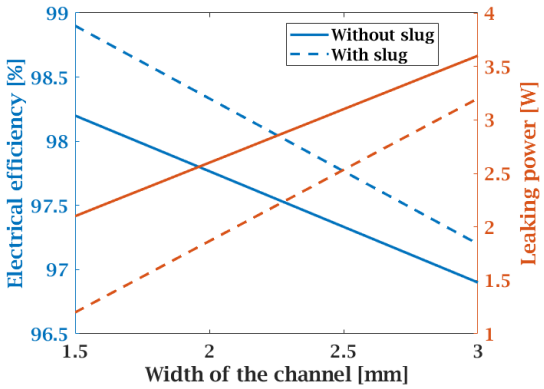

Figure 4.15: Variation of efficiency of electrical efficiency with w_{ch} and the effect of gas slugs.

The effect of gas slugs on the electrical efficiency is seen in Figure 4.15. For small differences in the channel width, the Matlab model did not show significant deviation from a linear curve (curve fit in Appendix A). Hence, the effect of slugs in the intermediate diameter was seen through a linear curve fit. The effect of slug on the electrical efficiency decreases with the increase in width of the channel. Using a linear curve fit, the efficiency at 2 mm channel width is 98.3% with the mass flow rate increasing by 6% as seen in Figure 4.14. Intermediate experiments can be done in future to observe the channel at different dimensions.

If the ZEF alkaline electrolyser has to work with an electrical efficiency of over 99%, then the channel with 1.5 mm diameter would be able to achieve the target considering the effect of the gas slugs on the leaking currents. If the electrical efficiency is allowed to be at 98.3%, a channel width of 2 mm can be used with an improvement of around 6% in the mass flow rate.

5

Conclusions and recommendations

5.1. Conclusions

- **Design modifications**

  The main objective of the thesis was to characterise the alkaline electrolyser system of ZEF and check if the design modification in the system would improve the flow of the system while keeping leaking currents under control. The objective was achieved and the current design was characterised with respect to flow and temperature. But, modifying the channel at the top of the cell led to a few changes. The original design had problems related to flow and temperature. The flow was not steady and the whole electrode in the cell was not used as there was gas trapped at the top of the cell during operation. By removing the part of the channel in the cell, the flow qualitatively improved by making use of the entire area of the electrode. The channel was also widened from 1.5 mm to 3 mm. The flow was observed using high speed camera and fluorescent particles to look at the flow pattern. The new design also improved with more particles moving vertically towards the top of the cell.

- **Modelling and simulations**

  To investigate the performance of the flow part of the Matlab model, it was compared with Comsol simulations and the experiments. Matlab model showed about 25% deviation from the Comsol model and about 65% deviation from the experiments. The bubble diameter obtained from the system was compared to those of the Matlab model as the flow part of the model depends on the void fraction in cell which depends on the bubble diameter. The deviation was about 27%. Time dependent simulations were done on the Comsol model to obtain the heating curve of the electrolyser and the experiments were compared with the simulations. The experiments matched the Comsol model when the external heat transfer coefficient of air was at 15 W/m^2K. The steady state temperature at the hottest part of the system is at 56°C. Insulation is required to operate the system at 90°C.

- **Leaking currents**

  The leaking currents in the setup were investigated using the Matlab model and they scale differently in a single cell system and multi-cell system with respect to the channel diameter. The gas slugs were taken into account for calculating the effective leaking current which showed a considerable decrease in the leaking currents. But, the effect of gas slugs decreases with the increase in diameter as the duration of slugs in the channel reduces. The electrical efficiency is at 99% with the inclusion of gas slugs for the 1.5 mm case and 97% for the 3 mm case. The flow rate of the electrolyte in the channel goes from $3.27 \cdot 10^{-5}$ kg/s to $3.42 \cdot 10^{-5}$ kg/s when the width o the channel was changed from 1.5 mm to 3 mm. A good compromise point would be at a width of 2 mm where the system has a mass flow rate improvement of 6% while decreasing the electrical efficiency from 99% to 98.3%.

5.2. Recommendations

- **Design modification**

  The main recommendation for the system is to remove the part of the top channel which is in the cell. Another suggestion is to increase the diameter of the channels (currently at 1.5 mm) at the top of the cell as it can have a significant effect on the mass flow rate of the electrolyte. Increasing the diameter of the channels beyond 2 mm is not suggested as the leaking currents are affected more than the mass flow rate of the electrolyte. The duration of the gas slugs in the channel decreases with the increase in the diameter of the channel. Hence, larger the channel, lesser the effect of the gas slugs on the leaking currents. Insulating the system is also essential to increase the temperature at the cell. The insulation at the cell need not be provided as the cell would already be insulated by the adjacent cell in the system.

- **Modelling and simulations**

  The Matlab model currently contains the electrical network and the flow network. A heat network can be added to observe the effects of temperature. It is was also seen that the temperature of the system has more impact on the density than the temperature at elevated temperature and pressure. Hence, the model prediction would improve with the addition of the temperature network. Further improvement can be made by including the minor losses in the flow of the system like losses due to bends. Comsol analysis can be improved by using the 'Bubbly flow module'. That will take into account the multi-phase flow of the system.

- **Future experiments**

  More experiments can be done at intermediate values of the channel diameter which will make it more accurate to find the best value of the channel diameter. The experiments must be done for a multi-cell system to get an estimate for the leaking currents as the single cell test setup cannot be used to measure the leaking currents. Higher pressure analysis must be done so that the experiments can validate the flow and the temperature model simultaneously.

A

Comsol and Matlab Modelling

A.1. Approximate modelling

To see the combined effects of flow and temperature and to get a visual plot of the same, a multiphysics simulation was done using Comsol Multiphysics. A simpler 3D model of the actual setup was done using Adobe Fusion 360 software. The model was split into various bodies so that it becomes easier to quantify the flow velocity from the results at a later stage.

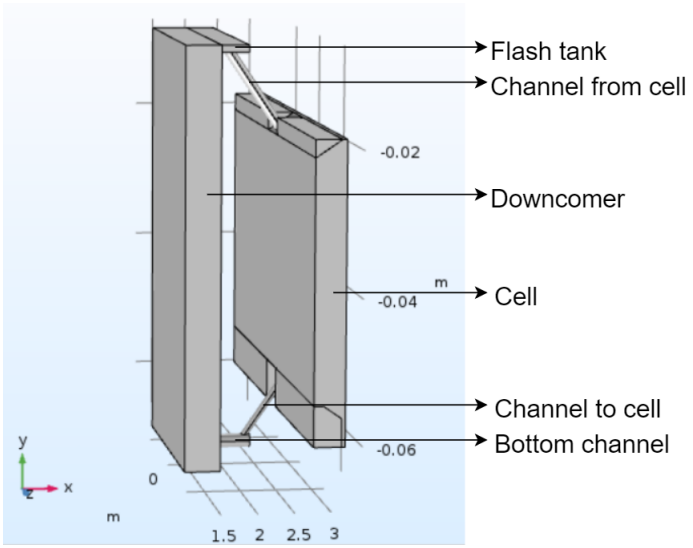

Figure A.1: Various parts of the 3D model used in the analysis

The heat input to the system was from the faces of the electrode and the value of the heat input was calculated based on the voltage and current that is supplied to the system. For alkaline water electrolysis, the thermo-neutral voltage is 1.48 V and assuming supplied voltage as 2 V, the heat input to the system is,

$$Q_{\mathrm{i}} = (V_{\mathrm{supp}} - V_{\mathrm{tn}}) \times I_{\mathrm{supp}} = (2 - 1.48) \times 10 = 5.2\mathrm{W} \tag{A.1}$$

The heat generated due to that is spread across both the electrodes. Initially, the simpler model has one half of the cell with the bottom channel, channel to the cell, channel from the cell and the downcomer. The flow is natural convection and the main driving force for the flow is the formation of bubbles at the cell which decreases the effective density of the fluid in the cell. This buoyancy driven flow is simulated using a volume body force.

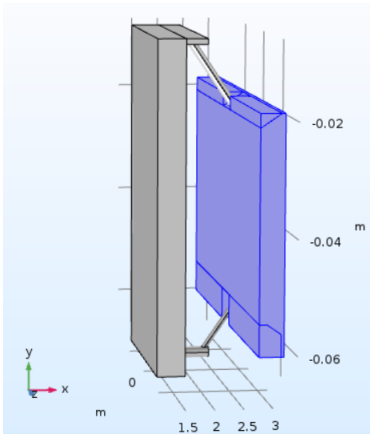

Figure A.2: Part of the body where body force is applied in the system

The laminar flow module in Comsol is used to obtain the flow parameters. The velocity predicted by Matlab model helped in identifying the flow regime and the Reynolds number was low enough for the flow to be considered as laminar flow. The velocity at various sections of the electrolyser was obtained from the Matlab model and that was used to calculate the Reynolds number. Using this value, the order of Reynolds number was estimated by,

$$Re = \frac{\rho_{\mathrm{KOH}} \times v_{\mathrm{KOH}} \times d_{\mathrm{flow}}}{\mu_{\mathrm{KOH}}} \tag{A.2}$$

The value of Reynolds number at various locations is presented in table A.1.

Table A.1: Predicted Reynolds number at various locations of the test setup

Location	d_{flow} (m)	v_{KOH}(m/s)	Re
Downcomer	0.0117	1.27E-04	1.91
Bottom channel	0.002	4.30E-03	11.08
Channel to cell	0.001	1.72E-02	22.15
Cell	0.0093	2.01E-04	2.41
Channel from cell	0.0015	7.85E-03	15.17
Flash tank	0.0102	1.66E-04	2.18

As it can be seen in table A.1, the value of Reynolds number is such that the flow far from the transition Reynolds number of 2300. Hence, the assumption of laminar flow is valid. The effects of gravity is included with the flow being set to incompressible.

In addition to the laminar flow module, the heat transfer in fluids module was used to see the temperature distribution during the flow. In the heat transfer module, a boundary heat source was added where the electrode area is exposed to the fluid and the boundary convection heat flux was described to simulate the heat loss to the walls of the test setup.

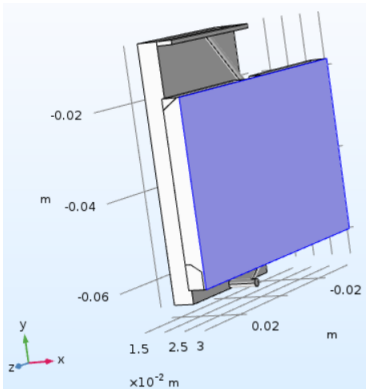

Figure A.3: Face at which the boundary heat source is applied

For the stationary solution case, the following equations were used by Comsol to iteratively solve the given problem:

$$\rho(\mathbf{u}\cdot\nabla)\mathbf{u} = \nabla\cdot[-p\mathbf{I} + \mu(\nabla\mathbf{u} + (\nabla\mathbf{u})^T)] + F_\mathrm{b} + \rho\mathrm{g} \tag{A.3}$$

$$\rho\nabla\cdot(\mathbf{u}) = 0 \tag{A.4}$$

$$\rho c_p\mathbf{u}\cdot\nabla T + \nabla\cdot q = Q + Q_\mathrm{p} + Q_\mathrm{vd} \tag{A.5}$$

Equations A.3 and A.4 are the momentum and mass conservation equations used to solve for the flow part of the problem. Equation A.5 is used to solve for the heat part of the problem. In equation A.3, F_b is the body force given in terms of the void fraction at the cell.

$$F_\mathrm{b} = \alpha \times \rho_\mathrm{KOH} \times g \tag{A.6}$$

where α is the void fraction. The non isothermal flow module was used from the multiphysics menu of Comsol to couple the effects of heat and flow to each other. In the module, there is an option to vary the density of the fluid with the temperature using Boussinesq approximation. This assumes that the density of fluid in the system is a linear function of the temperature. The incompressible flow option was chosen initially to account for the variation in the density only in the body force term using this approximation.

Using a reference temperature, density and thermal coefficient of expansion, the density values can be calculated for other temperature values. This assumption is valid as long as the temperature variation is not too high. EquationA.7 shows the equation form of the effective density of the fluid.

$$\rho_\mathrm{KOH} = \rho_\mathrm{ref}[1 - \beta(T - T_\mathrm{ref})] \tag{A.7}$$

The solution to this problem was computed using a stationary solver using a direct solver as the number of cells were not large enough to exceed the computer memory during computation. The result of the simulation is presented in Figure A.4

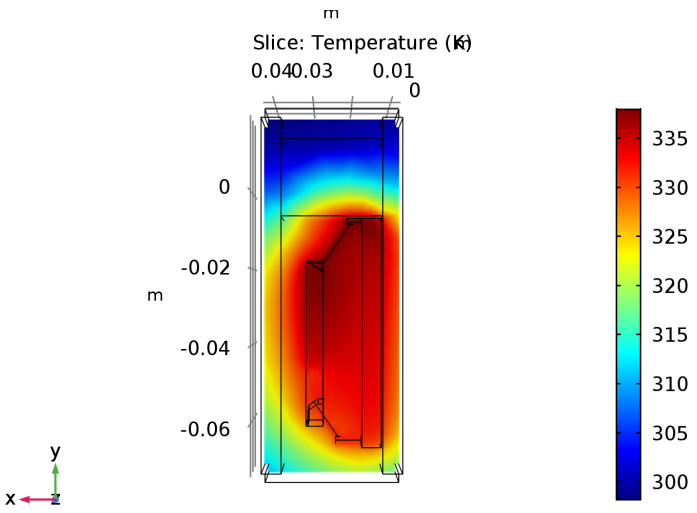

Figure A.4: Results of the comsol simulation for the 3D model of half cell

Comparing the results from both the Matlab and the Comsol model, the values are tabulated in table A.2. The values of velocity and the mass flow rate are displayed in the table. the values from the Comsol model are the volume average values. The mass flow rate in the Comsol model is calculated using the formula,

$$\dot{m}_{\text{com}} = \rho_{\text{KOH}} \times A_{\text{flow}} \times u_{\text{com}} \tag{A.8}$$

the value for the density of KOH is taken as 1280 kg/m^3. The least value of error is seen in the two channels, channel to the cell and channel from the cell. This is because the flow is more unidirectional in the Comsol model at these locations. This leads to the Matlab model being more valid as it does not take into account the back flow that happens in the model at, for example the cell.

The average value of velocity at the cell does take into account the backflow in Comsol and this leads to a lower value of velocity and hence, a lower value of mass flow rate at the cell. Also, the back flow can be confirmed from the larger mass flow rate at the channel to the cell and a smaller mass flow at the channel to the flash tank. Since these effects are not seen in the Matlab model, the mass flow is constant everywhere.

Table A.2: Comparison of results from Matlab and Comsol

Location	Velocity (m/s)		Difference (%)	Mass flow (kg/s)		Error (%)
	Matlab	Comsol		Comsol	Matlab	
Downcomer	2.16E-04	2.84E-04	-31.44	6.57E-05	6.81E-05	-3.70
Bottom channel	1.69E-02	1.26E-02	25.44	5.03E-05	6.81E-05	-35.32
Channel to cell	6.75E-02	6.98E-02	-3.42	7.06E-05	6.81E-05	3.53
Cell	1.66E-04	3.40E-04	-104.73	1.51E-04	6.81E-05	54.88
Channel from cell	3.17E-02	2.97E-02	6.15	6.74E-05	6.81E-05	-1.04
Flash tank	2.59E-04	1.13E-03	-334.36	5.20E-05	6.81E-05	-30.86

A.2. Computer specifications

Table A.3: Computer specifications

Parameter	Value
Processor	Intel® Core™ i5-3470
Number of cores	4
Maximum clock speed	3.20 Ghz
RAM	8 GB
Operating System	Windows 10
Comsol version	5.4

A.3. Grid independence study

Grid independence study was done by me for the choice of mesh. The main limiting factors for the mesh selection are: computation time and the computation power. Since the computer provided had only 8 GB of RAM, the mesh refinement could not be performed beyond a point. This test was done on the model which had the narrow channel.

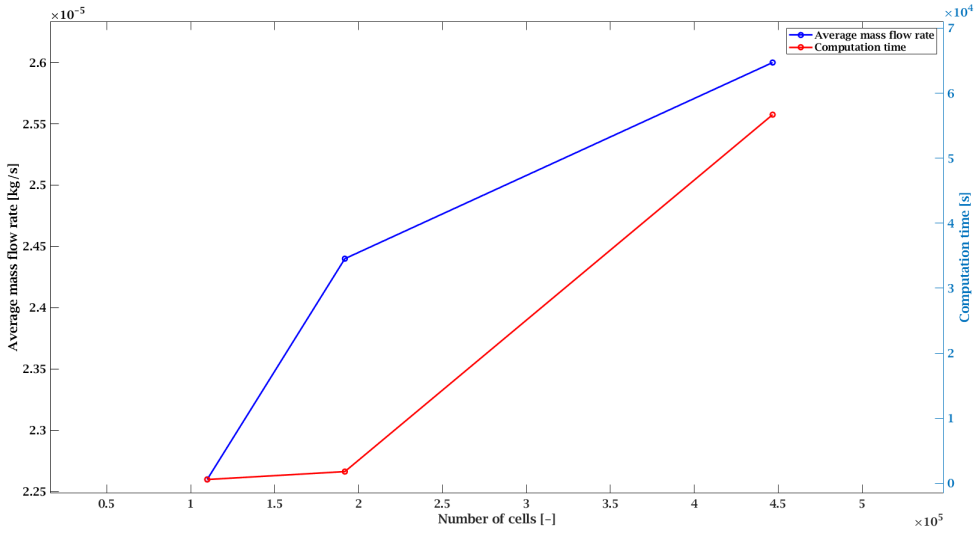

Figure A.5: Results of the grid independence study. The computation time for the mesh corresponding to the 'normal' mesh size is larger than the actual change in the flow rate. Hence, the 'coarse' option was selected as it gave larger difference in the mass flow for smaller delay in producing results.

Figure A.5 shows the result of the grid independence study. It can be seen that three cases were run with different mesh size that resulted in different computation times and different average mass flow rates in the system.

Table A.4: Grid independence study results

Grid size	Number of elements	Computation time (s)	Mass flow rate (kg/s)
Coarser	109821	576	2.26E-05
Coarse	191818	1794	2.44E-05
Normal	446696	56698	2.6E-05

Table A.4 shows the different mesh sizes named by Comsol and the outcomes as a result of choosing them. The change in mass flow rate from coarser to coarse was larger compared to the jump from coarse to normal. The computation time was significantly higher in the normal case as the solver had to switch to slower processing due to limited availability of RAM. Hence, the coarse mesh option was chosen as a balance between accuracy and computation time.

A.4. Figures and tables

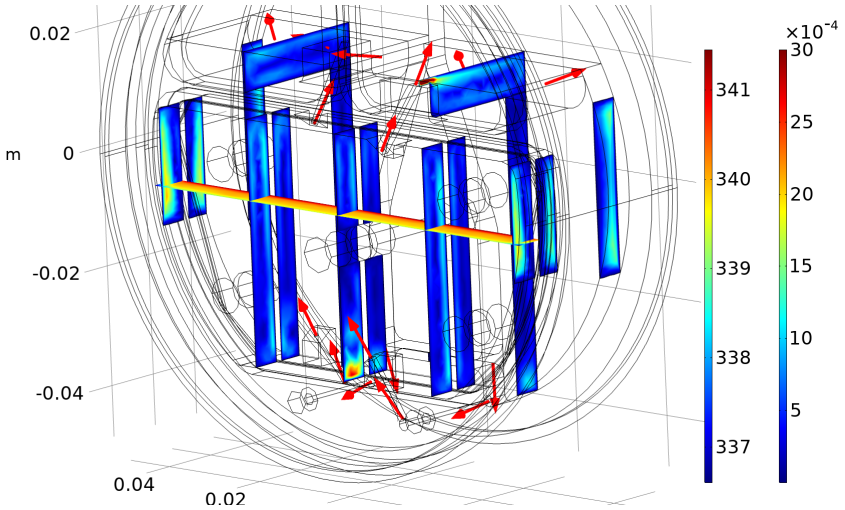

Figure A.6: Flow profile for 10 A of current supplied to the electrolysis system in the narrow channel case with respect to the whole setup.

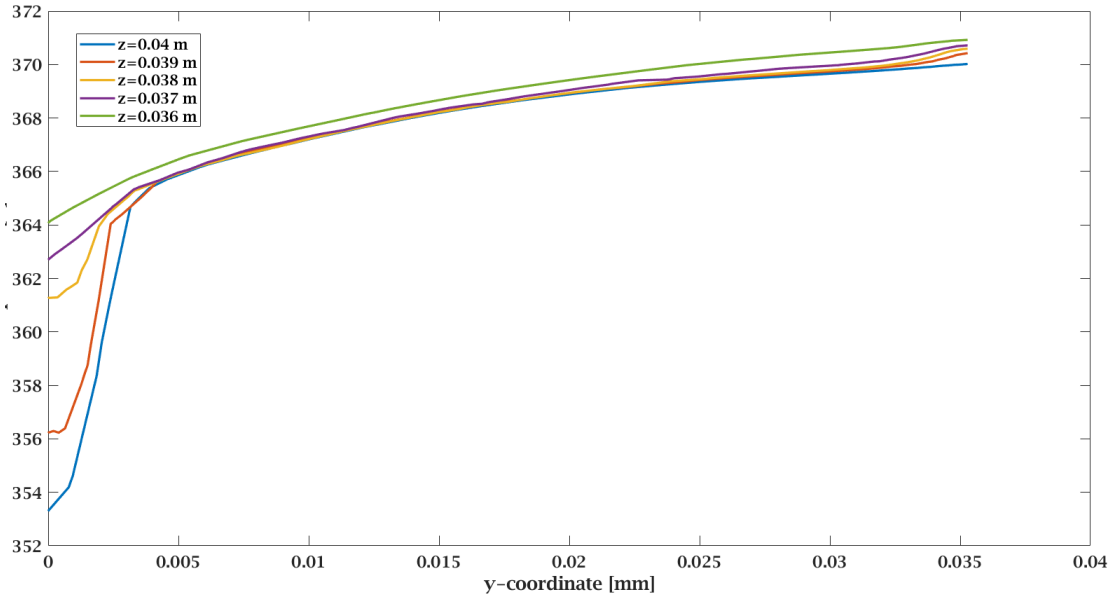

Figure A.7: Temperature profile at different depths in the cell.

Figure A.9 shows the result of velocity of the KOH solution at different locations in the test setup. The colour convention is same for the hydrodynamic results as it is in the case of the electrical results: red for oxygen and blue for hydrogen. The values of pressure at different nodes are also shown in the figures.

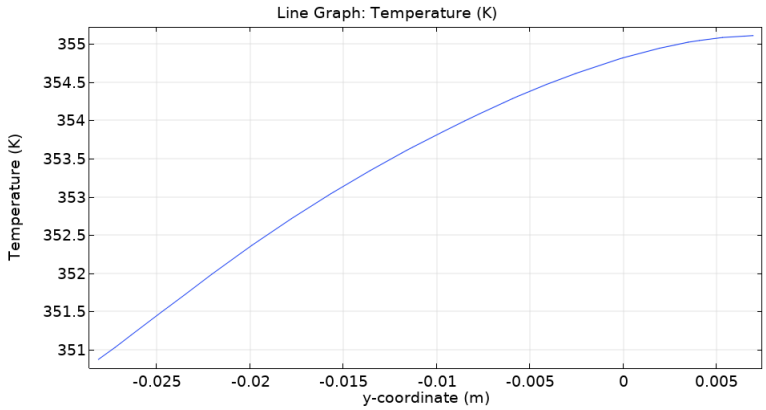

Figure A.8: Temperature profile at the cell obtained using a vertical line of points along the height of the cell

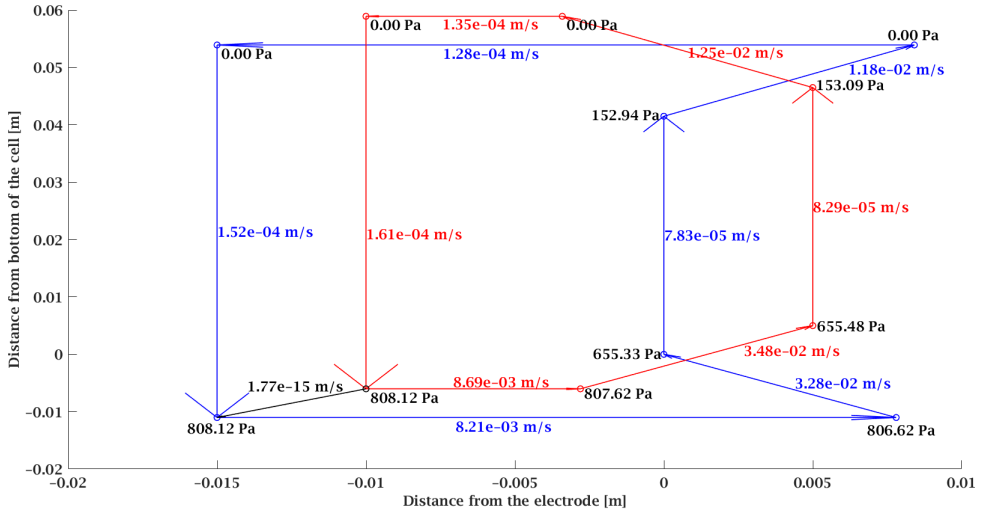

Figure A.9: Velocity of KOH solution in various parts of the setup. The value of leaking current and the power is shown at every element and the expected voltage value is shown at every node. The hydrogen part of the flow is shown by blue vectors and the oxygen part of the flow is shown in red vectors. The flow in the channel connecting the electrolyte on the anode and cathode side is shown in a black vector.

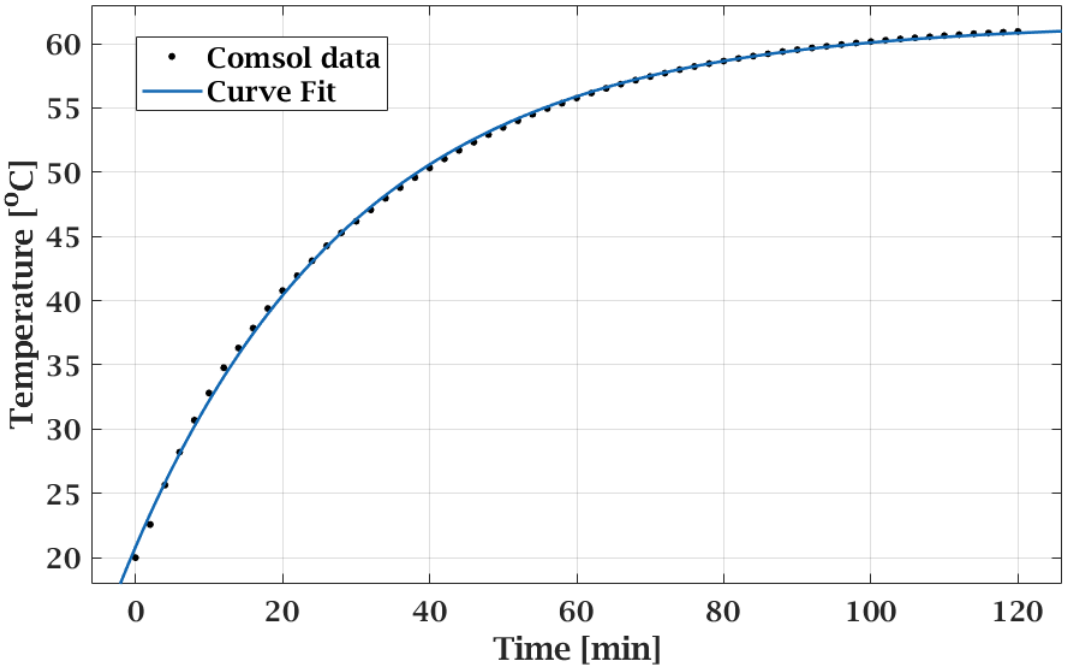

Figure A.10: Comsol heating curve fit in Matlab

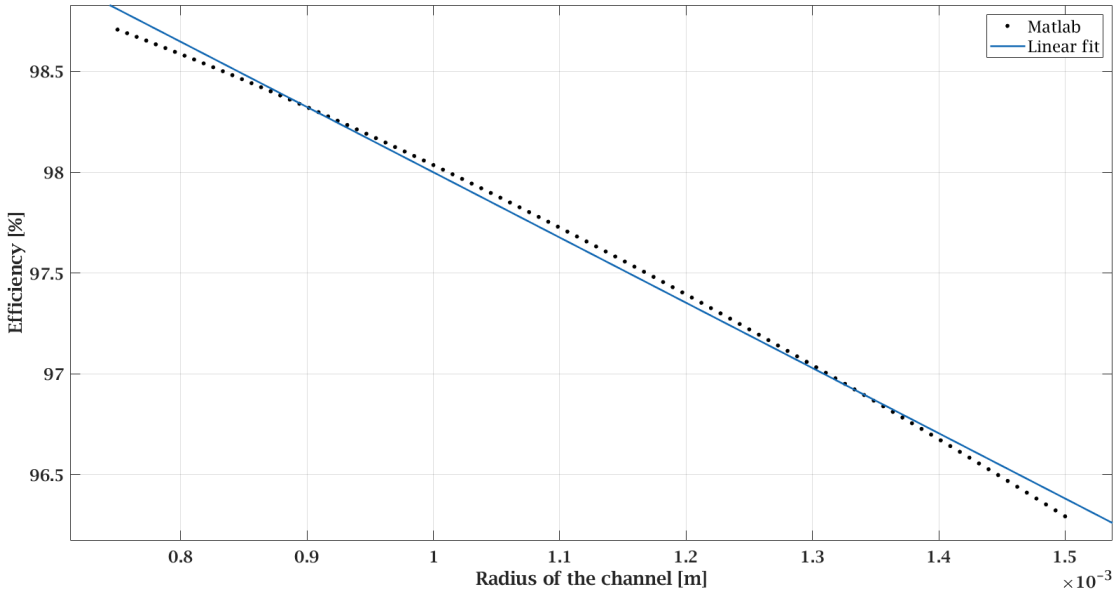

Figure A.11: Fitting a linear curve to the electrical efficiency of the electrolyser

Table A.5: Detailed calculations for the current flow in the top channel for w_{ch} = 1.5 mm

Parameter	A_{flow} (m^2)	Resistance (Ω)	Current (A)	Duration (s)	Current flow (C)
Electrolyte	2.25E-06	32.21	7.45E-03	5.2	0.03875
Gases	4.91E-08	1474.83	1.63E-04	6.7	0.00109
Backflow	0.00E+00	0.00	0.00E+00	0	
			Total	11.9	0.039841

B

Experiments

B.1. Test setup

In order to perform the experiments, the test setup was to be built. The test setup was shown in one of the previous chapters and that was to be manufactured, built and used for obtaining data. The main components of the test setup are:

- **PVC cookies** : The cookies shown in the earlier chapter was manufactured using a small programmable CNC machine. The stock used for manufacturing was made out of Chlorinated Polyvinyl Chloride (CPVC) material. After the manufacturing was done, two holes of 4 mm diameter were made to ensure that the gases generated in the setup are not trapped inside. It also served as a way to add in KOH solution to the mixture as it is being consumed during operation.

- **Temperature sensors** : Thermistors were used as temperature sensors. There was a common calibration curve used for obtaining the temperature values from the absolute voltage value generated from the system. The setup used to obtain the values and log them will be explained later. The temperature sensor is connected as a part of a voltage divider setup.

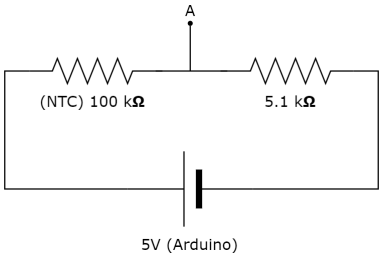

Figure B.1: Voltage divider circuit for the temperature sensor

  The temperature sensors are rated to have 100 kΩ (with a tolerance of 5% (CHECK THIS)) of resistance at 120 °C. The resistance varies with the temperature and it is connected in series with a 5.1 kΩ resistor. The resistors are powered by 5 V from the Arduino mega controller and the absolute voltage in between the resistors is taken from the circuit. This is represented as point A in Figure B.1.

- **Electronics** : The data from the system was obtained using an Arduino Mega controller. The connections of the system are shown in Figure B.2. The Arduino board is powered by a 9 V power supply for the Arduino although it can be powered by 5 V USB supply that the board is connected to. But the USB power supply introduces more noise into the values logged by the Arduino and hence, it is powered by 9 V power supply.

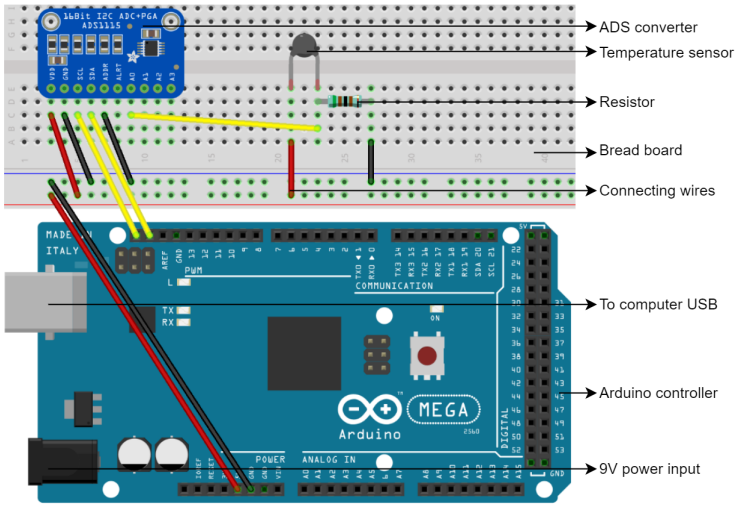

Figure B.2: Connections of the data acquisition system. The connections are shown on a bread board but a PCB was used to make the connections for lesser noise in the signal while obtaining data.

The Arduino power the components on the breadboard with 5 V. The voltage divider setup shown in Figure B.1 is also seen with the connections made to the temperature sensor and the resistor. There is an ADS converter which is an analog to digital signal converter. The analog values of the absolute voltage obtained from the voltage divider setup (connected to port A0 of the ADS) is converted to digital values that are read by the Arduino and then logged on the computer using Arduino software.

- **PMMA cover** : Poly methyl methacrylate is cut by laser cutting for the side covers making the system visually accessible. There are 4 bolts to hold the electrode on the front side of the setup which are also done using laser cutting.

- **KOH solution** : The setup should run with an electrolyte which is 30% Potassium Hydroxide. The solution was prepared by adding KOH pellets containing 85% by mass KOH to calculated amount of water. The density was then measured at room temperature which turned out to be 1240 kg/m^3.

- **Membrane and electrodes** : A stencil was made for the membrane using PMMA material. The stencil was used and the membrane of the right side was cut from the Zirfon stock material. For the electrodes, a slicing machine was used for cutting the electrodes to the right size. An electrical connection bolt is to be connected to the electrode.

  Combi metal glue was initially used for joining the electrode with the bolt. But the connection was not good enough and the bubbles were generated at the bolt rather than the electrode. Spot welding was then used for the connection. But the connection was not mechanically study. Hence, spot welding was used for ensuring good electrical connection whereas metal glue was applied around the bolt to ensure that the connection was mechanically sturdy as well.

- **Glue, seal and clamps** : The temperature sensor and the electrical connection bolt were connected to the PMMA and sealed for leak tightness by using epoxy glue. The advantage of using epoxy glue is the fact that it is transparent. It takes about 30 minutes to dry up after application after which the glue is sturdy.

  Sealing is done in between the CPVC cookies and the PMMA cover by means of silicone rubber. The epoxy glue and silicone rubber are made of two components which are semi solid. Upon mixing the two components, the mixture begins to harden. Approximately 15 minutes is available for applying the sealing and the glue to the area. In the case of silicone rubber, the rubber is applied on to the cookies where sealing is required and then the PMMA cover is placed on it without applying any pressure.

  Once the silicone dries up, the C-clamps are used on either side of the setup to press all the components for the setup against each other and make sure that there are no leaks. There are grooves present in the

setup for including O-rings but they were not required as the system was already leak tight with the above mentioned components at atmospheric pressure.

For this test, table B.1 shows the operating conditions:

Table B.1: Operating parameters for the thermal characterisation

Parameter	Value	Unit
Current	10	A
Voltage	2.4	V
KOH concentration	30	%
Quantity of KOH	54	ml
Density of KOH	1280	kg/m^3
Pressure	1	bar(a)

The test was run for about 8200 seconds and the result of the change in temperature with respect to time is shown in Figure B.3

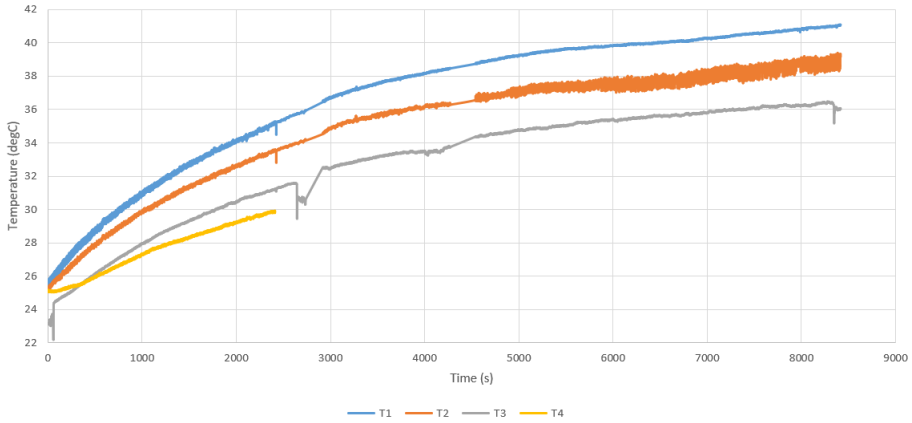

Figure B.3: Temperature change with respect to time for 5A of current

Table B.2: Location of temperature sensors

Sensor name	Location
T1	Front top
T2	Front bottom
T3	Back top
T4	Back bottom

The temperture sensor locations are mentioned in table B.2. The temperature rise is seen but it starts flattening out as the temperature rises. Sensor T4 starts giving out weird values was decided to be disconnected. While disconnecting the sensor, the system was physically moved and that explains the temperature drop around that time. The temperature values begin to follow the expected trend until the end.

Steady state condition was not reached even after the experiment. The temperature values begin to fluctuate and the values begin to form bands as the temperature rises rather than a single value for the sensor T2. A curve fit was done to obtain the equation for these curves and see when the temperature begins to stay constant.

B.2. Flow measurement equipment

The various equipment used to visualise the flow are:

1. **Photron APX-RS high speed camera**: Photron APX-RS high speed camera was used to capture the information required from the flow. The specifications of the camera are mentioned in table B.3

Table B.3: Specifications of Photron APX-RS high speed camera

Parameter	Value/Range
Sensor type	10-bit CMOS
Pixel size	17 μm
Connection mode	Ethernet
Maximum resolution	1024x1024 pixels
Colour mode	Monochrome
Internal memory	8 GB
Minimum frame rate	60 fps

Images were obtained at a rate of 60 fps and 125 fps. For the memory available on the camera, 49.2 seconds of video can be shot at 125 fps at a resolution of 1024×1024 pixels. Live information was obtained from the camera by connecting it to a computer through ethernet cable.

2. **Nikon lens**: The lens used in the setup is the Nikon Micro Nikkor 105 mm f/2.8 lens. The specifications of the lens are in table B.4

Table B.4: Nikon lens specifications [1]

Parameter	Value/Range
Focal length	105 mm
Maximum aperture	f/2.8
Minimum aperture	f/32
Focus mode	Manual
Filter size	52 mm

3. **High power light source**: Zeiss Schott KL 1500 electronic was used as a light source for the experiments. The light was green in colour. There were two bright sources of halogen lamps whose colour can be changed by means of a filter inside. The light can also be filtered using external filters if internal filters are not good enough.

4. **UV filters for the camera**: UV filters were used on top of the lens to filter only one wavelength of light through it. The fluorescent particles are orange in colour and if rest of the setup is lit with a light source of wavelength far from orange, then the camera can only 'see' the particles while rest of the setup is seen as dark. A UV filter of green wavelength was also used for the light source to filter out the part of light with the wavelength close to orange.

5. **Fluorescent particles**: Fluorescent particles were used to obtain the flow pattern inside the test setup at the cell. The specifications of the particles are given in table B.5

Table B.5: Properties of the fluorescent particles added to the flow

Parameter	Value/Range
Colour	Orange
Size	13 μm
Density	1.1 g/cm^3

6. **Camera stand, mount and other accessories**: A speaker stand was used to raise the camera to the required height and a mount was used to attach the camera to the stand. An ethernet cable was used to establish connection between the camera and the computer. A computer was used to view, save and process the data obtained from the camera. Photron PFV ver.3691 was the software used to read and save information from the camera.

B.3. Flow measurement technique

The bubbles and the particles in the flow are tracked using single particle tracking technique. A Matlab code was written for manual particle tracking. At any given moment, one partcile/bubble is tracked. The code mainly consists of three parts:

1. **Reading the frame/image**: Every frame is read either from the folder directly if the image is available in tif format. Sometimes, a video was captured and those had to be converted to frames before they are read into the code again. Since every particle is tracked at different points of time, the frame from which the tracking should begin was also given as input.

2. **Obtaining the coordinates of the bubble/particle**: The coordinates of every bubble/particle is obtained by using a Matlab function called *getpts*. The *getpts* function gives coordinates of the mouse-click. This is used to obtain the coordinates of the bubble/particle. This value obtained is in terms of pixels of the image.

3. **Converting the coordinates to the distance/trajectory**: The obtained coordinates of the mouse-clicks are converted in terms of vertical distance. The *getpts* function allows obtaining coordinates of more than one mouse-click per frame. Hence, while tracking every time, the first frame is allowed to obtain more than one point.

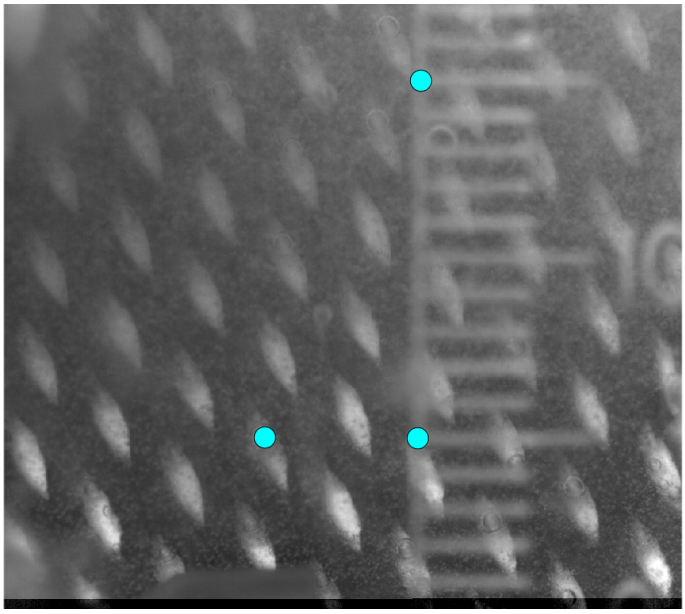

Figure B.4: Mouse tracking example for one frame. This is the first frame for tracking the bubble. The circles marked are the mouse-clicks. The two mouse-clicks can be seen on the scale at 5 mm and 15 mm. The coordinates of these two points are used to convert other points in the code from pixel values to mm values.

Figure B.4 shows an example of first frame in tracking one of the bubbles. The first click in every frame corresponds to the coordinates of the bubble/particle. The second and third mouse-click of the first frame corresponds to two points on the scale of the setup which can be any two values. Usually it is either 5 mm distance or 10 mm distance. This is used to obtain a correlation between the coordinates and the actual distance travelled. A right click or a double left click is used to continue to the next frame and obtain the coordinates of the bubble in the next iteration.

B.4. Figures

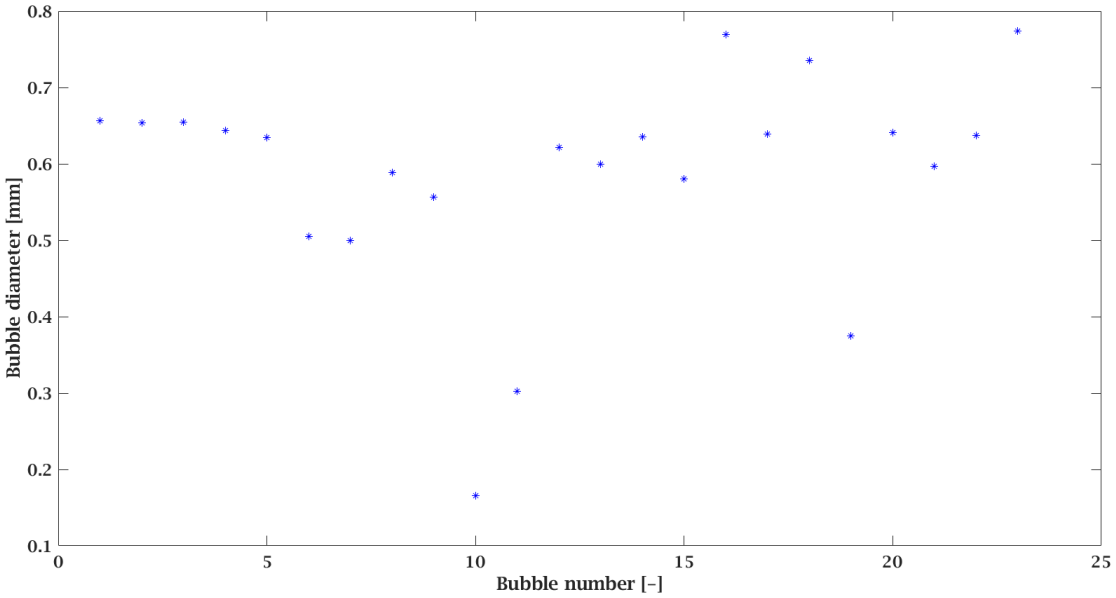

Figure B.5: Diameter of the bubbles measured in the flow while leaving the electrode

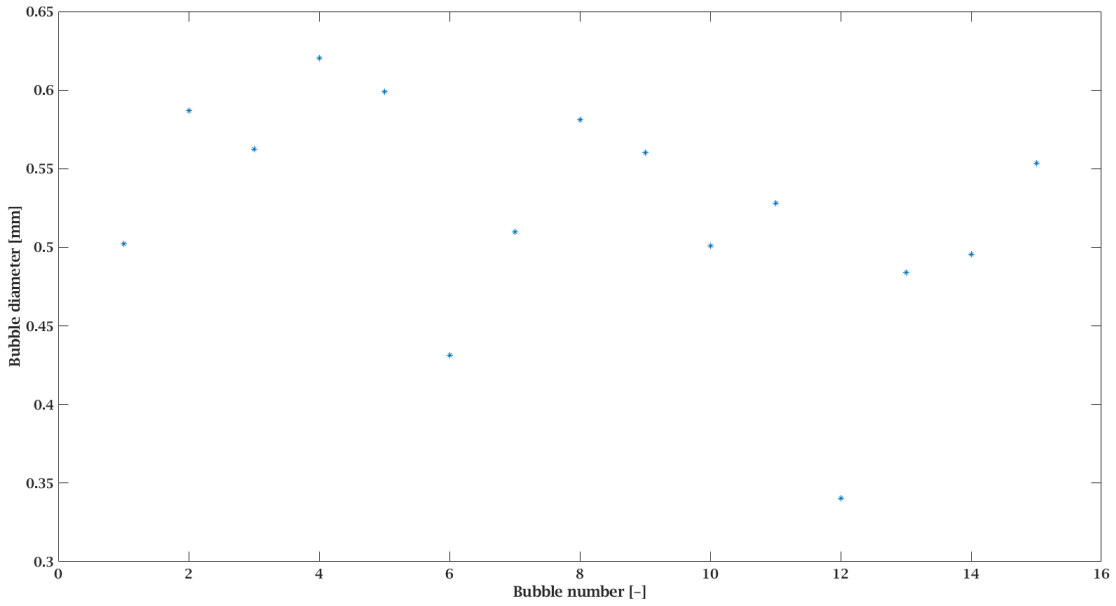

Figure B.6: Bubble diameter in the wide channel case

B.5. Variation of bubble velocity with diameter

The bubble velocity increases with the increase in the bubble diameter. But the relation of the bubble velocity with the diameter is different based on the Reynolds number [30]. The technique used to follow the bubbles and obtain the coordinates have already been in mentioned in the previous chapters. The bubble velocity was obtained by linear curve fitting the line in the graph of distance vs time. The time of rise (t_g)for every bubble,

distance travelled by bubble (h_g) and the velocity of the bubble (u_g) were obtained using the equation,

$$h_g = \frac{N_{p,g} \times h_{scale}}{N_{p,scale}} \tag{B.1}$$

$$t_g = \frac{N_f}{N_{fps}} \tag{B.2}$$

$$u_g = \frac{h_g}{t_g} \tag{B.3}$$

The velocity is obtained from the slope of the curve fitting equation. The bubble diameter is obtained by masking the bubble diameter and using *imfindcirlces* function in Matlab. This will identify all the bubbles and the right bubble is chosen after which the radius is obtained in terms of pixels. The radius is converted to mm scale using the same method as in the case of obtaining the bubble coordinates.

The boundary of two regimes for the graph in the bubble velocity vs bubble diameter is at the point on x axis where Reynolds number is less than 1. The Reynolds number is given by,

$$Re = \frac{\rho_l (v_g - v_l) d_g}{\mu_l} \tag{B.4}$$

The stokes drag force (F_s) is given by,

$$F_s = 3\pi \mu_l d_g (v_g - v_l) \tag{B.5}$$

The buoyant force (F_b) is given by,

$$F_b = \frac{\pi}{6} d_g^3 g \rho_l \tag{B.6}$$

Equating Equation B.5 and Equation B.6,

$$v_g = v_l + \frac{\rho_l g d_g^2}{18\mu_l} \tag{B.7}$$

For Reynolds number greater than 1, the relation between the bubble velocity and the bubble diameter becomes,

$$v_g = v_l + \frac{f \rho_l g d_g}{\mu_l} \tag{B.8}$$

Using Equation B.7, the value of diameter where Reynolds number is equal to 1 can be obtained.

$$Re = \frac{\rho_l^2 d_g^3}{18\mu_l^2} \tag{B.9}$$

Using Equation B.9, the diameter at which the Reynolds number is equal to one is given by,

$$d_g = \sqrt[3]{\frac{18 \times (1.5 \times 10^{-3})^2}{1200^2 \times 9.81}} = 0.142 \times 10^{-3} \text{m} \tag{B.10}$$

Hence, approximately, until a bubble diameter of 0.1 mm, a quadratic relation will exist for the graph of bubble velocity vs bubble diameter. For bubble diameter values greater than 0.1 mm, the relation will gradually approach to being linear. Using this information, curve fitting was done for the information obtained.

B.6. Estimation of bubble diameter and velocity at the cell

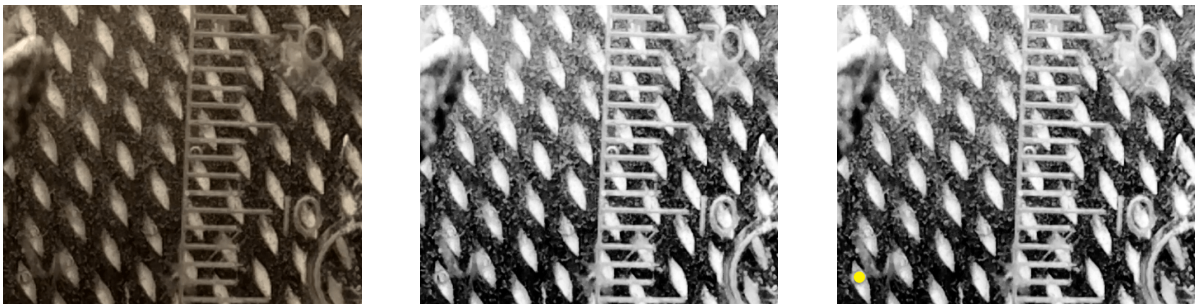

(a) Original image (b) Histogram equalised image (c) Patching the bubble

Figure B.7: Different steps taken in image processing for measuring bubble diameter

Figure B.7 shows the steps taken for obtaining the bubble diameter of one of the bubbles. This is in the case of the large bubbles. The original image (Figure B.7a) is taken and the Matlab code is ran to perform histogram equalisation on the image so that the boundaries of the bubbles are more clear to be distinguished. The histogram equalisation is done after converting the image to grayscale. The result is seen in Figure B.7b. The final stage in separating the bubble from the background is to patch the bubble with a colour that has a good contrast with the background. The final image (Figure B.7c) was used to obtain the bubble diameter through a Matlab code and imfindcircles command.

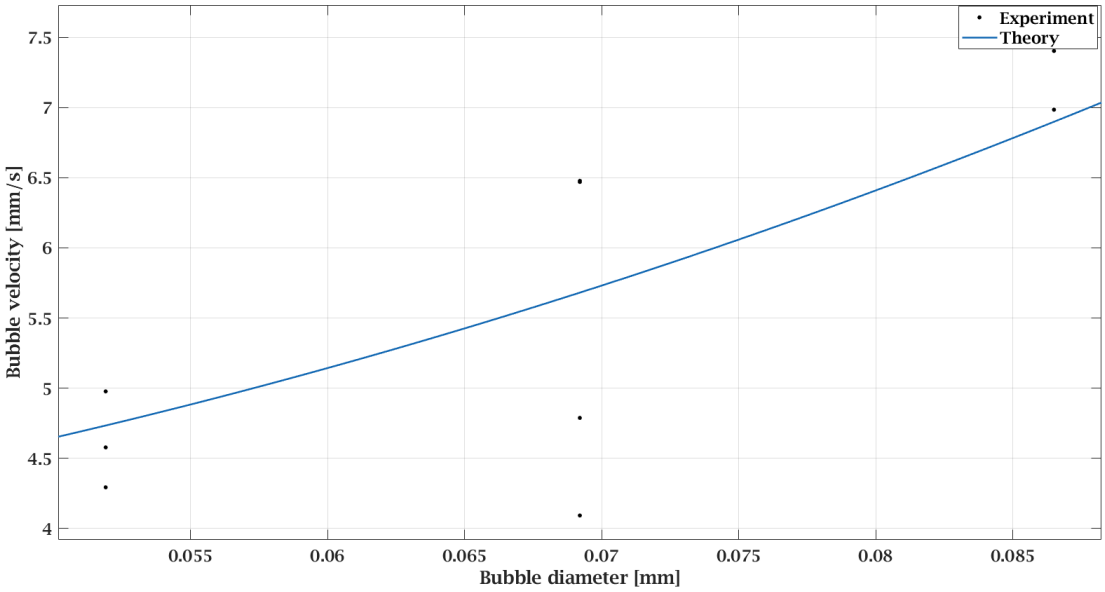

Figure B.8: Bubble velocity vs diameter for the wide channel for Reynolds number lesser than 1.

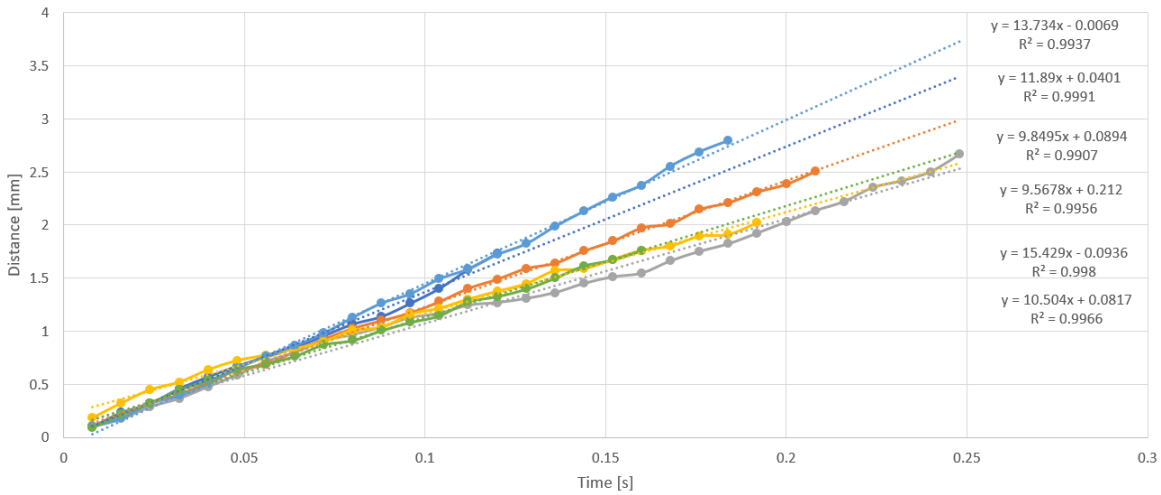

Figure B.9: Distance-time plot of the particles tracked in the wide channel case

The goodness of fit for the temperature profile curves for the equation is given in Table B.6

Table B.6: Goodness of fit parameters for the temperature curves at four measurement points

Parameter	**y1**	**y2**	**y3**	**y4**
SSE	29.84	40.06	410.1	136.9
R-square	0.9994	0.9991	0.9926	0.9957
Adjusted R-square	0.9994	0.9991	0.9926	0.9957
RMSE	0.1573	0.1823	0.5832	0.3369

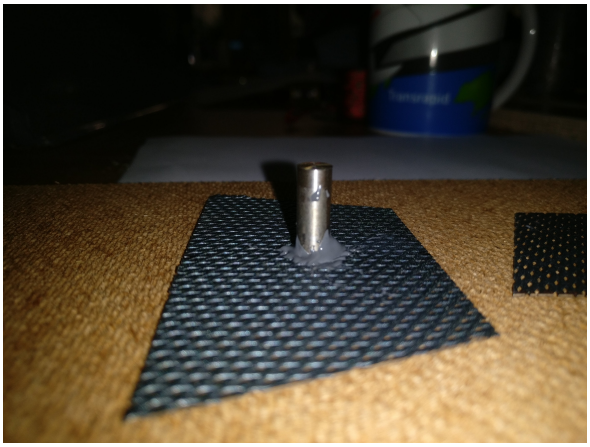

(a) Electrical bolt attached to the electrode

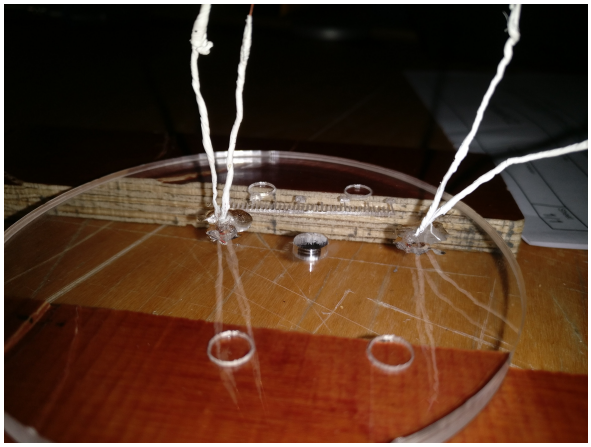

(b) NTC attached to the PMMA using epoxy glue

Figure B.10: Electrode bolt connection and the NTC on the PMMA

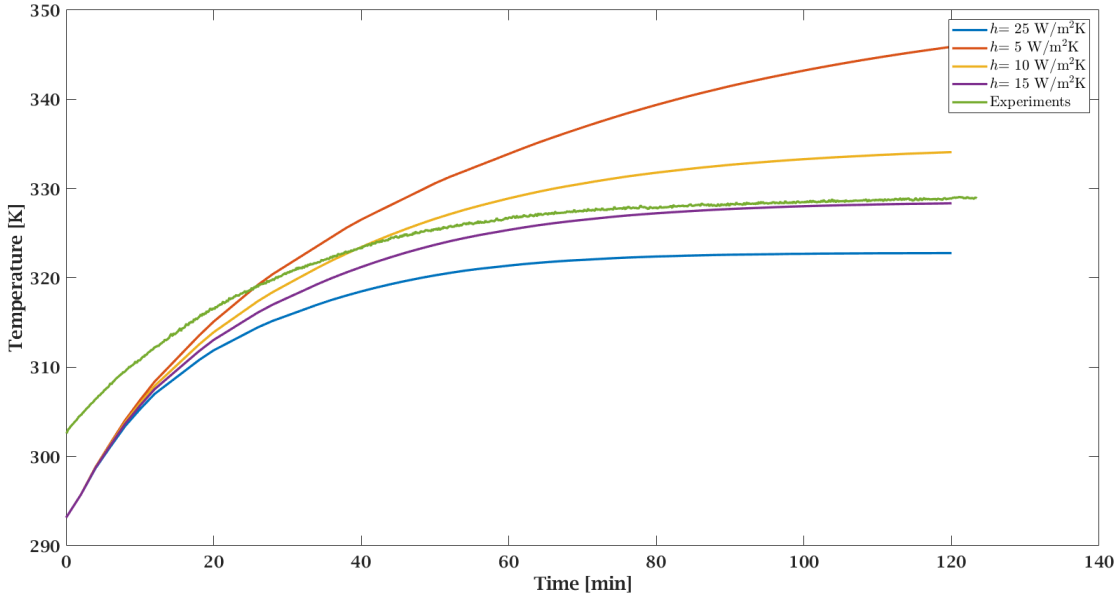

Figure B.12: Heating curves obtained from Comsol for different values of $h_{c,air}$ along with the heating curve from the experiments. The temperature of the electrolyte in the experiments were not at room temperature when the experiments began. But the trend is similar. The coefficients can be used to compare the expected value of heat transfer coefficient.

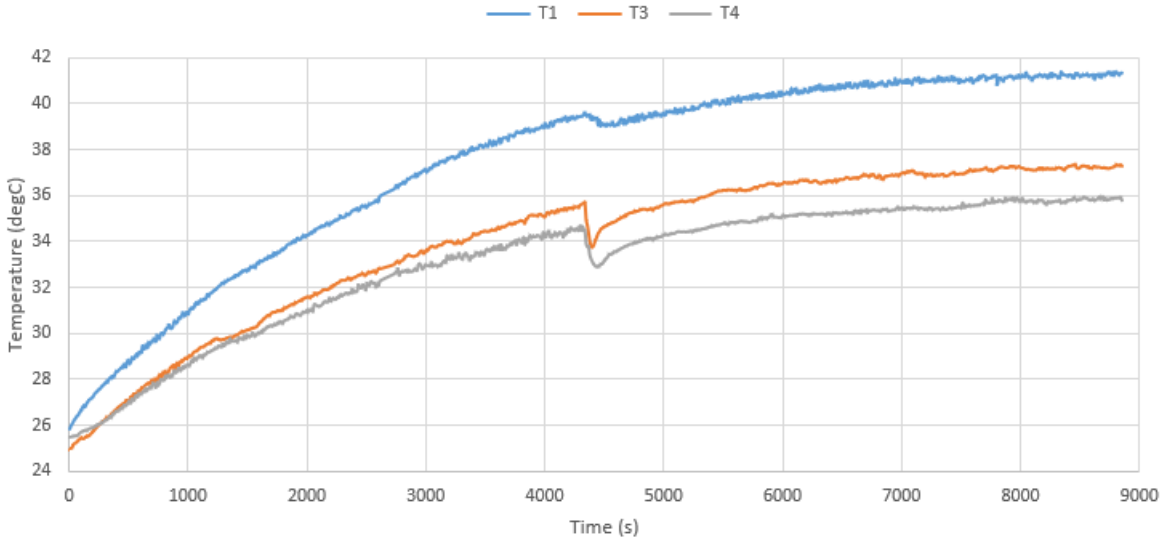

Figure B.11: Effect of temperature drop due to addition of KOH

C

Literature

C.1. Efficiency of an electrolyser

There are various definitions for the efficiency of an electrolyser. Some of them are mentioned below:

- **Enthapy efficiency:**

$$\gamma_{\Delta H} = \frac{V_{\text{tn}}}{V_{\text{applied}}} \tag{C.1}$$

  At low current densities (j≈0), $V_{\text{tn}} \approx V_{\text{applied}}$ and $\gamma_{\Delta H} \approx 1$

- **Faradic efficiency:** Faradic efficiency is the ratio of the actual volume of hydrogen produced to the theoretical volume of hydrogen that is supposed to be produced.

$$\gamma_F = \frac{Q_{\text{actual}}}{Q_{\text{theo}}} \tag{C.2}$$

  If the process has 100% faradic efficiency, it would mean that every electron that is produced is being used by protons to form hydrogen. This efficiency is closer to 1 and the reasons for the deviation from 100% efficiency are energy used for electrolysis of impurities, spontaneous recombination of the products due to improper separation and formation of stray currents in the stack.

- **Energy efficiency:** The energy efficiency of the electrolyser is the ratio of the energy available from the produced hydrogen to the energy consumption of the cell.

$$\gamma_{\text{energy}} = \frac{\text{moles of } H_2 \text{ produced} \times \text{HHV}_{H_2}}{I \times V \times t} \tag{C.3}$$

- **Thermodynamic efficiency:** The thermodynamic efficiency is the ratio of the change in Gibbs free energy to the change in enthalpy.

$$\gamma_{\text{TD}} = \frac{\Delta G}{\Delta H} \tag{C.4}$$

  The denominator does not vary so much with the temperature. But the $T\Delta S$ increases with temperature. This would mean that the numerator decreases with the temperature. γ_{TD} is the fraction of electricity to be added and since the numerator reduces with temperature, less electricity needs to be added at higher temperature.

C.1.1. Velocity of KOH solution

A numerical study was done to investigate the flow and thermal characteristics in a micro channel [10]. In one method, the temperature difference between the top and bottom wall was observed. In the second method, the bottom wall was heated to notice the buoyancy effect induced as a result of the temperature differences.

The most optimal location to place the sensors was found to be on the top and bottom walls. The best measurement method to adopt for extremely low velocity is the temperature difference induced buoyancy effect.

Thermal flow sensors can be used for the measurement of the velocity [15]. Thermal flow sensors are a combination of heaters and temperature sensors. The principle of the thermal micro flow sensor is presented in Figure C.1. The temperature field is represented in red which changes with the flow velocity. This change is captured by the temperature sensor and the sensed field is used to measure the velocity.

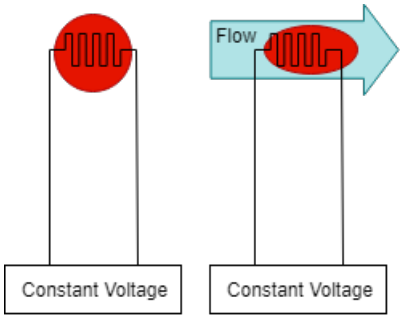

Figure C.1: Principle of thermal micro flow sensor [23]

Three different types of thermal sensors were discussed, namely, anemometers, calorimetric flow sensors and time of flight sensors.

Anemometers work under the principle that the temperature change in a material causes a change in the resistance it offers. The response of the anemometer is proportional to the square of the flow velocity.

Calorimetric flow sensors uses various temperature sensors around the heater to observe change in the temperature distribution around the heater. These sensors are useful to measure very low flow velocity. In time of flight sensors, a heat pulse is fed to the fluid and a temperature sensor located downstream detects its delay. Measuring time in this mode, the sensors will be able to determine the velocity of the fluid.

Time of flight sensors have a heating device which is placed at a certain distance before the temperature sensor. The heating device creates a temperature field which is carried by the flow field and is sensed by the temperature sensor. The variation in the temperature field observed is used to compute the velocity.

C.1.2. Transport resistances:

Ionic transfer within the electrolyte is dependant on factors like electrolyte concentration, diaphragm between electrodes and distance of separation between anode and cathode. The viscosity and flow field of the electrolyte determine the ionic transfer, bubble size, rising velocity and temperature distribution.

Recirculating and mixing the electrolytes helps to prevent further rise in over-potential due to difference in the electrolyte concentration in the cell. The velocity of the fluid can help in the removal of gas and vapour bubbles from the electrodes. The re-circulation of electrolyte facilitates even distribution of heat within electrolyte.

If the bubble coverage is denoted as θ, then the electrical resistivity due to bubble coverage is given by,

$$\rho = \rho_0 (1-\theta)^{-\frac{3}{2}} \tag{C.5}$$

where p_0 is the specific resistivity of the gas free electrolyte solution. If a membrane is used for the separation of hydrogen and oxygen gas that is evolved, then the membrane adds to the resistance to ionic transfer. The resistive effect is expressed as apparent conductivity in equation C.6.

$$\kappa_{\text{membrane}} = 0.272 \frac{\kappa m^2}{p} \tag{C.6}$$

where p is the permeability of the membrane and m is the hydraulic radius.

C.2. Electrode kinetics

The rate of the reaction depends on the nature and pre-treatment of the electrode surfaces and the composition of the electrolyte in the vicinity of the electrode. The ions in the electrolyte near the electrode, forms

layers, called double layers. For example, at the cathode, the charge layer is formed by hydroxyl ions and potassium ions. The double layer is shown in Figure C.2

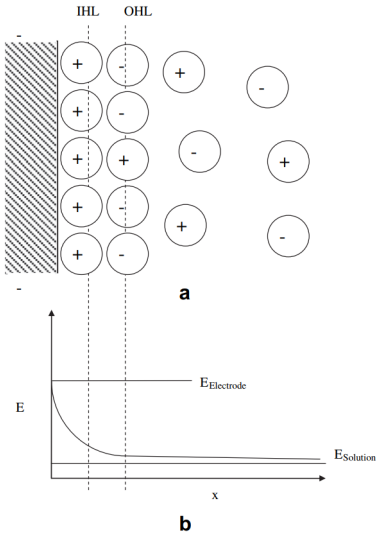

Figure C.2: Representation of the (a) double layer and (b) the potential distribution near electrode surface

The ions that are accumulated, form two mobile layers of solvent molecules and adsorbed species. The layer closer to the electrode surface is called the Inner Helmholtz Layer (IHL) which is relatively ordered. The layer away from the electrode is called as the Outer Helmholtz Layer (OHL), which is the one with less order.

It is evident that there is a potential difference between the electrode surface and the electrolyte. Since formation of double layer is a non faradaic process, charge is progressively stored and this leads to electrodes acquiring properties of a capacitor.

According to Faraday's law, the number of moles of electrolysed species, N, is given by

$$N = \frac{Q}{nF} \tag{C.7}$$

where F is Faraday constant, n is the stoichiometric number of electons consumed (2 in the electrolysis of water), Q is the total charge in Coulomb transferred during the reaction. The rate of reaction is given by,

$$\text{Rate} = \frac{\mathrm{d}N}{\mathrm{d}t} \tag{C.8}$$

Also, taking surface area into account,

$$\text{Rate} = \frac{j}{nF} \tag{C.9}$$

where $j = \frac{i}{A}$, is the current density, $i = \frac{\mathrm{d}Q}{\mathrm{d}t}$, is the Faraday current. The simplified form of Butler-Volmer equation is given by,

$$i = i_0(e^{-\alpha f \gamma} - e^{(1-\alpha) f \gamma}) \tag{C.10}$$

where i_0 is the exchange current density defined as the current of reversible water splitting reaction. The rate of reaction depends on the over-potential which in turn depends on various factors. One of the factors is activation energy which shows strong dependence on the electrode material. The reaction rate and activation energy are inversely proportional, but, the activation energy and current density are directly proportional which can be lowered by using the right electro-catalysts.

C.2.1. Electrochemical reaction resistances

The mechanism of hydrogen evolution reaction involves the formation of adsorbed hydrogen (equation C.11) followed by chemical desorption (equation C.12) or electro-chemical desorption (equation C.13).

$$H_2O + e^- \longrightarrow H_{ads} + OH^- \tag{C.11}$$

$$2H_{ads} \longrightarrow H_2 \tag{C.12}$$

$$H_{ads} + +e^- + H_2O \longrightarrow H_2 + OH^- \tag{C.13}$$

It is to be noted that equations C.11, C.12 and C.13 do not proceed with the same reaction rate. The rate determining step is to be identified for the hydrogen evolution reaction as it will decide the relative importance of the electrode properties.

If hydrogen adsorption is the rate determining step, electrode material with more edges and cavities will create more electrolysis centres for hydrogen adsorption. This will favour easy transfer of electrons. If hydrogen desorption is the rate determining step, then, physical properties like surface roughness or perforation will either increase electron transfer or reduce the bubble size, increasing the electrolysis rate.

When the over-potential is low, electron transfer is slower than desorption. Hence, adsorption will be the rate determining step. If the over-potential is high, the hydrogen adsorption rate will be greater than desorption rate. Hence, hydrogen desorption will be the rate determining step.

The generally accepted mechanism for the oxygen evolution reaction is as follows:

$$OH^-_{ads} \longleftrightarrow OH_{ads} + e^- \tag{C.14}$$

$$OH^- + OH^-_{ads} \longleftrightarrow O_{ads} + H_2O + e^- \tag{C.15}$$

$$O_{ads} + O_{ads} \longleftrightarrow O_2 \tag{C.16}$$

The variation in the thermo-neutral voltage explained using the Gibbs equation and is shown in Figure C.3. $T\Delta S$ has a linear variation with temperature as ΔS is almost constant. The total energy requirement is ΔH which is almost constant with the lines for both enthalpy and entropy having discontinuity at 100 °C due to evaporation of water. As a result, the Gibbs free energy (ΔG) decreases with the rise in temperature.

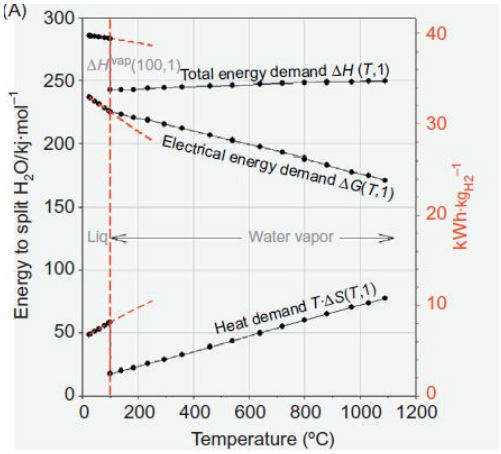

Figure C.3: Variation of $T\Delta S, \Delta G$ and ΔH with temperature at 1 bar [6]

If the angle of the channel had to be kept constant, the height of the channel scales with the length of the channel. This would mean that the flow rate is independent of the length of the channel making the flow rate depend only on the radius of the channel.

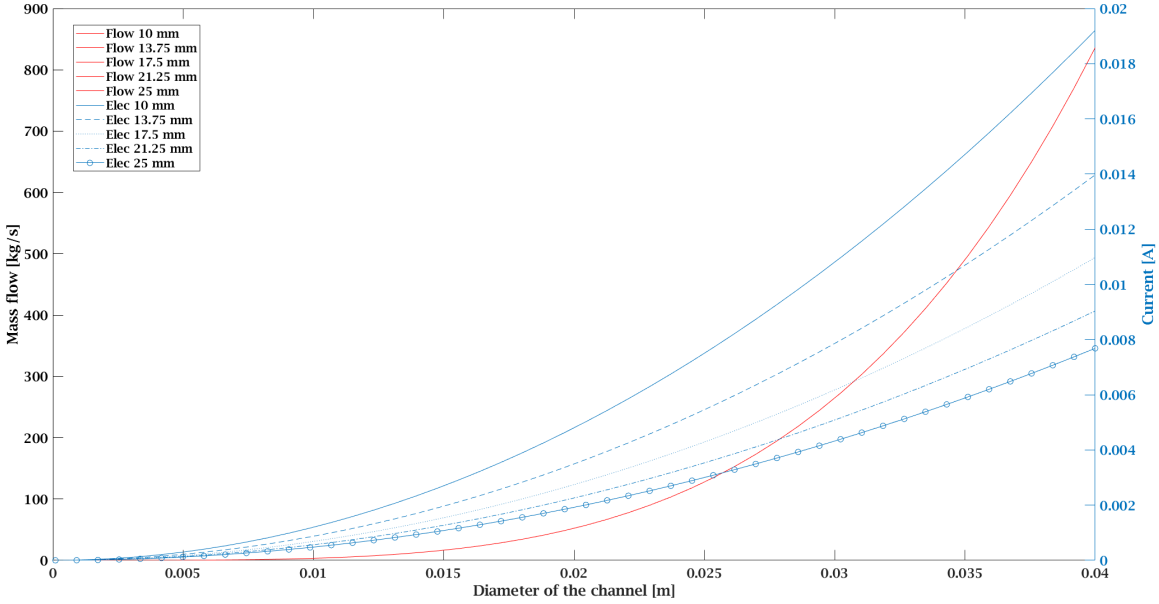

Figure C.4: Variation of the mass flow rate and the leaking current with the diameter of the top channel. The pressure drop and the resistance scale linearly with the channel length and hence, all the lines representing the mass flow rate are overlapping on one another. The mass flow is observed to raise continuously with the channel diameter. The leaking currents also increase with the diameter of the channel but decrease with the length of the channel

When the current density was increased from 0.3 to 0.6 mA/cm^2 in the ZEF electrolyser, the critical diameter increased from 0.59 to 1.09 mm. The bubble size decreases with the electrolyte circulation. However, it was found that there was a bubble curtain on the surface of the electrode and was contributing to the total resistance of the process [18]. This also caused a small reduction in the cell voltage.

Bibliography

[1] Micro-Nikkor 105mm f/2.8 lens from Nikon. URL https://www.nikon.co.uk/en_GB/product/nikkor-lenses/manual-focus-lenses/single-focal-length/micro-nikkor-105mm-f-2-8#tech_specs.

[2] A. A. Adamczyk and L. Rimai. 2-Dimensional particle tracking velocimetry (PTV): Technique and image processing algorithms. *Experiments in Fluids*, 6(6):373–380, 1988. ISSN 07234864. doi: 10.1007/BF00196482.

[3] P. Angeli and A. Gavriilidis. Hydrodynamics of Taylor flow in small channels: A review. *Proceedings of the Institution of Mechanical Engineers, Part C: Journal of Mechanical Engineering Science*, 222(5):737–751, 2008. ISSN 09544062. doi: 10.1243/09544062JMES776.

[4] Nicola Armaroli and Vincenzo Balzani. The hydrogen issue. *ChemSusChem*, 4(1):21–36, 2011. ISSN 1864564X. doi: 10.1002/cssc.201000182.

[5] Swapan Basu and Ajay Kumar Debnath. General Instruments. *Power Plant Instrumentation and Control Handbook*, pages 229–296, 2015. doi: 10.1016/B978-0-12-800940-6.00004-6. URL https://linkinghub.elsevier.com/retrieve/pii/B9780128009406000046.

[6] Dmitri Bessarabov and Pierre Millet. Fundamentals of Water Electrolysis. In *PEM Water Electrolysis*, pages 43–73. Elsevier, 2018. ISBN 9783527676507. doi: 10.1016/B978-0-12-811145-1.00003-4. URL https://linkinghub.elsevier.com/retrieve/pii/B9780128111451000034.

[7] B. E. Bongenaar-Schlenter, L. J J Janssen, S. J D Van Stralen, and E. Barendrecht. The effect of the gas void distribution on the ohmic resistance during water electrolytes. *Journal of Applied Electrochemistry*, 15 (4):537–548, 1985. ISSN 0021891X. doi: 10.1007/BF01059295.

[8] Marcella Cappadonia, Jiri Divisek, Thomas von der Heyden, and Ulrich Stimming. Oxygen evolution at nickel anodes in concentrated alkaline solution. *Electrochimica Acta*, 39(11-12):1559–1564, 8 1994. ISSN 0013-4686. doi: 10.1016/0013-4686(94)85135-2. URL https://www.sciencedirect.com/science/article/pii/0013468694851352.

[9] Caty Fairclough. Efficiently Mesh Your Model Geometry with Meshing Sequences | COMSOL Blog, 2016. URL https://www.comsol.com/blogs/efficiently-mesh-your-model-geometry-with-meshing-sequences/.

[10] Pai Yu Chang, Ming Nan Fu, and Chung Ho Chen. Simulation for velocity measurement with thermal micro-flow sensors. *Japanese Journal of Applied Physics, Part 1: Regular Papers and Short Notes and Review Papers*, 42(9 A):5859–5864, 2003. ISSN 00214922. doi: 10.1143/JJAP.42.5859.

[11] Hubert Chanson and Hubert Chanson. Unsteady open channel flows: 1. Basic equations. *Environmental Hydraulics of Open Channel Flows*, pages 185–222, 1 2004. doi: 10.1016/B978-075066165-2.50044-8. URL https://www.sciencedirect.com/science/article/pii/B9780750661652500448.

[12] Greig Chisholm and Leroy Cronin. Hydrogen From Water Electrolysis. *Storing Energy*, pages 315–343, 1 2016. doi: 10.1016/B978-0-12-803440-8.00016-6. URL https://www.sciencedirect.com/science/article/pii/B9780128034408000166?via%3Dihub.

[13] Martín David, Carlos Ocampo-Martínez, and Ricardo Sánchez-Peña. Advances in alkaline water electrolyzers: A review. *Journal of Energy Storage*, 23:392–403, 6 2019. ISSN 2352-152X. doi: 10.1016/J.EST.2019.03.001. URL https://www.sciencedirect.com/science/article/pii/S2352152X18306558.

[14] Seth Dunn. Hydrogen futures: toward a sustainable energy system. *International Journal of Hydrogen Energy*, 27(3):235–264, 3 2002. ISSN 0360-3199. doi: 10.1016/S0360-3199(01)00131-8. URL https://www.sciencedirect.com/science/article/pii/S0360319901001318.

[15] M. Elwenspoek. Thermal flow micro sensors. pages 423–435, 2003. doi: 10.1109/smicnd.1999.810580.

[16] Fred Fairbrother and Alfred E. Stubbs. 119. Studies in electro-endosmosis. Part VI. The "bubble-tube" method of measurement. *J. Chem. Soc.*, pages 527–529, 1935. ISSN 0368-1769. doi: 10.1039/JR9350000527. URL http://xlink.rsc.org/?DOI=JR9350000527.

[17] Ruiming Fang and Yin Liang. Control strategy of electrolyzer in a wind-hydrogen system considering the constraints of switching times. *International Journal of Hydrogen Energy*, 3 2019. ISSN 0360-3199. doi: 10.1016/J.IJHYDENE.2019.03.033. URL https://www.sciencedirect.com/science/article/pii/S0360319919309577.

[18] Mitch Geraedts. Assessing the physical phenomena within stacked miniature alkaline electrolysis cells with regards to convective flow and bypass currents by using computational modelling. *ZEF*, 2019.

[19] Alain Goeppert, George A. Olah, and G.K. Surya Prakash. Toward a Sustainable Carbon Cycle: The Methanol Economy. *Green Chemistry*, pages 919–962, 1 2018. doi: 10.1016/B978-0-12-809270-5.00031-5. URL https://www.sciencedirect.com/science/article/pii/B9780128092705000315.

[20] Latif M. Jiji. *Heat Convection*. Springer Berlin Heidelberg, Berlin, Heidelberg, 2009. ISBN 978-3-642-02970-7. doi: 10.1007/978-3-642-02971-4. URL http://link.springer.com/10.1007/978-3-642-02971-4.

[21] Sadhana Kumari, Nilay Kumar, and Raghvendra Gupta. Flow and heat transfer in slug flow in microchannels: Effect of bubble volume. *International Journal of Heat and Mass Transfer*, 129:812–826, 2 2019. ISSN 0017-9310. doi: 10.1016/J.IJHEATMASSTRANSFER.2018.10.010. URL https://www.sciencedirect.com/science/article/pii/S001793101832366#b0005.

[22] S. Laborie, C. Cabassud, L. Durand-Bourlier, and J.M. Lainé. Characterisation of gas–liquid two-phase flow inside capillaries. *Chemical Engineering Science*, 54(23):5723–5735, 12 1999. ISSN 0009-2509. doi: 10.1016/S0009-2509(99)00146-3. URL https://www.sciencedirect.com/science/article/pii/S0009250999001463.

[23] Chi Yuan Lee, Shih Chun Li, Chia Hung Chen, Yen Ting Huang, and Yu Syuan Wang. Real-time microscopic monitoring of flow, voltage and current in the proton exchange membrane water electrolyzer. *Sensors (Switzerland)*, 18(3), 2018. ISSN 14248220. doi: 10.3390/s18030867.

[24] P. Millet. Membrane electrolysers for hydrogen (H2) production. *Advanced Membrane Science and Technology for Sustainable Energy and Environmental Applications*, pages 568–609, 1 2011. doi: 10.1533/9780857093790.4.568. URL https://www.sciencedirect.com/science/article/pii/B9781845699697500187.

[25] Pierre Millet and Sergey Grigoriev. Water Electrolysis Technologies. *Renewable Hydrogen Technologies: Production, Purification, Storage, Applications and Safety*, pages 19–41, 2013. doi: 10.1016/B978-0-444-56352-1.00002-7.

[26] Amin Mohammadi and Mehdi Mehrpooya. A comprehensive review on coupling different types of electrolyzer to renewable energy sources. *Energy*, 158:632–655, 9 2018. ISSN 0360-5442. doi: 10.1016/J.ENERGY.2018.06.073. URL https://www.sciencedirect.com/science/article/pii/S0360544218311381#bib1.

[27] Saeid Mokhatab, William A. Poe, John Y. Mak, Saeid Mokhatab, William A. Poe, and John Y. Mak. Raw Gas Transmission. *Handbook of Natural Gas Transmission and Processing*, pages 103–176, 1 2019. doi: 10.1016/B978-0-12-815817-3.00003-4. URL https://www.sciencedirect.com/science/article/pii/B9780128158173000034.

[28] Niro NAGAI, Masanori TAKEUCHI, and Motohide NAKAO. Effects of Generated Bubbles Between Electrodes on Efficiency of Alkaline Water Electrolysis. *JSME International Journal Series B*, 46(4):549–556, 2003. ISSN 1340-8054. doi: 10.1299/jsmeb.46.549. URL http://joi.jlc.jst.go.jp/JST.JSTAGE/jsmeb/46.549?from=CrossRef.

[29] Thomas F. O'Brien, Tilak V. Bommaraju, and Fumio Hine. *Handbook of Chlor-Alkali Technology*. Springer US, Boston, MA, 2005. ISBN 978-0-306-48623-4. doi: 10.1007/b113786. URL http://link.springer.com/10.1007/b113786.

[30] Sung Hoon Park, Changhwan Park, JinYong Lee, and Byungchul Lee. A Simple Parameterization for the Rising Velocity of Bubbles in a Liquid Pool. *Nuclear Engineering and Technology*, 49(4):692–699, 6 2017. ISSN 1738-5733. doi: 10.1016/J.NET.2016.12.006. URL https://www.sciencedirect.com/science/article/pii/S1738573316303667.

[31] Francisco Pedocchi, J. Ezequiel Martin, and Marcelo H. García. Inexpensive fluorescent particles for large-scale experiments using particle image velocimetry. *Experiments in Fluids*, 45(1):183, 2008. ISSN 07234864. doi: 10.1007/s00348-008-0516-2.

[32] A.H. Abdol Rahim, Alhassan Salami Tijani, Muhammad Fadhlullah, S. Hanapi, and K.I. Sainan. Optimization of Direct Coupling Solar PV Panel and Advanced Alkaline Electrolyzer System. *Energy Procedia*, 79:204–211, 11 2015. ISSN 1876-6102. doi: 10.1016/J.EGYPRO.2015.11.464. URL https://www.sciencedirect.com/science/article/pii/S1876610215021967.

[33] Bastian E. Rapp and Bastian E. Rapp. Fluids. *Microfluidics: Modelling, Mechanics and Mathematics*, pages 243–263, 1 2017. doi: 10.1016/B978-1-4557-3141-1.50009-5. URL https://www.sciencedirect.com/science/article/pii/B9781455731411500095#tf0055.

[34] Ronald J. Adrian. Particle-Imaging Techniques for Experimental Fluid Mechanics. *Annual Review of Fluid Mechanics*, 23:261–304, 1991.

[35] D.M.F. Santos, C.A.C. Sequeira, and R.F.M. Lobo. Effect of alloys modified by sodium borohydride alkaline solutions on the kinetics of hydrogen evolution reaction at Mm(Ni3.6Co0.7Mn0.4Al0.3)1.15 hydride electrodes. *International Journal of Hydrogen Energy*, 35(18):9901–9909, 9 2010. ISSN 0360-3199. doi: 10.1016/J.IJHYDENE.2009.11.015. URL https://www.sciencedirect.com/science/article/pii/S0360319909017583.

[36] Øystein Ulleberg. Modeling of advanced alkaline electrolyzers: a system simulation approach. *International Journal of Hydrogen Energy*, 28(1):21–33, 1 2003. ISSN 0360-3199. doi: 10.1016/S0360-3199(02)00033-2. URL https://www.sciencedirect.com/science/article/pii/S0360319902000332.

[37] H. Vogt and R. J. Balzer. The bubble coverage of gas-evolving electrodes in stagnant electrolytes. *Electrochimica Acta*, 50(10):2073–2079, 2005. ISSN 00134686. doi: 10.1016/j.electacta.2004.09.025.

[38] Gernot Voitic, Birgit Pichler, Angelo Basile, Adolfo Iulianelli, Karin Malli, and Sebastian Bock. Hydrogen Production. *Fuel Cells and Hydrogen*, pages 215–241, 1 2018. doi: 10.1016/B978-0-12-811459-9.00010-4. URL https://www.sciencedirect.com/science/article/pii/B9780128114599000104.

[39] George Wypych. PVC PROPERTIES. *PVC Formulary*, pages 5–44, 1 2015. doi: 10.1016/B978-1-895198-84-3.50004-1. URL https://www.sciencedirect.com/science/article/pii/B9781895198843500041.

[40] Kai Zeng and Dongke Zhang. Recent progress in alkaline water electrolysis for hydrogen production and applications. *Progress in Energy and Combustion Science*, 36(3):307–326, 2010. ISSN 03601285. doi: 10.1016/j.pecs.2009.11.002. URL http://dx.doi.org/10.1016/j.pecs.2009.11.002.

[41] Dongke Zhang and Kai Zeng. Evaluating the behavior of electrolytic gas bubbles and their effect on the cell voltage in alkaline water electrolysis. *Industrial and Engineering Chemistry Research*, 51(42):13825–13832, 2012. ISSN 08885885. doi: 10.1021/ie301029e.

[42] Ankica Đukić and Mihajlo Firak. Hydrogen production using alkaline electrolyzer and photovoltaic (PV) module. *International Journal of Hydrogen Energy*, 36(13):7799–7806, 7 2011. ISSN 0360-3199. doi: 10.1016/J.IJHYDENE.2011.01.180. URL https://www.sciencedirect.com/science/article/pii/S0360319911003132.